UNIVERSIDADE FEDERAL DE MINAS GERAIS
Instituto de Ciências Exatas
Programa de Pós-Graduação em Física

Guilherme Rodrigues Fontenele

STRUCTURAL AND ELECTRONIC PROPERTIES OF TWO-DIMENSIONAL MULTIPHASE INDIUM SELENIDE CRYSTALS

Belo Horizonte
2023

Guilherme Rodrigues Fontenele

STRUCTURAL AND ELECTRONIC PROPERTIES OF TWO-DIMENSIONAL MULTIPHASE INDIUM SELENIDE CRYSTALS

Dissertação apresentada ao Programa de Pós-Graduação em Física da Universidade Federal de Minas Gerais como requisito parcial para obtenção do título de Mestre em Física.

Orientador: Prof. Dr. Rogério Magalhães Paniago

Co-orientador: Prof. Dr. Ângelo Malachias de Souza

Belo Horizonte
2023

Dados Internacionais de Catalogação na Publicação (CIP)

F683s Fontenele, Guilherme Rodrigues.
Structural and electronic properties of two-dimensional multiphase indium selenide crystals / Guilherme Rodrigues Fontenele. – 2023.
99 f. : il.

Orientador: Rogerio Magalhães Paniago.
Coorientador: Ângelo Malachias de Souza.
Dissertação (mestrado) – Universidade Federal de Minas Gerais, Departamento de Física.
Bibliografia: f. 89-99.

1. Microscopia de tunelamento de varredura. 2. Semicondutores. 3. Difração. I. Título. II. Paniago, Rogerio Magalhães. III. Souza, Ângelo Malachias de. IV. Universidade Federal de Minas Gerais, Departamento de Física.

CDU – 539.211 (043)

Ficha catalográfica elaborada por Romário Martins Ribeiro – CRB6 3595

Biblioteca Professor Manoel Lopes de Siqueira – Departamento de Física - UFMG

UNIVERSIDADE FEDERAL DE MINAS GERAIS
INSTITUTO DE CIÊNCIAS EXATAS
PROGRAMA DE PÓS-GRADUAÇÃO EM FÍSICA

FOLHA DE APROVAÇÃO

A presente dissertação, intitulada **"STRUCTURAL AND ELECTRONIC PROPERTIES OF TWO-DIMENSIONAL MULTIPHASE INDIUM SELENIDE MATERIALS"**, de autoria de **GUILHERME RODRIGUES FONTENELE**, submetida à Comissão Examinadora, abaixo-assinada, foi aprovada para obtenção do grau de **MESTRE EM FÍSICA** em onze de setembro de 2023.

Belo Horizonte, 11 de setembro de 2023.

Prof. Rogério Magalhães Paniago
Orientador do aluno
Departamento de Física/UFMG

Prof. Ângelo Malachias de Souza
Coorientador do aluno
Departamento de Física/UFMG

Prof. Edmar Avellar Soares
Departamento de Física/UFMG

Prof. Roberto Hiroki Miwa
Instituto de Física/UFU

Documento assinado eletronicamente por **Angelo Malachias de Souza**, **Membro de comissão**, em 12/09/2023, às 10:25, conforme horário oficial de Brasília, com fundamento no art. 5º do Decreto nº 10.543, de 13 de novembro de 2020.

Documento assinado eletronicamente por **Edmar Avellar Soares**, **Professor do Magistério Superior**, em 12/09/2023, às 12:42, conforme horário oficial de Brasília, com fundamento no art. 5º do Decreto nº 10.543, de 13 de novembro de 2020.

Documento assinado eletronicamente por **Roberto Hiroki Miwa**, **Usuário Externo**, em 12/09/2023, às 19:45, conforme horário oficial de Brasília, com fundamento no art. 5º do Decreto nº 10.543, de 13 de novembro de 2020.

Documento assinado eletronicamente por **Rogerio Magalhaes Paniago**, **Professor do Magistério Superior**, em 13/09/2023, às 10:50, conforme horário oficial de Brasília, com fundamento no art. 5º do Decreto nº 10.543, de 13 de novembro de 2020.

A autenticidade deste documento pode ser conferida no site https://sei.ufmg.br/sei/controlador_externo.php?acao=documento_conferir&id_orgao_acesso_externo=0, informando o código verificador **2614553** e o código CRC **06D4CB7E**.

Referência: Processo nº 23072.255347/2023-44 SEI nº 2614553

ACKNOWLEDGEMENTS

Agradeço as agências de fomento CAPES, CNPq, FAPEMIG e INCT-Nanocarbono por todo o suporte financeiro obtido durante este trabalho.

RESUMO

Neste trabalho, apresentamos o crescimento e as propriedades estruturais e eletrônicas de diferentes fases e polimorfos bidimensionais de seleneto de índio, mais especificamente os compostos InSe e In_2Se_3. As duas amostras sintetizadas para este estudo foram obtidas por meio do método de Bridgman, empregando duas abordagens distintas nas condições termodinâmicas de crescimento. Além de técnicas de caracterização estrutural, empregamos técnicas de microscopia e espectroscopia de tunelamento a fim de obter a correlação entre informações estruturais e eletrônicas, permitindo a investigação da densidade local de estados eletrônicos das diferentes fases e polimorfos deste material.

Começamos a dissertação apresentando uma revisão da literatura a respeito das fases bidimensionais de InSe e In_2Se_3. Os polimorfos da fase In_2Se_3 são caracterizados pelo empilhamento de pentacamadas de índio e selênio, enquanto as estruturas de InSe se caracterizam por tetracamadas empilhadas de índio e selênio. Estes materiais apresentam uma grande variedade estrutural e eletrônica e, por isso, são importantes candidatos para diversas aplicações como células solares, transistores, memórias ferroelétricas, sensores de gás, etc. Finalmente, apresentamos as técnicas experimentais mais importantes utilizadas neste trabalho. Discutimos o método de crescimento de cristais Bridgman e técnicas analíticas de microscopia eletrônica de varredura, espectroscopia de raios-X por energia dispersiva, difração de raios-X, difração de elétrons retroespalhados e microscopia/espectroscopia de tunelamento.

Obtivemos com sucesso dois cristais de seleneto de índio, com cada uma das amostras tendo uma proporção de fases e polimorfismos diferentes. A partir de medidas de difração de raios-X e de elétron retroespalhados, conseguimos quantificar a proporção de fases tanto no volume quanto em regiões superficiais na escala de mícrons de ambos os cristais. Através de medidas de microscopia e espectroscopia de tunelamento, conseguimos obter imagens de alta resolução das estruturas lamelares na escala nanométrica, assim como determinar a densidades de estados eletrônicos dos polimorfos de In_2Se_3 e InSe.

Palavras-chave: Microscopia de Tunelamento por Varredura, Espectroscopia de Tunelamento por Varredura, Seleneto de Índio, Semicondutores, Difração de elétrons retroespalhados.

ABSTRACT

In this work, we present the growth and the structural and electronic properties of two-dimensional phases and polymorphs of indium selenide, specifically the InSe and In_2Se_3 compounds. The two samples synthesized for this study were obtained by the Bridgman method, employing two distinct approaches in the thermodynamic conditions of growth. In addition to structural characterization techniques, we employed tunneling microscopy and spectroscopy techniques to obtain the correlation between structural and electronic information. This allowed the investigation of the local electronic density of states of the different phases and polymorphs of this material.

We begin the dissertation by presenting a literature review on the two-dimensional phases of InSe and In_2Se_3. The polymorphs of the In_2Se_3 phase are characterized by the stacking of quintuple layers of indium and selenium, while the structure of InSe is characterized by stacked tetralayers. These materials present a wide variety of structural and electronic properties and are important candidates for various applications, such as solar cells, transistors, ferroelectric memories, gas sensors, etc. Finally, we present the most important experimental techniques used in this work. We discuss the Bridgman crystal growth method and analytical techniques of scanning electron microscopy, energy dispersive X-ray spectroscopy, X-ray diffraction, electron backscattered diffraction, and tunneling microscopy/spectroscopy.

We successfully obtained two indium selenide crystals, with each of the samples having a different proportion of phases and polymorphs. From X-ray diffraction and electron backscattered diffraction measurements, we were able to quantify the proportion of phases in both the volume and surface regions of the crystals. Through microscopy measurements and tunneling spectroscopy, we were able to obtain high-resolution images of the lamellar structures at the nanometer scale, as well as determine the electronic densities of states of InSe and In_2Se_3, for each phase and polymorph.

Keywords: Scanning Tunneling Microscopy, Scanning Tunneling Spectroscopy, Indium Selenide, Semiconductors, Electron backscattered diffraction.

TABLE OF CONTENTS

1. Introduction 11

2. Literature Review of Indium Selenide 13

2.1 Physical Properties and Applications of In_2Se_3 14

2.1.1 α-In_2Se_3 14

2.1.2 β-In_2Se_3 17

2.1.3 δ-In_2Se_3 20

2.2 Physical Properties and Applications of InSe 21

2.2.1 β-InSe 21

2.2.2 γ-InSe 23

3. Experimental Techniques 27

3.1 The Bridgman Method for Crystal Growth 27

3.2 Scanning Electron Microscopy 29

3.2.1 Scanning Electron Microscope 30

3.2.2 Energy-dispersive X-ray Spectroscopy 33

3.2.3 Electron Backscatter Diffraction 34

3.3 X-ray Diffraction 37

3.3.1 X-ray Scattering by a Crystal 37

3.4 Scanning Tunneling Microscopy and Spectroscopy 39

3.4.1 The Tunneling Phenomenon 40

3.4.2 Scanning Electron Microscope 44

3.4.3 The Bardeen theory of Tunneling 47

3.4.4 Scanning Tunneling Spectroscopy 51

4. Results and discussion 59

4.1 Crystal Growth and Structural Characterization 59

4.2 Measurements of Local Electronic Density of States 73

4.2.1 Scanning Tunneling Microscopy 73
4.2.2 Scanning Tunneling Spectroscopy 76
5. Conclusions and Perspectives 88
REFERENCES 89

1. INTRODUCTION

The investigation of two-dimensional (2D) and layered van der Waals (vdW) materials continues to attract substantial interest ever since the isolation of graphene [1] and the subsequent study of its unique electronic [2-4], thermal [5, 6], and optical properties [7]. Graphene consists of one-atom-thick sheets of carbon atoms with sp2 hybridization arranged in a honeycomb structure. Its valence and conduction bands exhibit an approximately linear dispersion near the Fermi level, and the electronic band structure is a Dirac cone [8]. While possessing groundbreaking potential to revolutionize science and technology, the absence of a band gap and limited light absorption restricts its applicability in electronic devices such as photovoltaic cells, light-emitting diodes (LEDs), and field-effect-based devices. Consequently, it becomes crucial to explore alternative 2D and layered materials.

Apart from graphene, the scientific community has explored a wide variety of 2D and layered materials such as silicene [9], germanene [10], phosphorene [11], h-BN [12], and transition metal dichalcogenides (TMD's) [13]. These materials exhibit diverse electronic properties, and can be classified as metals, semimetals, topological insulators, semiconductors, and insulators. Another significant group of layered materials is the III-VI semiconductors, which consist of alloys composed of elements from Group III and Group VI of the periodic table. Typically, these materials exhibit layer-dependent band gaps, efficient light absorption, and high carrier mobility [14]. Moreover, some of these materials possess topological properties [15] and can also exhibit in-plane and out-of-plane ferroelectricity [16].

In this work, we investigated the structural and electronic properties of indium selenide, a group of materials with a variety of phases and polymorphisms. Indium selenide belongs to the III-VI group of semiconductors and consists of compounds of indium (In) and selenium (Se) atoms. These materials crystallize in different stoichiometry and polymorphisms, such as InSe, In_2Se_3, and In_4Se_3 [17], and it includes three-dimensional (3D) and layered phases with diverse atomic and electronic structures. InSe has at least three layered polymorphisms labeled as β, ε, and γ-InSe [18]. Furthermore, In_2Se_3 has at least four different polymorphisms, one 3D called γ-In_2Se_3, and three layered polymorphisms known as α, β, and δ-In_2Se_3 [19-21]. Additionally, there are other variations in polymorphisms, such as α' and β'-In_2Se_3. Our primary focus in this work is solely on the layered polymorphs of InSe and In_2Se_3.

The α, β, and δ-In_2Se_3 variants are characterized by their quintuple layer (QL) structures, which consist of monoatomic Se-In-Se-In-Se layers. Within each layer, the atoms are held together by covalent bonds, while neighboring QLs are connected by van der Waals forces [22]. The α-In_2Se_3 phase exhibits two distinct stacking variants, known as α(2H) and α(3R), represented by the space groups $P6_3mc$ and R3m, respectively. On the other hand, β-In_2Se_3 displays three different stacking variants: 1T, 2H, and 3R. The corresponding space groups are P-3m1 for β(1T), $P6_3mc$ for β(2H), and R-3m for β(3R) [23]. To date, evidence strongly supports that the δ-In_2Se_3 is the stacking variant of β-In_2Se_3, β(1T). Furthermore, all three polymorphs of InSe (β, ε, and γ) are arranged in tetralayers composed of monoatomic Se-In-In-Se layers. The β-InSe structure belongs to the space group $P6_3/mmc$, the γ-InSe structure adopts the R3m space group, and the ε-InSe structure possesses the P-6m2 space group [24].

Although complex, sometimes with minor differences in atomic stacking and local symmetry, these different phases exhibit exciting new bulk and surface electronic properties. The current interest in these materials resides in their potential applications in electronics, optoelectronics, and solar cells. However, the controlled synthesis of indium selenide with desired stoichiometry and phase is challenging due to the complexity of the indium–selenium phase diagram.

We present a comprehensive analysis of the crystal growth, atomic structure and electronic properties of β, ε, and γ-InSe, as well as α(3R), β(2H), and δ-In_2Se_3. The bulk crystals were grown using the Bridgman method, resulting in highly multiphase indium selenide crystals. For the structural analysis, a combination of scanning electron microscopy (SEM), energy-dispersive X-ray spectroscopy (EDS), electron backscatter diffraction (EBSD), and powder X-ray diffraction (XRD) measurements were performed. The investigation of the electronic properties involved scanning tunneling microscopy and spectroscopy (STM/STS), which allows one to image the surface of the sample while determining the electronic local density of states via a tunneling spectrum. Also, electronic density of states calculations was performed using Density Functional theory (DFT). Combining the experimental data and computational modelling provides an in-depth insight into the interplay between the structural and the electronic properties of the synthesized phases.

2. LITERATURE REVIEW OF INDIUM SELENIDE

Indium selenide compounds have been well-known for their incredible and diverse atomic and electronic structure, with novel and highly desired properties for next-generation devices, including high-order topological properties [15], both in-plane and out-of-plane ferroelectricity [25-28], piezoelectricity [29-31], etc. This family of compounds exhibits extensive phases, polymorphisms, and polytypes, which means that it crystallizes in a variety of forms, each possessing unique atomic and electronic properties.

Figure 2.1 illustrates the binary phase diagram of indium-selenium. It shows incredible and complex stoichiometries such as InSe, In_2Se_3, In_6Se_7, and In_4Se_3 [17]. In_2Se_3 appears to be the most complex compound among the indium selenide family, and it includes high-temperature and low-temperature phases such as δ-In_2Se_3 and α'-In_2Se_3, respectively.

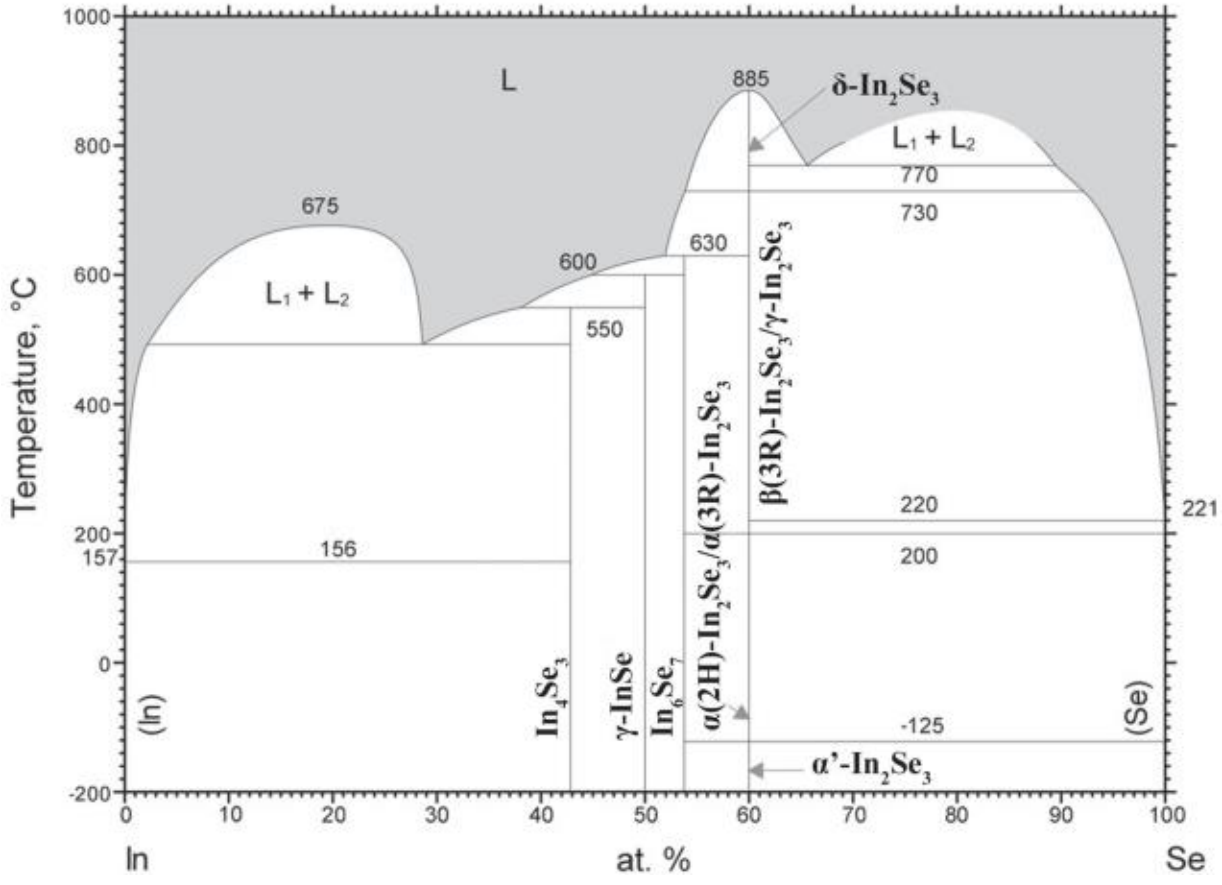

Figure 2.1. Indium-selenium (In-Se) binary phase diagram. Figure taken from reference [17].

Despite the complexity of the phase diagram, it is important to note that the literature already contains reports on additional phases of InSe and In_2Se_3. This indicates that the In-Se phase diagram shown is even more complex than it is depicted. For instance, β and ε-InSe [32-34] are not presented in the diagram, indicating that even InSe, which seems less complex based on its phase diagram, still exhibits different polymorphisms and structure variations.

In this chapter, our goal is to provide a comprehensive literature review on indium selenide, with a particular focus on the properties and characteristics of the layered phases of InSe and In_2Se_3. The investigation will be centred on their crystal structures, electronic properties, and potential applications.

2.1 Physical Properties and Applications of In_2Se_3

2.1.1 α-In_2Se_3

The α phase of In_2Se_3 exhibits a layered van der Waals structure, consisting of closely bonded monoatomic layers of indium (In) and selenium (Se) arranged in a quintuple layer (QL), with a stacking sequence of Se-In-Se-In-Se [35, 36]. The cohesion between the monoatomic layers arises from covalent bonding, while the interaction between neighbouring QLs is governed by the van der Waals force. As a result of this van der Waals structure, it is possible to obtain few QLs from a bulk α-In_2Se_3 through mechanical exfoliation techniques [37].

Liu et al. and Küpers et al. conducted a comprehensive investigation and characterization of the α phase of In_2Se_3, using techniques such as transmission electron microscopy, X-ray diffraction, and Raman spectroscopy [23, 38]. Remarkably, they were able to characterize the two known stacking variants of α-In_2Se_3: α(2H) and α(3R). These two studies stand out as the only ones, up to this moment, to differentiate between these two α polytypes.

α(2H) and α(3R) represent distinct polytypes of α-In_2Se_3, which represents a variant of the quintuple layer but with distinct stacking arrangements and, consequently, a different crystal structure. These variations in stacking arrangements can lead to differences in physical

properties and behavior, making them an important consideration when studying and characterizing crystalline materials.

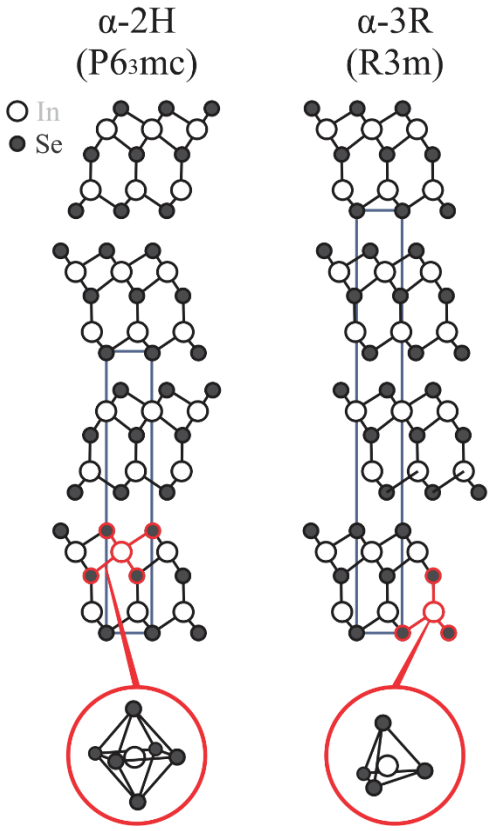

Figure 2.1.1. Schematic representation of α(2H) and α(3R) variants of In_2Se_3 along the *c*-direction. In the α(2H) variant, the QLs are reflected in the *ab* plane. The α(3R) exhibits a translation of the QLs along the *ab* plane. Figure adapted from reference [23].

In the case of α(2H), the quintuple layers undergo a reflection in every alternate QL, with the stacking in the *c*-direction, creating a distinctive zigzag arrangement. Furthermore, in the α(3R) variant, a translation in the *ab* plane occurs, leading to a lateral shift pattern. Figure 2.1.1 illustrates the representation of both stacking variants of the α polymorph, showcasing the distinct arrangements of quintuple layers within the crystal lattice. Moreover, the α(2H) polytype exhibits a hexagonal crystal structure with the space group $P6_3mc$, whereas the α(3R) variant possesses a rhombohedral space group R3m.

Manolikas reported a phase transformation of α-In_2Se_3 that manifests at temperatures below -120°C. This polymorph is known as the α'-In_2Se_3 phase, and it is characterized by a disordered arrangement of quintuple layers along the *c*-axis [21].

Our primary focus will be on the α(3R) variant, which shall be denoted only as α-In_2Se_3. This is motivated by the fact that the α(3R) polytype seems to be more frequently obtained via crystal growth methods and that the scientific literature usually studies this rhombohedral α-In_2Se_3. Also, we successfully synthesized this polymorph in this work.

The study of the electronic properties of α-In_2Se_3 is quite cumbersome in the literature. Early calculations of the band structure hinted at the possibility of this material being a metal [39]. However, experimental evidence confirming α-In_2Se_3 as a semiconductor motivated physicists to reevaluate the electronic structure calculations. Li et al. pointed out that the investigation of the fundamental band gap nature is often neglected. However, through first-principles calculations, they successfully determined an indirect fundamental band gap of 1.27 eV for the α-In_2Se_3 [22]. Narita et al. performed calculations on the electronic band structure of α-In_2Se_3, revealing a fundamental band gap of 1.45 eV [40]. Moreover, Ho et al. identified the fundamental band gap of bulk and multilayer α-In_2Se_3 as direct [41], supported by experimental data from Gedrim et al. [42]. This indicates that the indirect band gap may occur in a few-layers limit.

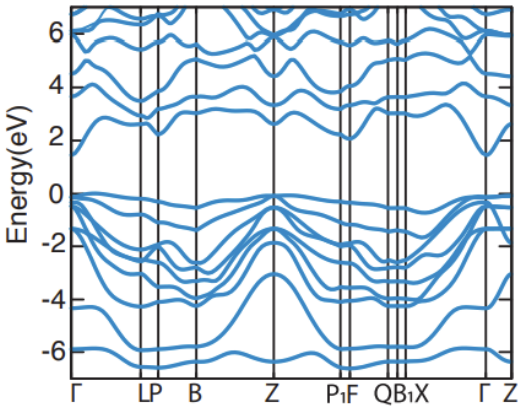

Figure 2.1.2. Electronic band structure of α-In_2Se_3. The top of the valence band is in between the Γ and L points, while the bottom of the conduction band is at the Γ point. The band gap is approximately 1.27 eV. Figure taken from reference [22].

Lyu et al. first reported the thickness-dependence of the band gap for a few layers of α-In_2Se_3. Their findings revealed that the band gap increases as the film thickness decreases, ranging from 1.44 eV in a 48 nm thickness to 1.64 eV in an 8 nm thickness [43]. The ability to tune the band gap by varying the film thickness presents exciting opportunities for diverse

applications such as solar cells [44], photodetectors [45], and other semiconductor-based devices.

Zhou et al. reported the first experimental evidence of out-of-plane ferroelectricity and piezoelectricity in α-In_2Se_3 nanoflakes [25] using the piezo-response force microscopy technique. This opened the door for the study of the α-In_2Se_3 applied to ferroelectric devices. For instance, Wan et al constructed a prototype of rewritable nonvolatile memory using ultrathin α-In_2Se_3 samples [26], while Wang et al. fabricated ferroelectric semiconductor field-effect transistors (FeSFETs) [27].

2.1.2 β-In_2Se_3

The β-phase is an additional layered polymorph of In_2Se_3, sharing the same stacking sequence of monoatomic layers, namely Se-In-Se-In-Se, thus forming quintuple layers as well. Similarly, to α-In_2Se_3, the cohesion of the individual monoatomic layers is primarily attributed to covalent bonding, while the van der Waals forces assume a pivotal role in holding the QLs together.

Liu et al. investigated the three known stacking variants of β-In_2Se_3, which are classified as follows: β(1T) with a trigonal structure, β(2H) with a hexagonal structure, and β(3R) with a rhombohedral one. To date, their study stands as the only report of the β(1T) polytype [38]. The observation of the β(3R) phase is also corroborated by Osamura et al., who conducted an X-ray diffraction analysis to characterize the crystalline structure as rhombohedral, with a space group of R-3m [46]. Van Landuyt et al. [19] and Manolikas [21] corroborated the formation of β(3R) through transmission electron microscopy. In comparison to β(3R), the β(2H) and β(1T) polytypes appear to have received limited attention in the literature, suggesting that the rhombohedral and the trigonal β structures might present challenges in terms of crystal growth.

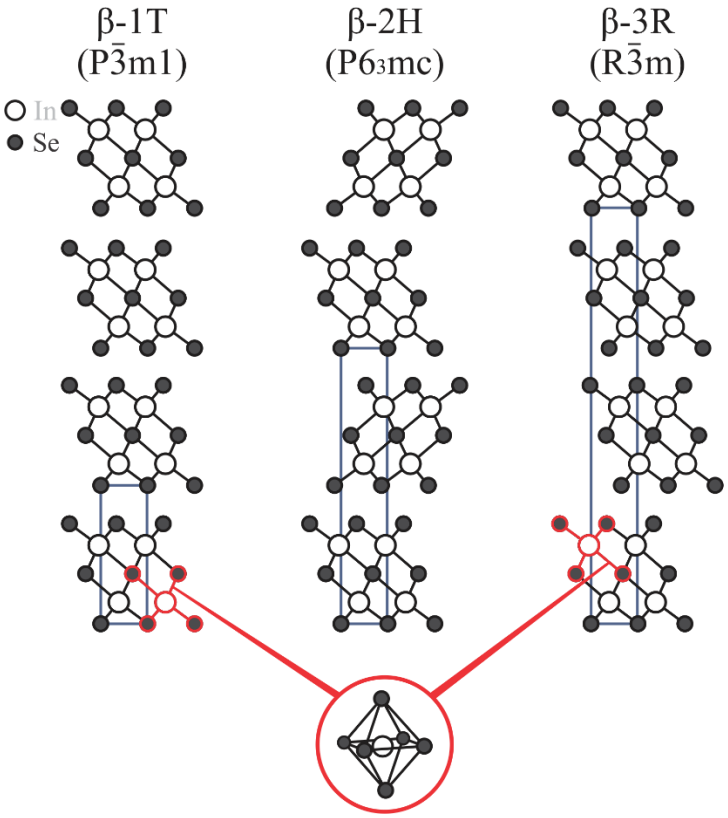

Figure 2.1.3. Schematic representation along the c-axis of β(1T), β(2H), and β(3R) variants of In_2Se_3. Figure adapted from references [23] and [38].

In the β(3R) variant, the QLs undergo a translation along the ab plane, thus creating a lateral shift pattern. Furthermore, the QLs of the β(2H) polytype undergo a reflection in ab plane, while stacking in c-direction. Finally, β(1T) variant involves stacking the QLs along the c-direction without any rotation or translation. Figure 2.1.3 shows a schematic view of the three stacking variants of the β polymorph of In_2Se_3. The space groups of β(3R), β(2H), and β(1T) are R-3m, $P6_3mc$ and P-3m1, respectively [38]. Moreover, there exists a variation of the β-In_2Se_3 known as β′. In a recent investigation conducted by Zhang et al., it was demonstrated that the phase transition from β to β′ takes place at approximately -93°C [47]. This structure is not presented in the binary phase diagram of indium-selenium shown in Figure 2.1.

We focus below on the β(3R) polytype, which is denoted only as β-In_2Se_3. As we mentioned earlier, the rhombohedral β-In_2Se_3 is the most commonly studied in the literature, and indeed, we have successfully grown the β(3R) polytype.

Debbichi et al. performed an Ab Initio calculation on the electronic structure of β-In_2Se_3, revealing that the β phase displays a semiconductor band structure with an indirect band gap of 0.7 eV for the bulk material and 1.29 eV for a monolayer. Additionally, the fundamental band gap remains indirect regardless of the number of layers [48]. Interestingly, these computational results suggest that β-In_2Se_3 also has a tunable band gap property, and as the number of layers increases, the band gap decreases. Liu et al. conducted first-principles calculations on the electronic structure of β-In_2Se_3 and obtained an indirect fundamental band gap of 0.46 eV [22].

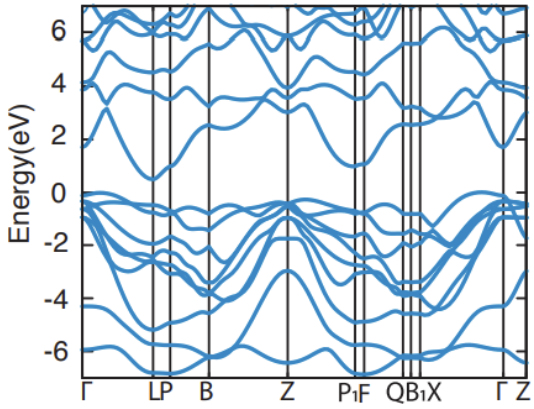

Figure 2.1.4. Electronic band structure of β-In_2Se_3. The band gap is indirect, with a value of 0.46 eV. Figure taken from reference [22].

β-In_2Se_3 has demonstrated its utility in the fabrication of electronic devices, including gas sensors, infrared detectors, and photodetectors. In a study by Bolarinwa et al., they examined the structural and electronic characteristics of β-In_2Se_3 and its interaction with CO, NO_2, and NO molecules [49]. Their findings indicated that the β phase exhibits superior sensitivity to NO molecules compared to the other molecules, showcasing its potential as a highly promising material for gas sensor fabrication. Moreover, Claro et al. successfully demonstrated the creation of photodetectors employing five quintuple layers of β-In_2Se_3 [50]. Their work revealed a remarkable fast response sensitivity to near-infrared light. Additionally, Zheng et al. presented a scalable fabrication method for a photodetector integrated with a β-In_2Se_3/Si heterojunction. This device exhibited a wide photo-response range, spanning from the ultraviolet to the near-infrared region [51].

2.1.3 δ-In_2Se_3

The δ-In_2Se_3 emerges as a variant of the β-In_2Se_3, identified as the β(1T) variant. Lutz et al. first reported that δ-In_2Se_3 was obtained after heating the β(2H)-In_2Se_3 above 807°C [52]. Moreover, as the binary phase diagram in Figure 2.1 indicates, the δ phase is in fact a high-temperature structure, although it demonstrates stability at room temperature.

It is difficult to justify why one calls the β(1T) polytype as δ-In_2Se_3. It is crucial to highlight that the β(1T) polytype, now referred to as δ-In_2Se_3, has been subject to limited attention in the available literature. Up until now, only one paper [38] has been conducted experimental investigating the properties of the β(1T) polytype, i.e., δ-In_2Se_3.

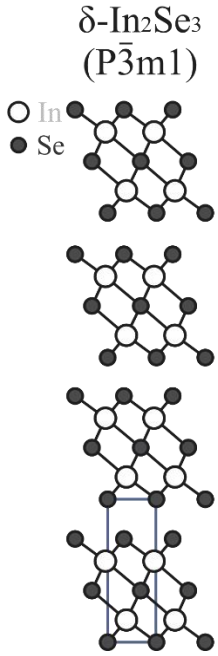

Figure 2.1.5. Schematic representation of the atomic structure of the δ-In_2Se_3 along the *c*-direction. The stacking of quintuple layers in the c-direction occurs without any rotation, translation, or reflection. Figure adapted from reference [38].

The atomic structure of δ-In_2Se_3 is identical to that of the β(1T) polymorph. The stacking of QLs along the *c*-direction occurs without any rotation, translation, or reflection of the adjacent QLs. Figure 2.1.5 shows the atomic structure of β(1T), now named as δ-In_2Se_3. Thus, we will consistently refer to this polymorph as δ-In_2Se_3.

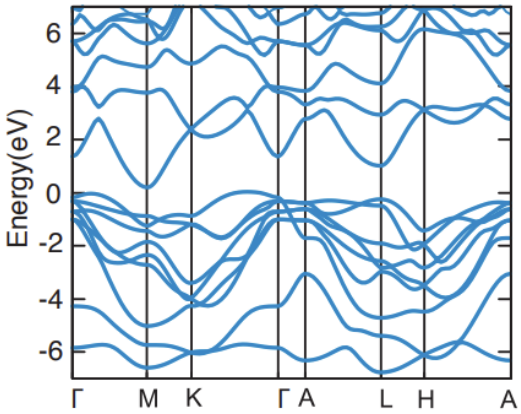

Figure 2.1.6. Electronic band structure of δ-In2Se3. The nature of the band gap is indirect, and the value is 0.32 eV. Figure taken from reference [22].

Li et al. conducted an analysis of the electronic structure of δ-In_2Se_3 using first-principles calculations. They reported a fundamental band gap of 0.32 eV [22]. Notably, their research revealed a significant disparity between the fundamental and optical gaps in the δ polymorph.

2.2 Physical Properties and Applications of InSe

2.2.1 β-InSe

β-InSe is a van der Waals layered phase of indium selenide, composed of tetralayers (TL) arranged in the Se-In-In-Se configuration. Like the previously mentioned layered phases and polymorphisms, the van der Waals force governs the interaction between the tetralayers in β-InSe, while the cohesion between the monoatomic layers arises from covalent bonding. Figure 2.2.1 shows a schematic view of the β-InSe atomic structure.

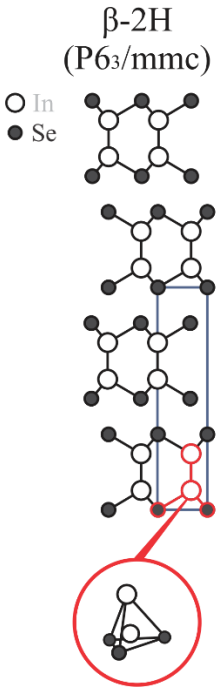

Figure 2.2.1. Schematic representation of the atomic structure of β-InSe along the c-direction. The tetralayers are rotated by 60° in the ab plane.

The β-InSe phase exhibits a hexagonal crystal structure, where every second tetralayer is rotated by 60° in the ab plane. The hexagonal structure of the β polymorph was confirmed through X-ray diffraction analysis conducted by Čelustka et al., who also identified the space group as $P6_3/mmc$ [53]. Grimaldi et al. also investigated the structural properties of β-InSe, further corroborating the hexagonal structure and the arrangement of the TLs [54]. In a more recent study, Küpers et al. presented the atomic arrangement of the β-InSe and provided a comprehensive overview of the stacking pattern of the tetralayers.

The electronic structure of β-InSe was investigated by Kang et al. using angle-resolved photoemission spectroscopy [55]. In their study, they observed and conclusively identified a direct fundamental band gap of 1.3 eV. This finding is corroborated by other computational and experimental studies. For instance, Guo et al. conducted first-principles calculations and reported a minimum band gap of 1.25 eV [56]. Furthermore, Gürbulak also reported a very similar band gap value of 1.28 eV [57].

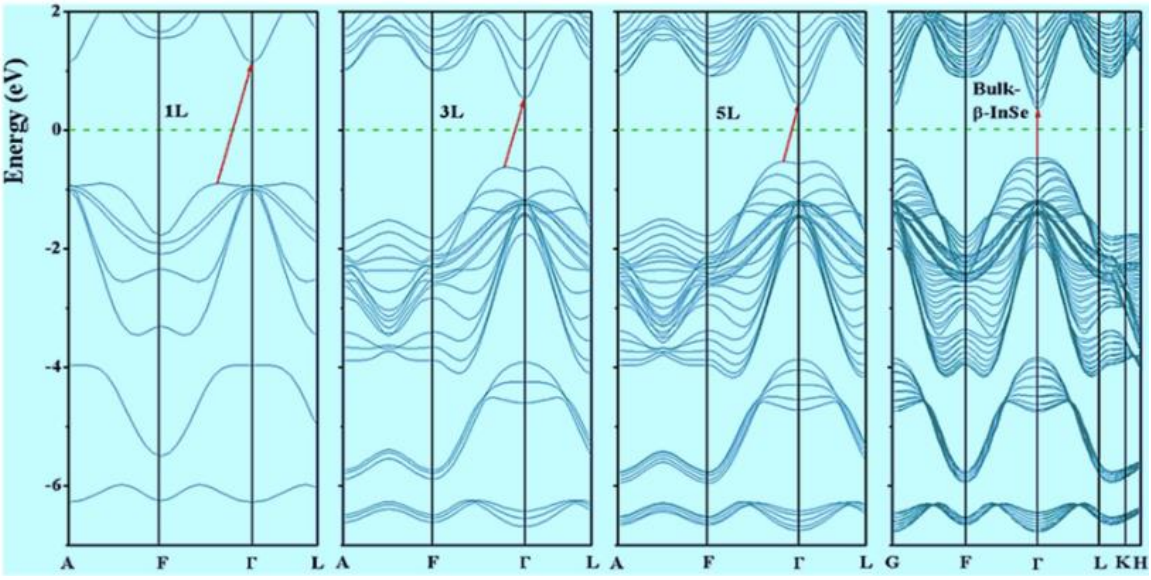

Figure 2.2.2. Electronic band structure calculations of a single layer, three layers, five layers, and bulk β-InSe. Figure taken from reference [58]. In the bulk, the direct band gap occurs in the Γ point and the value is 1.39 eV.

Sang et al. reported a transition from direct to indirect band gap behavior in β-InSe as the material changes from bulk to 5-, 3-, and single-layer configuration. In the few-layer form of β-InSe, it exhibits an indirect band gap, whereas the bulk calculations indicate a direct fundamental band gap of 1.39 eV [58]. This study further indicates that β-InSe exhibits a tunable band gap, as illustrated in Figure 2.3.2.

β-InSe exhibits ferroelectricity and piezoelectricity. Hu et al studied β-InSe nanoflakes using piezo-response force microscopy. They visualized out-of-plane and in-plane ferroelectricity at room temperature [59]. This opens the door for a wide range of applications in novel devices, including nonvolatile ferroelectric memories, ferroelectric photodetectors, etc. Additionally, Li et al. demonstrated the exceptional electronic and optical properties of β-InSe by developing a highly sensitive photodetector based on a β-InSe/graphene heterostructure [60].

2.2.2 γ-InSe

γ-InSe is a rhombohedral polymorph of InSe with space group R3m [61, 62]. It also consists of tetralayers arranged in a Se-In-In-Se configuration. These tetralayers are also bonded by van der Waals force. One significant distinction from β-InSe is that in γ-InSe, the tetralayers undergo a translation in the ab plane during the stacking in the c-direction [23, 63]. Figure 2.2.3

shows a schematic view of the atomic structure of γ-InSe, with every second layer being translated.

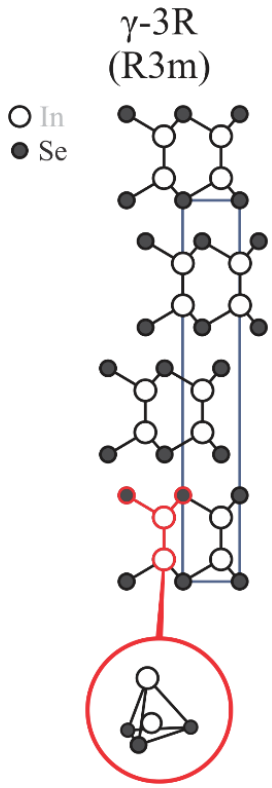

Figure 2.2.3. Schematic representation of the atomic structure of γ-InSe along the *c*-direction.

Julien et al. successfully determined the band gap of γ-InSe to be 1.29 eV. However, the nature of the fundamental band gap, whether it is direct or indirect, was not investigated in their work. On the other hand, Gomes da Costa et al. conducted an electronic structure calculation for γ-InSe and found that the band gap is direct, with a value of 1.35 eV [63]. Other experimental evidence supporting the electronic structure and the nature of the band gap in γ-InSe was provided by Xu et al [64]. They conducted angle-resolved photoemission spectroscopy to study the electronic structure of the material while inducing various temperatures in the crystal. Furthermore, Hamer et al. also conducted angle-resolved photoemission spectroscopy to study γ-InSe, obtaining a band gap of 1.25 eV for the bulk [65]. Their findings revealed a transition from a direct to an indirect band gap for monolayer and bilayer γ-InSe.

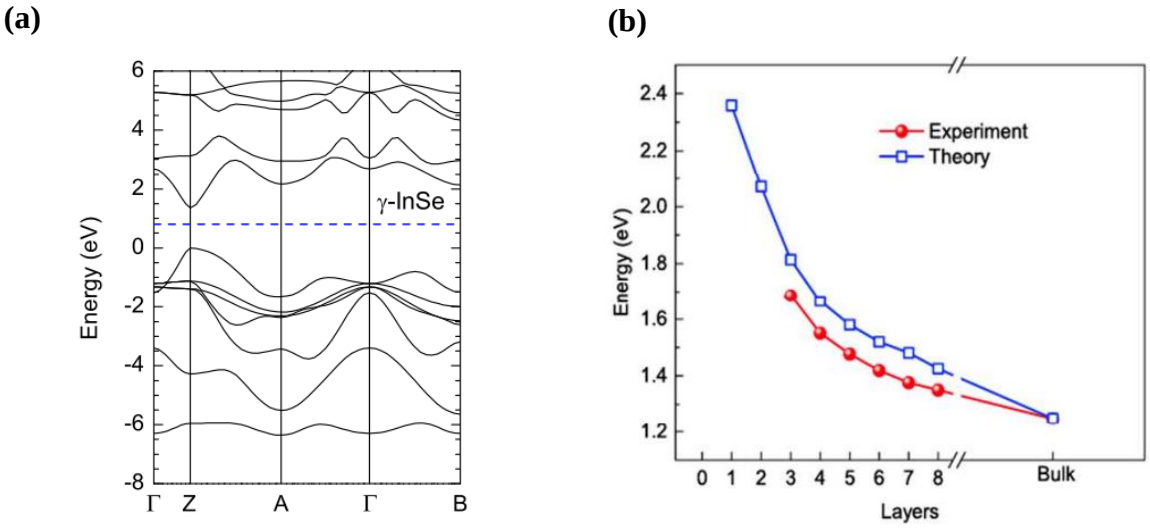

Figure 2.2.4. (a) Electronic band structure of bulk γ-InSe. An indirect fundamental band gap of 1.35 eV was reported. Figure taken from reference [66]. **(b)** Value of the band gap both in experiment and theory reported by Song et al. [67].

Like other indium selenide compounds, γ-InSe has garnered attention as a promising ferroelectric material that holds great potential for constructing novel electronic devices. Sui et al. reported on the properties of both in-plane and out-of-plane ferroelectricity in this material [68]. Dai et al. proposed an ultra-high photon responsivity photodetector based on multilayer γ-InSe [69]. Finally, Yang et al. reported a photodiode based on a γ-InSe/Ge heterojunction [70].

2.2.3 Other InSe polymorphs

In this work, we have also successfully synthesized the ε-InSe, as well as a new polymorph which little is known in literature, with a space group of C2/m.

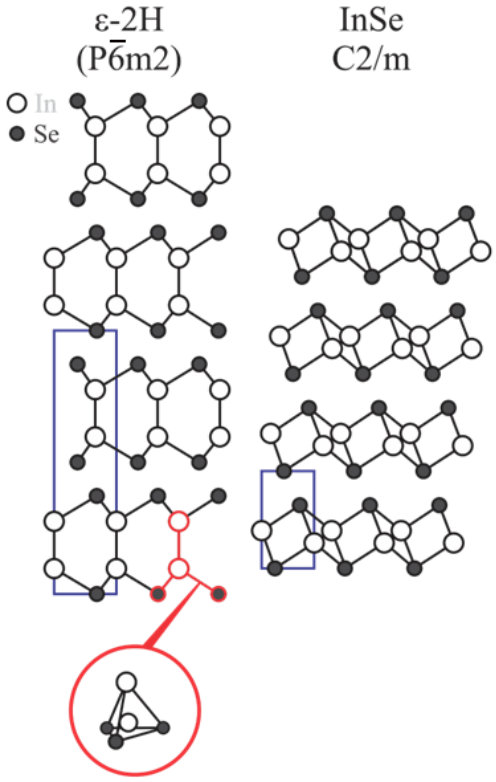
ε-2H
(P6̄m2)
InSe
C2/m
In
Se

3. EXPERIMENTAL TECHNIQUES

In this chapter, we present an overview of the experimental setups and techniques used in this work. These techniques included the Bridgman method for crystal growth, scanning electron microscopy, energy-dispersive X-ray spectroscopy, electron backscatter diffraction, and powder X-ray diffraction, for the structural analysis. Scanning tunneling microscopy and spectroscopy were applied to the study of the interplay between atomic and electronic properties.

The first section is dedicated to presenting the synthesis method. The second section is devoted to the study of the fundamental principles of scanning electron microscopy and its associated techniques, energy-dispersive X-ray spectroscopy and electron backscatter diffraction. The third section is dedicated to the theory of X-ray. Finally, we discuss scanning tunneling microscopy and spectroscopy and their applicability in the study of the local density of states of layered van der Waals materials.

The combined utilization of these experimental techniques provided us with a comprehensive structural and electronic understanding of the surface properties of InSe and In_2Se_3. In the following sections, we present the theoretical principles, experimental setups, and specific applications of each technique.

3.1 The Bridgman Method for Crystal Growth

The Bridgman method is a crystal growth technique that has become an essential tool in materials science and engineering, especially for producing large-scale semiconductors for manufacturing electronic devices. First described in a seminal article by Percy Bridgman in 1925 [71], the Bridgman method involves controlling the temperature and cooling rate to slowly solidify a material from the melt. By controlling the thermodynamic variables, one can produce large, uniform, and high-quality crystals, which are essential for high-performance electronic applications. More recently, topological materials such as Bi_2Se_3 [72, 73] and Sb_4Te_3 [74, 75]

have also been grown using this technique. A drawback is that only materials that melt under approximately 1500^0C can be grown by this technique.

In the original description of Bridgman, a vertical furnace is maintained at a temperature above the melting point of the elemental material (in stoichiometric proportion) of the crystal to be produced. An evacuated quartz tube containing the materials in the molten condition is gradually lowered from the bottom of a hot zone into the air or an oil cooling bath. This results in the solidification process beginning at the tube's base and gradually advancing along its axis as the material descends. A schematic diagram shown in Figure 3.1.1 illustrates the Bridgman setup.

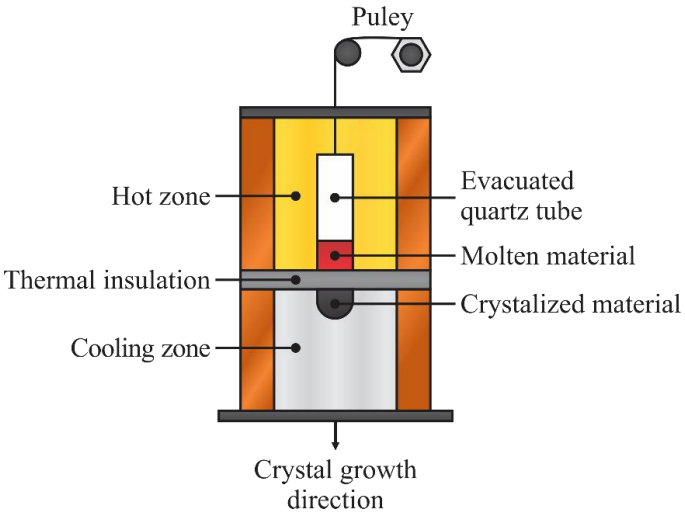

Figure 0.1. The schematic diagram of the original Bridgman method proposed in 1925.

In this work, a simplified version of the Bridgman apparatus was employed. This approach involved evacuating a quartz tube containing the mixed materials and subsequently placing it in a furnace heated to a temperature above the melting point of the materials (220,8 °C for Selenium and 156,6 °C for Indium). After several hours of melting to make the solution homogeneous, the furnace temperature was gradually lowered until the crystal reached room temperature. Figure 3.1.2 presents a schematic diagram illustrating this simplified Bridgman method.

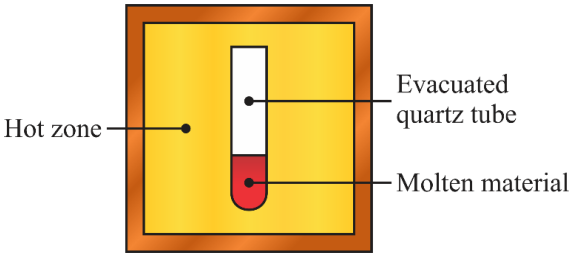

Figure 0.2. The schematic diagram of the simplified Bridgman method used in this work.

All samples were grown using a VRC Millenium furnace, as shown in Figure 3.1.3. The furnace employed in this study offers a maximum temperature of 1100°C, providing a sufficiently high-temperature range for the melting of indium and selenium. Its design and specifications ensure precise temperature control and uniform heating throughout the crystal growth process.

Figure 0.3. VRC Millenium furnace.

3.2 Scanning Electron Microscopy

Scanning Electron Microscopy (SEM) is an important and powerful technique for imaging and analysing the microstructural and morphology of a wide range of materials, such as metals, ceramics, polymers, biological specimens, minerals, and nanomaterials. Moreover, SEM-based techniques such as Energy-Dispersive X-ray Spectroscopy (EDS) and Electron

Backscatter Diffraction (EBSD) can be used to determine the chemical composition and obtain crystallographic information about all the above-mentioned materials.

3.2.1 Scanning Electron Microscope

In a scanning electron microscope, the primary electrons are produced at the top of an optoelectronic high vacuum column, which consists of an electron gum and a combination of lenses. The emission of electrons is made by a thermionic process, done by the heating of a filament (usually tungsten). The electrons are then accelerated along the column, where they pass through a series of electron lenses and are collimated, producing a thin beam with a diameter around fractions of microns. Finally, the thin electron beam hits the surface of the sample, which is scanned by the electron beam using a microscope coil. Figure 3.2.1a shows the components of scanning electron microscopy.

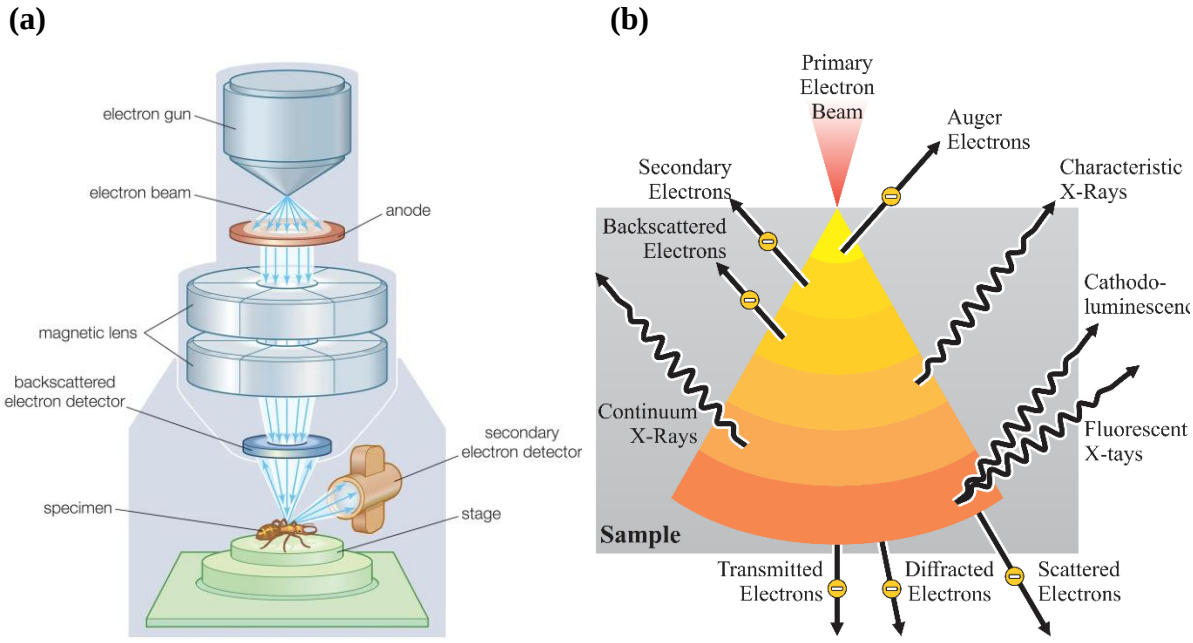

Figure 3.2.1. (a) Scanning electron microscope components. **(b)** Electron-Matter interaction and types of signals generated.

The interaction of the electron beam with the sample results in a variety of particles, such as secondary electrons (SE), backscattered electrons (BSE), continuum X-rays, characteristic X-rays, etc. The electrons and X-rays can be detected by appropriate detectors. A schematic diagram of the electron-matter interaction is shown in Figure 3.2.1b. In this

dissertation, we were mainly interested in the information provided by secondary electrons, backscattered electrons, and characteristic X-rays.

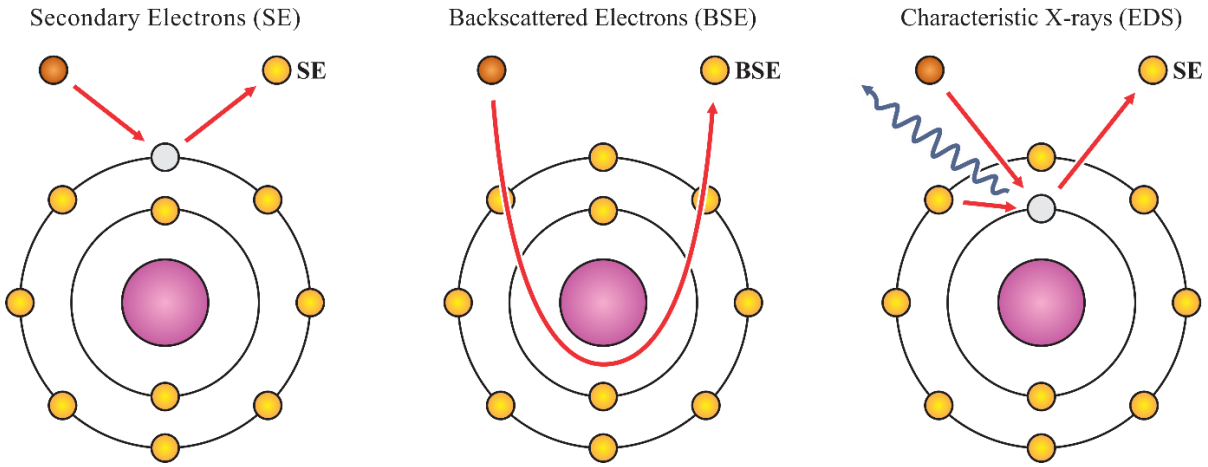

Figure 3.2.2. Physical visualization of electron-matter interaction, generating **(a)** secondary electrons, **(b)** backscattered electrons and **(c)** characteristic X-rays.

The first observation of a secondary electron emission was reported by Austin and Starke in 1902 [76]. Their work revealed a remarkable phenomenon: by exposing a metal surface to cathode rays (now known as electrons), the number of electrons that are detected exceeds that of the primary beam itself. This suggests that high-energy electrons from the primary beam collide with surface atoms, transferring energy to the bound electrons. Consequently, these electrons acquire sufficient energy to overcome the binding forces of the atoms and are ejected from the material, giving rise to secondary electrons. The energy of secondary electrons is typically below 50 eV, indicating their origin from the surface of the sample. This characteristic renders them highly valuable for the examination of surface morphology using electron detectors in a scanning electron microscope.

On the other hand, backscattered electrons, which are high-energy electrons that undergo elastic scattering by atoms of the sample, provide valuable information about the chemical composition, and the image is often regarded as an atomic number contrast tool. By analysing the intensity and distribution of these electrons, we can discern variations in the elemental composition of the sample, as higher atomic number elements tend to yield stronger backscattered electron signals. Furthermore, backscattered electrons can generate a diffraction pattern known as Kikuchi's lines, which offer insights into the crystallographic orientation and structural properties of the material [77]. For that, a specific EBSD detector must be used.

Finally, the interaction of the electron beam with the atoms of the sample also leads to the emission of characteristic X-rays. This interaction occurs when inner-shell electrons are ejected from the atoms, creating vacancies that are subsequently filled by outer-shell electrons. In this process, the electronic transition from a higher to a lower energy shell occurs, resulting in the emission of radiation. These emitted X-rays possess distinct energies that are specific to the atomic elements present in the sample. By detecting and analysing the energies of these characteristic X-rays, it becomes possible to identify the elements present in the sample and determine their atomic and weight ratios. To carry out this analysis, an energy-dispersive X-ray spectroscopy detector is needed.

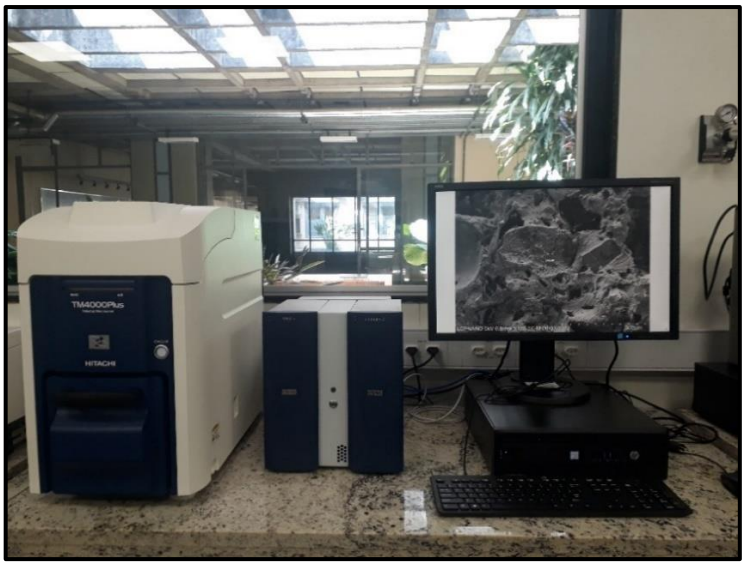

Figure 3.2.3. Hitachi TM4000Plus scanning electron microscope.

All our scanning electron microscopy images were acquired using the Hitachi TM4000Plus microscope, which is located at the LCPNano facility at the Physics Department of Universidade Federal de Minas Gerais (UFMG). This instrument offers middle-resolution imaging capabilities (> 100 nm) utilizing both secondary electron (SE) and/or backscattered electron (BSE) detectors, allowing for versatile imaging modes. The microscope operates at accelerating voltages of 5, 10, or 15 kV, providing flexibility in optimizing imaging conditions based on the sample requirements. Additionally, the setup includes an EDS detector, which facilitates compositional analysis and elemental mapping of the samples. Figure 3.2.3 illustrates the setup consisting of a scanning electron microscope (SEM) on the left, an EDS analyser in the middle, and the computer responsible for controlling the equipment on the right.

3.2.2 Energy-dispersive X-ray Spectroscopy

Energy-dispersive X-ray spectroscopy (EDS) is an analytical technique that utilizes the characteristic X-rays emitted by the atoms of a sample to identify and quantify its constituent elements. The fundamental principle behind EDS is the unique atomic structure of each and all elements, which results in very specific and discrete emission lines in the X-ray spectrum.

Quantitatively, the concentration of a specific element presented in a sample can be determined by analysing the intensities of the characteristic X-ray peaks emitted by that element. By measuring the intensities of these peaks and comparing them to known standards, the concentration of the element in the sample can be accurately calculated. In qualitative analysis, the focus is on identifying the presence of different elements in the sample. This is achieved by matching the observed X-ray peaks in the spectrum to the characteristic peaks associated with specific elements. Each element exhibits a specific set of peaks at well-defined positions in the X-ray spectrum, allowing for their identification and subsequent qualitative analysis.

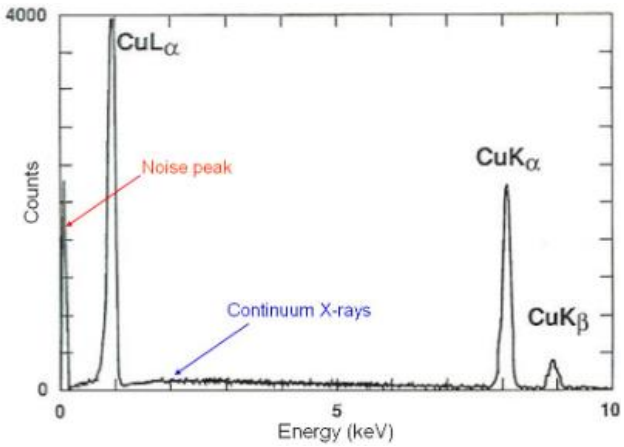

Figure 3.2.4. Typical EDS spectrum of Copper. Figure taken from reference [78].

Figure 3.2.4 shows a typical EDS spectrum of Cooper (Cu). When inner shell electrons are ejected by the electron beam, it occurs an electronic transition. The energy released during an atomic transition corresponds to the difference between the binding energy of the two shells involved. For example, when a primary electron removes an electron from the inner K shell, a vacancy is created and then filled by an electron from the outer L shell, resulting in the emitting of radiation with energy equal to $E_K - E_L$, where E_K and E_L represents the binding energy of the electrons from the K and L shell, respectively. Also, the subsequent electronic transition

creates a vacancy in the L shell, which can be filled by an electron from the M shell, leading to the emission of another radiation, now with energy equal to $E_L - E_M$. Therefore, in atoms with many electrons, a substantial number of X-ray photons can be generated, resulting in a complex X-ray emission spectrum.

Usually, electronic transitions between the K and L electron shells give rise to Kα lines, while transitions between the K and M shells produce Kβ lines. Similarly, transitions between the L and M shells result in Lα lines, and so on. Thus, lines from different electron shells always have distinct energies, leading to different positions in an X-ray emission spectrum. However, in a multiphase material, lines from two different elements may coincide at the same energy position, causing overlapping peaks in the EDS spectrum.

3.2.3 Electron Backscatter Diffraction

Electron Backscatter Diffraction (EBSD) is an additional powerful technique used for analysing the diffraction pattern of backscattered electrons in crystalline systems. An EBSD detector collects backscattered electrons that have undergone coherent Bragg scattering as they interact with a sample. This scattering and diffraction process generates a unique pattern known as Kikuchi lines, which can be analysed to determine the grain orientations, local texture, phase identification, and distributions. EBSD analysis in SEM is now very automated and has found widespread applications in the analysis of crystallography of materials.

The observation of the diffraction phenomenon in backscattered electrons was first reported by Seishi Kikuchi in 1928 [79, 80]. By passing an electron beam through a cleavage face of calcite, a diffraction pattern now known as Kikuchi lines were obtained. In the EBSD experiment, a sufficiently energetic electron beam (around 20 kV) is used to hit the surface of the sample, rotated approximately 70° from its normal position. The backscattered electrons can be thought of as a divergent source of electrons because the electron beam interaction with the sample spread the BSE in all directions within the interaction volume [81]. Part of these backscattered electrons from the beam-sample interaction form a diffraction pattern, which satisfies Bragg's law. Figure 3.2.5 shows a schematic representation of the tilted sample, the electron beam, and the EBSD camera.

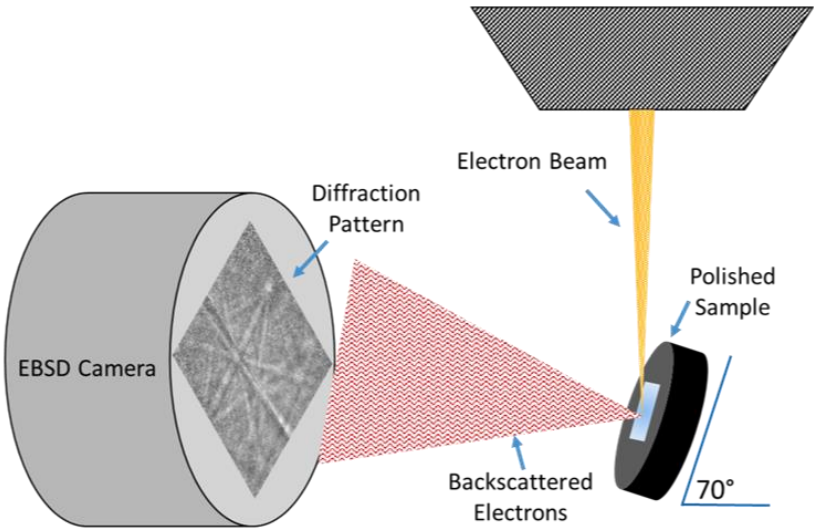

Figure 3.2.5. Schematic representation of Electron Backscatter Diffraction (EBSD) technique. Figure taken from reference [82].

By analysing the Kikuchi lines, it is possible to gain crystallographic information about the sample. One of the main features of the Kikuchi line is the regular arrangement of parallel bright bands offset on a continuous background, as shown in Figure 3.2.6a. Each line corresponds to diffraction occurring in a specific crystalline plane, thus resulting in a family of straight lines in the EBSD detector [82]. Also, each pair of parallel lines represents a family of parallel planes, with a specific value of the interatomic distance d. One of these lines represents the positive plane, while the other represents the negative one. The distance between the two parallel lines is inversely proportional to the interatomic distance.

(a) **(b)**

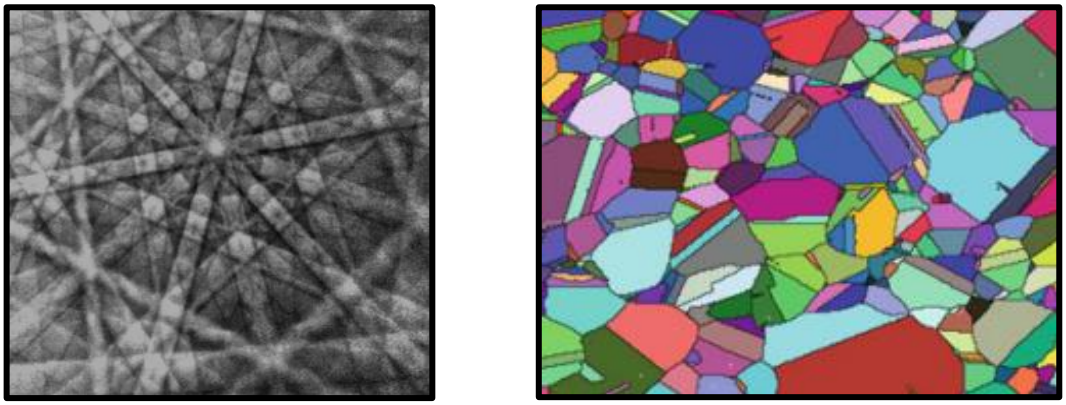

Figure 3.2.6. (a) Kikuchi line of cadmium (Cd) at 20 keV. Figure taken from reference [81]. **(b)** EBSD grain maps of aluminium (Al). Figures taken from reference [83].

The process of indexing Kikuchi lines to their respective crystallographic plane involves using dedicated software, which is then used to calculate and obtain structural information and measure the grain orientation. One method of indexing is to input crystal structure information and microscope parameters into the dedicated computer program. The software then precisely measures the positions of the Kikuchi lines and calculates the angles between each of them [83]. Then, it is possible to compare the simulation with the experimental data, determining the crystallographic orientation, grain boundaries, etc. A typical EBSD grain map is shown in Figure 3.2.6b.

The EBSD measurements shown in this work were conducted at the Brazilian Synchrotron Light Laboratory (LNLS) located in Campinas, Brazil. The instrument is a HELIOS 5 PFIB CXE DUALBEAM Electron Microscope with an imbedded EBSD detector and software.

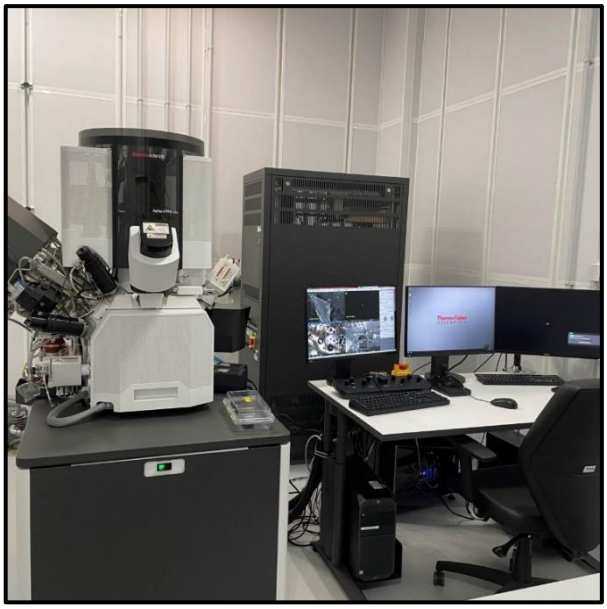

Figure 3.2.7. Microscopic Sample Laboratory (LAM), at the Brazilian Synchrotron Light Laboratory (LNLS).

3.3 X-ray Diffraction

X-ray diffraction (XRD) is an extremally important technique that, since the 20th century, has revolutionized our understanding of matter. Among its landmark discoveries, Max von Laue, Lawrence Bragg, and his father, William Henry Bragg made a significant achievement by unravelling the long-range atomic arrangements of crystalline materials. Through their early studies of elements and simple compounds, they concluded that these crystalline materials possess a regular and periodic arrangement of atoms in three dimensions. Another landmark achievement in X-ray physics was the discovery of the helical shape of DNA, which earned Crick, Watson, and Wilkins the Nobel Prize in Physiology or Medicine, in 1962 [84]. These profound revelations served as the cornerstone of our understanding of matter, and until today, X-ray diffraction stands as a routinely used technique for comprehending the atomic structure in complex materials, including proteins, low-dimensional objects, and more. In this section, an overview of X-ray diffraction is presented.

3.3.1 X-ray Scattering by a Crystal

Considering a three-dimensional crystal where the position $\mathbf{R_n}$ of each unit cell is given by a set of vectors of the form

$$\boldsymbol{R_n} = n_1\mathbf{a_1} + n_2\mathbf{a_2} + n_3\mathbf{a_3}$$

and

$$\boldsymbol{r_j} = x_j\mathbf{a_1} + y_j\mathbf{a_2} + z_j\mathbf{a_3},$$

which consists of the position of the j-atom inside a unit cell.

Assuming that the scattering occurs only one time between the X-rays and the crystal (known as the kinematical approximation), the scattering amplitude can be expressed as the product of the unit cell structure factor and a lattice sum factor, given by:

$$F^{\text{crystal}}(\mathbf{Q}) = \overbrace{\sum_j f_j(\mathbf{Q}) e^{i\,\mathbf{Q}\cdot\mathbf{r}_j}}^{\text{Unit cell structure factor}} \overbrace{\sum_n e^{i\,\mathbf{Q}\cdot\mathbf{R}_n}}^{\text{Lattice sum}}, \tag{3.1}$$

where $\mathbf{Q}$ is the scattering vector defined by

$$\mathbf{Q} = \mathbf{k} - \mathbf{k}' \tag{3.2}$$

and $f_j(\mathbf{Q})$ is the atomic form factor of the j'th atom in the crystal.

The lattice sum on the right side of the equation (3.1) involves phase factors distributed across the complex plane. The sum is finite only if $\mathbf{Q}$ satisfies

$$\mathbf{Q} \cdot \mathbf{R}_\text{n} = 2\pi \cdot \text{integer} \tag{3.3}$$

where n is an integer number. It is convenient, however, to use the reciprocal lattice vector $\mathbf{G}$, defined as

$$\mathbf{G} = h\mathbf{b}_1 + k\mathbf{b}_2 + l\mathbf{b}_3, \tag{3.4}$$

where h, k and l are integers and

$$\mathbf{b}_1 = \frac{\mathbf{a}_2 \times \mathbf{a}_3}{\mathbf{a}_1 \,.\, \mathbf{a}_2 \times \mathbf{a}_3}\ , \mathbf{b}_2 = \frac{\mathbf{a}_3 \times \mathbf{a}_1}{\mathbf{a}_1 \,.\, \mathbf{a}_2 \times \mathbf{a}_3} \text{ and } \mathbf{b}_3 = \frac{\mathbf{a}_1 \times \mathbf{a}_2}{\mathbf{a}_1 \,.\, \mathbf{a}_2 \times \mathbf{a}_3}\ . \tag{3.5}$$

Thus,

$$\mathbf{G} \cdot \mathbf{R}_\text{n} = 2\pi \cdot \text{integer} = 2\pi(hn_1 + kn_2 + ln_3). \tag{3.6}$$

The solution of equation (3.3) with the condition (3.6) is:

$$\mathbf{Q} = \mathbf{G} \tag{3.7}$$

and it is called the Laue condition. The physical interpretation of equation (3.7) is that the structure factor $F^{\text{crystal}}(\mathbf{Q})$ will vanish unless the scattering vector $\mathbf{Q}$ is equal to one of the reciprocal lattice vectors $\mathbf{G}$ [85]. Therefore, X-ray scattering from a crystal is confined to distinct points in reciprocal space. The intensity is the absolute square of the structure factor,

$$I = \left|F^{\text{crystal}}(\mathbf{Q})\right|^2, \tag{3.8}$$

and through the analysis of the intensities of the scattered X-rays, it becomes possible to determine the positions of the atoms within the unit cell.

3.4 Scanning Tunneling Microscopy and Spectroscopy

Scanning Tunnelling Microscopy (STM) and Spectroscopy (STS) have proven to be extremely powerful tools for analysing and resolving local electronic and atomic structures with a nanometer-scale resolution. Invented by Gerd Binnig and Heinrich Rohrer, who were awarded the 1986 Nobel Prize in Physics [87, 88], the field of scanning tunneling microscopy has witnessed an expansion and has paved the way for numerous groundbreaking discoveries across condensed-matter physics, chemistry, and biology. Furthermore, scanning tunneling spectroscopy has emerged as an indispensable tool for examining the local electronic density of states in various materials, such as graphene [89], topological insulators [90-92], semiconductors [93, 94], transition metal dichalcogenides [95, 96], and numerous other biological compounds [97-98]. Before discussing the functionality of a scanning tunneling microscope, it is prudent to provide an overview of the foundational principle underlying STM and STS: the tunneling phenomenon.

3.4.1 The Tunneling Phenomenon

The tunneling phenomenon occurs when a particle, like an electron, encounters a potential barrier that, classically, would not have enough energy to overcome. In quantum mechanics, however, there is a probability for the particle to tunnel through the barrier and emerge on the classically forbidden region. Depending on the initial conditions, such as the size and height of the barrier, as well as the energy of the particle, the quantum tunneling phenomenon can become significant enough to be non-negligible. In a scanning tunneling microscope, for example, the tip is significantly closer to the sample, and by applying a potential between the tip and the sample, tunnel electrons can flow.

Consider a potential energy described as

$$V(x) = \begin{cases} 0, & x < -a \\ V_0, & -a < x < a \\ 0, & x > a. \end{cases} \tag{3.9}$$

Figure 3.4.1 provides a visual representation of the potential energy defined by equation (3.9). The region $-a < x < a$ is classically forbidden if the energy (E) of the incident particle is lower than the potential barrier height (V_0).

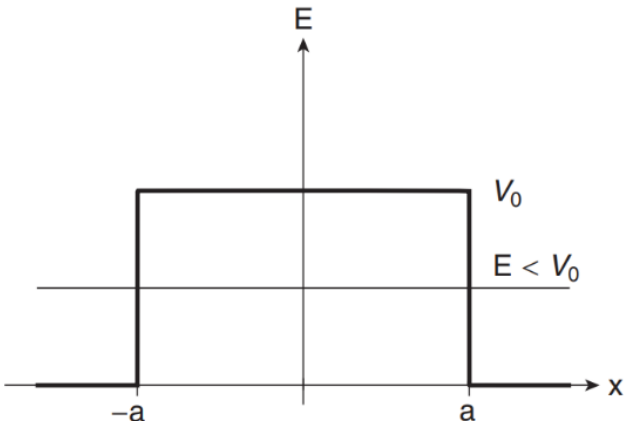

Figure 3.4.1. A representation of the potential barrier described by equation (3.9). An incident particle is depicted having energy E lower than the height of the potential barrier V_0. Figure taken from reference [99].

In quantum mechanics, however, the particle is described by Schrödinger equation, whose time-independent form is

$$-\frac{\hbar^2}{2m}\frac{d^2\psi(x)}{dx^2}+V(x)\psi(x)=E\psi(x), \tag{3.10}$$

which is an eigenvalue equation of the form $H|\psi\rangle = E|\psi\rangle$. The symbol $\hbar$ is the reduced Planck constant, while m is the mass of the particle with energy E.

By replacing the potential $V(x)$ described in equation (3.9) into equation (3.10), we have distinct eigenvalue equations within the three different regions:

$$\begin{aligned} -\frac{\hbar^2}{2m}\frac{d^2\psi_E(x)}{dx^2}+V_0\psi(x)&=E\psi_E(x), && |x|<a \\ -\frac{\hbar^2}{2m}\frac{d^2\psi_E(x)}{dx^2}&=E\psi_E(x), && |x|>a. \end{aligned} \tag{3.11}$$

It is convenient to define two parameters q and k as

$$q=\frac{1}{\hbar}\sqrt{2m(V_0-E)} \tag{3.12}$$

and

$$k=\frac{1}{\hbar}\sqrt{2mE}. \tag{3.13}$$

Thus, one can simplify equations (3.11) as

$$\begin{aligned} \frac{d^2\psi_E(x)}{dx^2}&=q^2\psi_E(x), && |x|<a \\ \frac{d^2\psi_E(x)}{dx^2}&=k^2\psi_E(x). && |x|>a \end{aligned} \tag{3.14}$$

Assuming that the particle is incoming from the left, so the wavefunction is initially propagating in the x-direction, the general solution to these equations are

$$\psi_E(x) = \begin{cases} A_1 e^{ikx} + A_2 e^{-ikx}, & x < -a \\ B_1 e^{qx} + B_2 e^{qx}, & -a < x < a \\ C e^{ikx}, & x > a. \end{cases} \tag{3.15}$$

The parameters defined in equations (3.12) and (3.13) hold significant physical meaning, representing the decay constant (q) and the momentum (k) of the particle. These constants are fundamental to understanding the general solution presented in equation (3.15).

Physically, the positive exponential function in the general solution for the interval $x < -a$ represents an incident wave propagating from the left to the right with momentum $p = \hbar\, k$, colliding with the barrier. On the other hand, the negative exponential in the same solution indicates a wave that reflects back by the barrier and now propagates in the $-x$ direction. Moreover, considering the solution for the interval $x > a$, we encounter the wavefunction that was successfully transmitted through the barrier, propagating in the positive x direction after the interaction with the potential barrier. Finally, the non-trivial solution from $-a < x < a$ represents the interaction of the wavefunction inside the potential barrier. As we shall see, there is a probability of the wavefunction transmitting through the classically forbidden region of the potential barrier. Figure 3.4.2 shows a representation of the real part of the wavefunction interacting with a potential barrier.

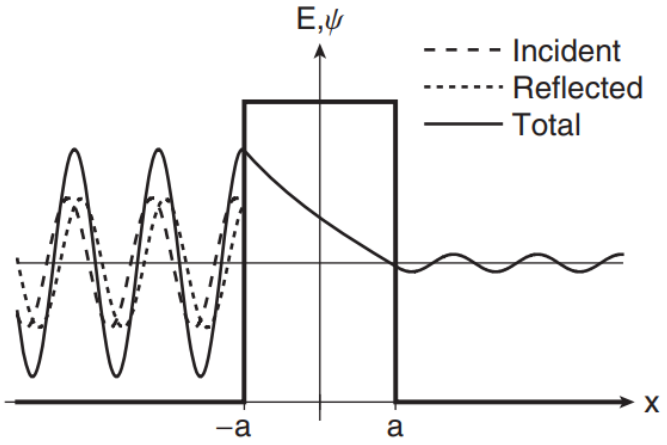

Figure 3.4.2. This graphical representation illustrates the real part of the wavefunction as a particle tunnel through a square barrier. Figure taken from reference [99].

To ensure the continuity of the wavefunction and applying the boundary conditions of this problem, we must calculate the $d\psi(x)/dx$. This condition is as follows:

$$\psi(-a): A_1 e^{-ika} + A_2 e^{ika} = B_1 e^{-qa} + B_2 e^{qa},$$

$$\psi(a): B_1 e^{qa} + B_2^{-qa} = C e^{ikx},$$

$$\left.\frac{d\psi(x)}{dx}\right|_{x=-a} : ikA_1 e^{-ika} - ikA_2 e^{ika} = qB_1 e^{-qa} - qB_2 e^{qa},$$

$$\left.\frac{d\psi(x)}{dx}\right|_{x=+a} : qB_1 e^{qa} - qB_2^{-qa} = ikC e^{ika}.$$

As mentioned earlier, the coefficient C from the general solution represents the amplitude of the wavefunction after it has been transmitted through the potential barrier, while A_1 corresponds to the amplitude of incident wavefunction approaching from the left. Therefore, to calculate the probability of the particle being transmitted through the potential barrier, we need to compute $|C|^2/|A_1|^2$, which is known as the transmission coefficient. This computation results in a real number, representing the probability of the particle with energy $E < V_0$ to successfully tunnel through the potential barrier. Thus,

$$T = \frac{|C|^2}{|A_1|^2} = \frac{1}{1 + \frac{V_0^2}{4E(V_0 - E)} \sinh^2\left(\frac{2a}{\hbar}\sqrt{2m(V_0 - E)}\right)}. \tag{3.16}$$

In the context of scanning tunneling microscopy, the particles in question are electrons, and the potential barrier can be either vacuum or even air. Consequently, the probability of electron tunneling from the tip to the sample, and vice versa, are closely related to the width of the potential barrier, which physically represents the distance between the tip and the sample. Figure 3.4.3 illustrates the physical interpretation of the tunneling concept in the context of scanning electron microscopy.

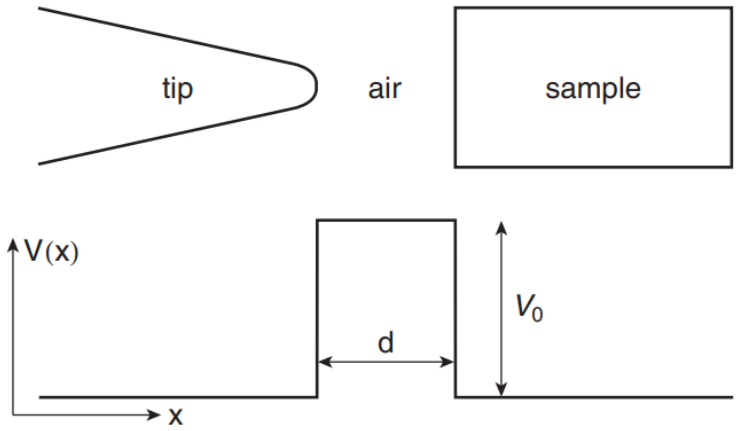

Figure 3.4.3. Schematic diagram of the tunneling phenomenon in the context of scanning tunneling microscopy. The potential barrier can be either the vacuum or air. Figure taken from reference [99].

3.4.2 Scanning Electron Microscope

Scanning tunneling microscopy is an imaging technique based on the quantum tunneling phenomenon. A probe tip, usually made of tungsten (W) or platinum-iridium (Pt-Ir) alloy, is moved in three dimensions using perpendicular piezoelectric translators with sub-nanometer precision. The piezoelectric translators allow the precise control and positioning of the sample or the tip, allowing them to be brought into proximity within a distance of 1 nm. This exceptional level of control enables the probing of atomic and molecular structures with unparalleled precision, usually achieving a nanometer and atomic scale resolution. By applying a bias voltage between the tip and the sample, a tunneling current will flow. Figure 3.4.4 shows a schematic diagram of the piezoelectric translators, the tip, and the sample.

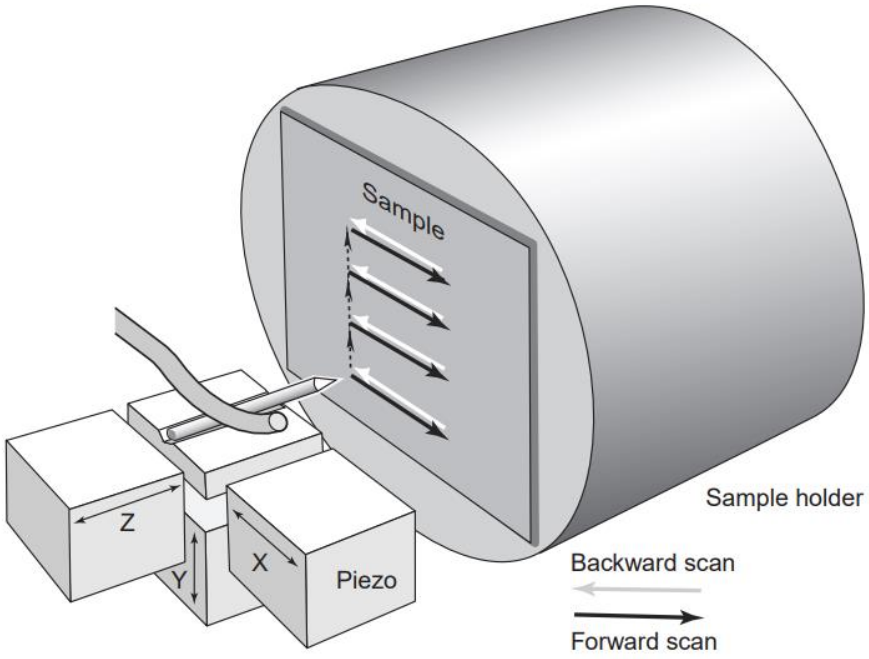

Figure 3.4.4. A schematic diagram of a scanning tunneling microscope. The crucial components of the STM are depicted, including the piezo drivers responsible for the precise positioning of the tip. Also, the piezo drivers are responsible for scanning the sample, enabling the acquisition of high-resolution images and spectroscopic data. Figure taken from reference [100].

Usually, a scanning tunneling microscope can operate in two distinct modes: constant current and constant height mode. To ensure that the tunneling current is constant during a scan, an electronic feedback control is mandatory. When the absolute value of the tunneling current exceeds a predefined reference value, typically referred to as the setpoint, the tip must be carefully retracted from the sample so that the tunneling current remains constant. On the other hand, if the absolute value of the tunneling currents is smaller than the setpoint, the tip needs to be brought closer to the sample. Thus, a constant tunneling current measurement provides a height image made by recording the position of the Z-feedback loop as a function of the XY-piezo position. On the other hand, in constant height mode, the feedback loop is turned off and the distance between the tip and the sample remains constant during the scan, thus making a measurement of the variation of the tunneling current. Figure 3.4.5 shows a schematic diagram of both constant current and constant height modes.

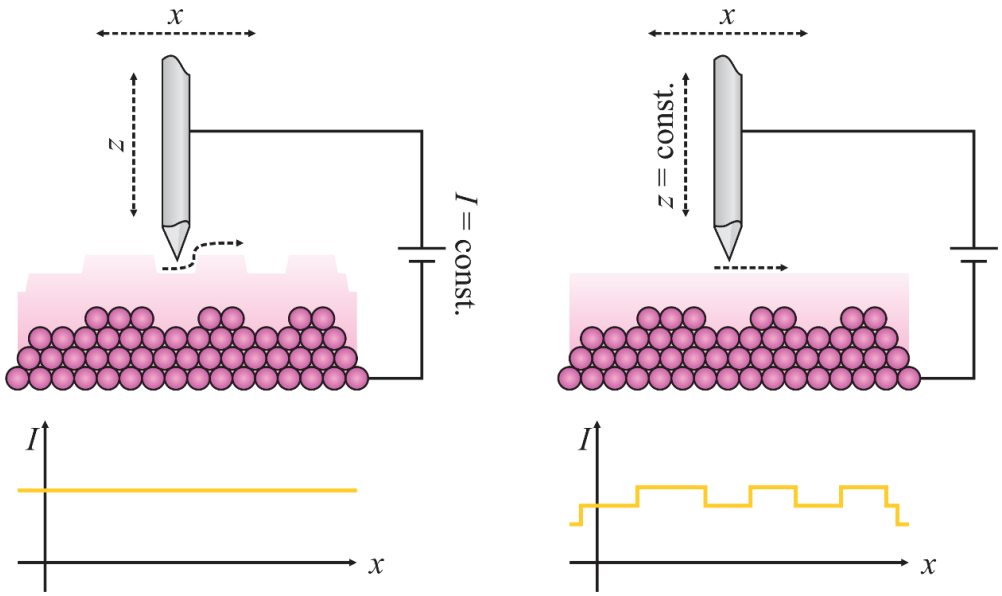

Figure 3.4.5. (a) In the tunneling current constant mode, the feedback loop continuously adjusts the distance between the tip and the sample during the scanning process, thus making the tunneling current constant. **(b)** In the height constant mode, the feedback loop is disabled, and the tip does not move in the z direction. Figure adapted from reference [100].

In this study, we use a Nanosurf Easyscan 2 STM, which can be seen in Figure 3.4.6. This microscope operates with tip bias, implying that the bias voltage is applied at the tip rather than the sample. Thus, throughout this work, we adopt the convention that the sample is virtually grounded while the bias voltage (V) is applied in the tip. This approach is employed to ensure accuracy and completeness throughout all the STM and STS results of this work.

Figure 3.4.6. Nanosurf Scanning Tunneling Microscope, Easyscan 2. Photo taken in the Nanoscopia-UHV laboratory, at UFMG.

When a positive bias is applied to the tip, the Fermi level of the tip undergoes a shift to $E_F - eV$. As the sample is grounded, this bias voltage induces electron tunneling from the occupied states of the sample to the unoccupied states of the tip. Conversely, when a negative bias is applied to the tip, the Fermi level of the tip shifts to $E_F + eV$, leading to electrons tunneling from the occupied states of the tip to the unoccupied states of the sample. Figure 3.4.7 visually demonstrates the tunneling phenomenon under varying bias conditions, enhancing the understanding of the physical process.

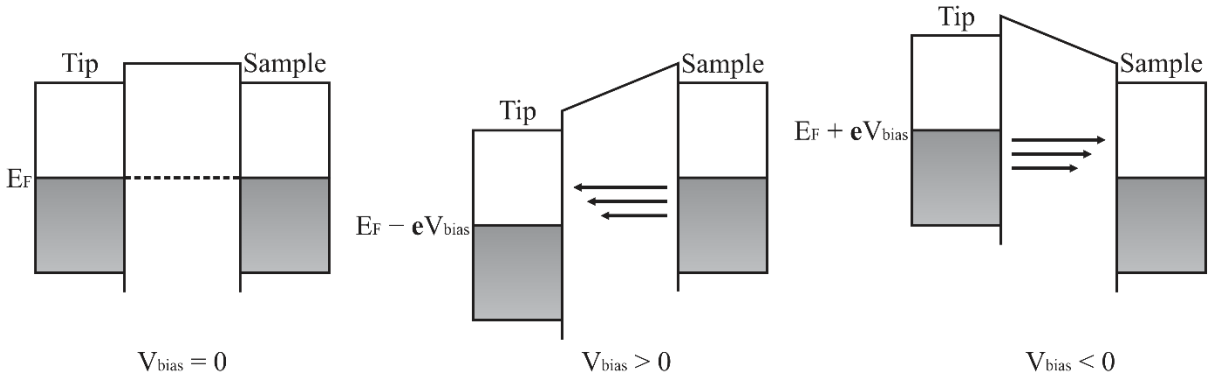

Figure 3.4.7. Tunneling phenomenon under zero, positive, and negative bias conditions. When a positive bias is applied, electrons tunnel from the occupied states of the sample to the unoccupied states of the tip. In contrast, under negative bias, electrons tunnel from the occupied states of the tip to the unoccupied states of the sample. At zero bias, no tunneling occurs between the sample and the tip.

3.4.3 The Bardeen theory of Tunneling

The most widely used theory to explain the tunneling phenomenon in scanning tunneling microscopy was developed by John Bardeen, first published in 1961 [101]. Initially, his goal was to understand the phenomenon of superconductivity reported by Giaever and Megerle [102]. However, it was not until 1983 that J. Tersoff and D. R. Hamann applied the Bardeen theory of tunneling within the context of STM [103].

Assuming that the STM tip and the sample are significantly distant from each other, we can write two time-dependent Schrödinger equations for the tip and the sample:

$$i\hbar\frac{\partial\Psi_{\mathrm{T}}}{\partial t} = \left[\frac{-\hbar}{2m}\frac{\partial^2}{\partial x^2} + V_T(x)\right]\Psi_{\mathrm{T}} \tag{3.17}$$

and

$$i\hbar\frac{\partial\Psi_{\mathrm{S}}}{\partial t} = \left[\frac{-\hbar}{2m}\frac{\partial^2}{\partial x^2} + V_S(x)\right]\Psi_{\mathrm{S}}, \tag{3.18}$$

where $V_T(x)$ and $V_S(x)$ are the potential energy of the tip and the sample, respectively. The general solution for the equations (3.17) and (3.18) are

$$\Psi_{\mathrm{T}} = \psi_\mu^T e^{-\frac{iE_\mu^T t}{\hbar}} \tag{3.19}$$

and

$$\Psi_S = \psi_\nu^S e^{-\frac{iE_\nu^S t}{\hbar}}, \tag{3.20}$$

where ψ_μ^T and ψ_ν^S are the wavefunctions of the time-independent Schrödinger equation of the tip and the sample, respectively.

As seen before, when the STM tip and the sample approach each other, the potential barrier width diminishes, leading to an increase in the transmission coefficient T. Consequently, the probability of electrons tunneling between the sample and the tip rises significantly.

Now, the electronic structure of the sample and the tip are not independent as they get closer, and the wavefunction Ψ is the general solution of the coupled Schrödinger equation,

$$i\hbar\frac{\partial\Psi}{\partial t} = \left[\frac{-\hbar}{2m}\frac{\partial^2}{\partial x^2} + V_S(x) + V_T(x,t)\right]\Psi. \tag{3.21}$$

In this approach, it is necessary to introduce a temporal dependency in the potential of the tip, given that the tip is progressively brought closer to the inert sample. Considering that for $t \to -\infty$, the tip and sample remain sufficiently separated to prevent any electronic interaction between them, and the equations (3.17) and (3.18) are valid. If the tip gradually approaches the sample, we can reasonably assume that $V_T(x,t)$ exhibits an adiabatic behavior [104, 105]:

$$V_T(x,t) = e^{\frac{\eta t}{\hbar}} V_T(x), \tag{3.22}$$

where η is a positive integer.

This adiabatic behavior implies that the potential of the tip evolves slowly and smoothly over time as it comes closer to the sample. As a result, the electronic system has sufficient time to adapt to these changes in the potential, ensuring a more stable and accurate description of the electron behavior during the approach.

The general solution of the equation (3.23) involves the wavefunctions ψ_ν^S and ψ_μ^T:

$$\Psi = \psi_\nu^S e^{-\frac{iE_\nu^S t}{\hbar}} + \sum_{\mu=1}^{\infty} c_\mu(t) \psi_\mu^T e^{-\frac{iE_\mu^T t}{\hbar}}, \tag{3.23}$$

and coefficient $c_\mu(t)$ was introduced due to the temporal dependency of the V_T.

A fundamental assumption in Bardeen´s theory of tunneling is that the sets of wavefunctions ψ_ν^S and ψ_μ^T are orthogonal,

$$\int \psi_\nu^S \psi_\mu^T \, d^3\boldsymbol{r} \cong 0. \tag{3.24}$$

Assuming that $c_\mu(-\infty) \to 0$ and the orthogonality of the wavefunctions, we can replace the general solution (3.23) into equation (3.21), resulting in:

$$\mathrm{i}\hbar \sum_{\mu=1}^{\infty} \frac{dc_\mu(t)}{dt}\, \psi_\mu^T e^{-\frac{iE_\mu^T t}{\hbar}} = V_T \psi_\nu^S e^{-\frac{i\left(E_\nu^S + i\eta\right)t}{\hbar}} + V_S \sum_{\lambda=1}^{\infty} c_\lambda(t) \psi_\lambda^T e^{-\frac{iE_\lambda^T t}{\hbar}}. \tag{3.25}$$

The second term on the right-hand side of the equation (3.25) is an infinitesimal quantity. Therefore, we can neglect it:

$$\mathrm{i}\hbar \frac{dc_\mu(t)}{dt} = \int_{x>x_0} \psi_\nu^S V_T\, \overline{\psi_\mu^T}\, e^{-\frac{i\left(E_\nu^S - E_\mu^T + i\eta\right)t}{\hbar}}\, d^3\boldsymbol{r}. \tag{3.26}$$

It is convenient to define a tunneling matrix element as

$$M_{\nu\mu} = \int_{x>x_0} \psi_\nu^S V_T\, \overline{\psi_\mu^T}\; d^3\boldsymbol{r}, \tag{3.27}$$

and the coefficient $c_\mu(t)$ can be written as

$$c_\mu(t) = M_{\nu\mu} \frac{e^{-\frac{i\left(E_\nu^S - E_\mu^T + i\eta\right)t}{\hbar}}}{\left(E_\nu^S - E_\mu^T + i\eta\right)}. \tag{3.28}$$

Calculating $\left|c_\mu(t)\right|^2$, which represents the probability of the electrons described by the wavefunction ψ_ν^S to populate the state ψ_μ^T,

$$|c_\mu(t)|^2 = |M_{\nu\mu}|^2 \frac{e^{\frac{2\eta t}{\hbar}}}{\left(E_\nu^S - E_\mu^T\right)^2 + \eta^2}. \tag{3.29}$$

Finally, it is possible to calculate the probability of the tunneling phenomenon per unit of time, defined as:

$$P_{\nu\mu}(t) = \frac{d}{dt}|c_\mu(t)|^2 = \frac{2\eta}{\hbar}\,|M_{\nu\mu}|^2 \frac{e^{\frac{2\eta t}{\hbar}}}{\left(E_\nu^S - E_\mu^T\right)^2 + \eta^2}. \tag{3.30}$$

If the tip is far away from the sample, so $\eta \to -\infty$, the probability of the tunneling phenomenon to occur is null. However, if the tip is close enough to the sample, $\eta \to 0$,

$$P_{\nu\mu}(t) = \frac{2\pi}{\hbar}\left|M_{\nu\mu}\right|^2 \delta\left(E_\nu^S - E_\mu^T\right), \tag{3.31}$$

where $\delta(x) = \frac{1}{\pi}\lim \frac{\eta}{x^2+\eta^2}$.

3.4.4 Scanning Tunneling Spectroscopy

Scanning tunneling spectroscopy (STS) is a local probe technique capable of inferring information about the electronic structure of materials. Usually, there are two distinct spectroscopy modes in an STM microscope: the current-voltage and the distance-current spectroscopies. For the current-voltage spectroscopy, the feedback control is disabled, making the distance between the tip and the sample constant. Then, the bias voltage is varied, making it possible to collect the tunneling current as a function of the applied bias. On the other hand, distance-current spectroscopy consists of a measurement of the tunneling current as the distance between the tip and the sample varies, within a constant bias voltage. The distance-current spectroscopy is particularly important for the study of heterogeneities in the electronic structure of materials, such as defects, impurities, etc. However, in this section, we will study in detail the current-voltage spectroscopy because, as we will see, the derivative of the tunneling current as a function of the bias voltage is proportional to the local electronic density of states.

The concept of density of states (DOS) is a fundamental aspect of quantum mechanics and represents the number of available electronic quantum states per energy in a given system. It serves as a crucial quantity in understanding the electronic behavior and energy distribution of materials. Here, we are going to denote the density of states of the tip and the sample as $\rho_T\left(E_\mu^T\right)$ and $\rho_S(E_\nu^S)$, respectively.

The total tunneling current [106] is

$$I = \frac{4\pi e}{\hbar} \int_0^{eV} \rho_T(E_F^T - eV + \epsilon)\rho_S(E_F^S + \epsilon)|M|^2 \, d\epsilon, \tag{3.32}$$

where e is the elementary charge and ϵ is an integration parameter. An approximation of equation (3.32) can be achieved by considering that the $|M|^2$ is constant in the integral range. Thus, the tunneling current will be

$$I \propto \int_0^{eV} \rho_T(E_F^T - eV + \epsilon)\rho_S(E_F^S + \epsilon) \, d\epsilon. \tag{3.33}$$

The derivative of the tunneling as a function of the bias voltage is then:

$$\frac{dI}{dV} \propto \rho_T(E_F^T - eV)\rho_S(E_F^S) \, , \tag{3.34}$$

$$\frac{dI}{dV} \propto \rho_T(E_F^T + eV)\rho_S(E_F^S) \, . \tag{3.35}$$

Scanning tunneling spectroscopy is a localized technique, where tunneling spectra are acquired from very small regions of the sample. As a result, it is common to refer to the local density of states (LDOS) when discussing the STS measurements. It is convenient to write equations (3.34) and (3.35) as follows:

$$\frac{dI}{dV} \propto LDOS_{tip}(E_F^T - eV)LDOS_{sample}(E_F^S) \, , \tag{3.36}$$

$$\frac{dI}{dV} \propto LDOS_{tip}(E_F^T + eV)LDOS_{sample}(E_F^S) \, . \tag{3.37}$$

Remembering that the sample is grounded, equation (3.36) represents a positive bias voltage V applied to the tip, leading to electrons tunneling from the occupied states of the sample to the unoccupied states of the tip. Thus, the dI/dV curve is proportional to the local

density of states of the tip at the energy $E_F^T - eV$ and to the local density of states of the sample at the Fermi level E_F^S. On the other hand, equation (3.37) corresponds to a negative bias voltage V applied to the tip, resulting in electrons tunneling from the occupied states of the tip to the unoccupied states of the sample. Furthermore, the dI/dV curve is now proportional to the density of states of the tip at the energy $E_F^T + eV$ and to the local density of states of the sample at the Fermi level E_F^S.

Generally, we consider that the local density of states of the tip is approximately constant, and then the dI/dV equations (3.36) and (3.37) are proportional to the local density of states of the sample itself. Based on this assumption, these dI/dV equations are directly proportional to the local density of states of the sample.

In the Nanosurf Easyscan 2 STM, a current-voltage spectroscopy measurement is divided into five steps. The first step involves setting the tip voltage at a resting potential of 0 V. Then, the tip voltage is adjusted to a positive value, such as 1 V. Subsequently, the tip voltage slowly moves from a positive value to a negative value. During this gradual voltage decrease, current measurements are recorded to capture the I-V curve. Figure 3.4.8 shows the tip voltage as a function of the time during a STS measurement.

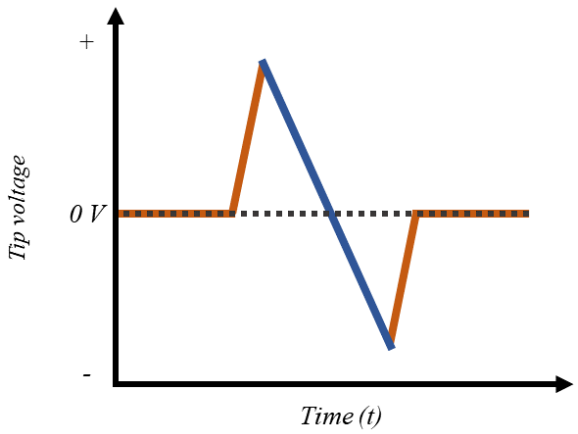

Figure 3.4.8. Representation of the tip voltage during an STS measurement. The orange lines represent the tip voltage while the tunneling current is not recording. The blue line represents the tip voltage during the measurement of the tunneling current. It starts in the positive value and is slowly moved into the negative value. Once the spectrum is acquired, the tip voltage returns to the resting potential. Figure adapted from reference [100].

Before diving into the physical interpretation of scanning tunneling spectroscopy curves, it is crucial to provide an overview of the band theory of solids and understand the electronic structure of materials classified as metals, semimetals, semiconductors, and insulators. Their electronic properties can be determined by examining the I-V and dI/dV curves.

One of the groundbreaking discoveries in quantum mechanics is that the energy levels of an electron within an atom are discrete. This is due to the fundamental exclusion principle established by Wolfgang Pauli, which states that two electrons in an isolated atom cannot have the same set of quantum numbers. As a result, only two electrons can occupy the same energy level, as long as they have opposite spins. However, when we consider a large number of atoms that are arranged to make up a solid, the high number of electronic states are now closely spaced, forming bands. Figure 3.4.9 shows a schematic diagram of the formation of bands, which are made up of discrete energy levels very close to each other. These energy bands allow electrons to occupy a wide range of energy states, resulting in a more complex and interconnected electronic behavior within the solid compared to isolated atoms.

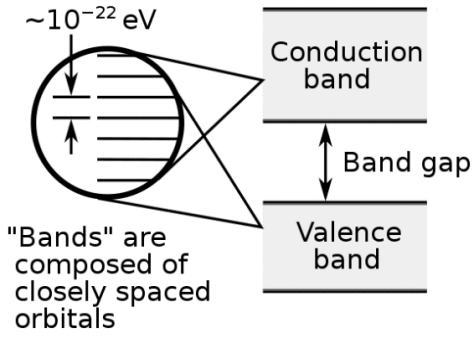

Figure 3.4.9. A representation of the energy levels of an electron in a semiconductor/insulator. The bands are composed of a closely spaced orbitals. Figure adapted from reference [107].

In the band theory of solids, the band structure describes the electronic states that electrons can or cannot occupy. We define the valence band as the highest range of electron energies in which electrons are normally present, while the conduction band is the lowest range of unoccupied electronic states. Moreover, there may be an energy range where no electronic states are available. These are called forbidden bands or band gaps.

In metals and semimetals, the Fermi level represents the highest energy level occupied by electrons at absolute zero temperature. However, the differentiation between the valence and conduction bands becomes insignificant in metals, since the conduction takes place in one or more partially filled bands. Thus, a metal is characterized by partially filled bands, indicating the presence of available energy states for electrons to move freely. On the other hand, a semimetal possesses a small overlap between the top of the valence band and the bottom of the conduction band, typically situated in a different region of momentum space. Because of the overlap between these bands, a semimetal has no band gap.

Semiconductors and insulators possess a band gap in their electronic structure, with the Fermi level inside this forbidden region. Typically, insulators possess a larger band gap ($>$ 4 eV) than semiconductors ($<$ 4 eV), making it extremely hard to excite valence electrons into the conduction band. On the other hand, semiconductors have a narrower band gap, permitting controlled electron movement under certain conditions, which gives them intermediate electrical conductivity characteristics. At zero temperature, the valence band of both types of material is completely filled, while the conduction band is empty. The first line of Figure 3.4.10 illustrates a simplified band diagram of metals, semimetals, semiconductors, and insulators.

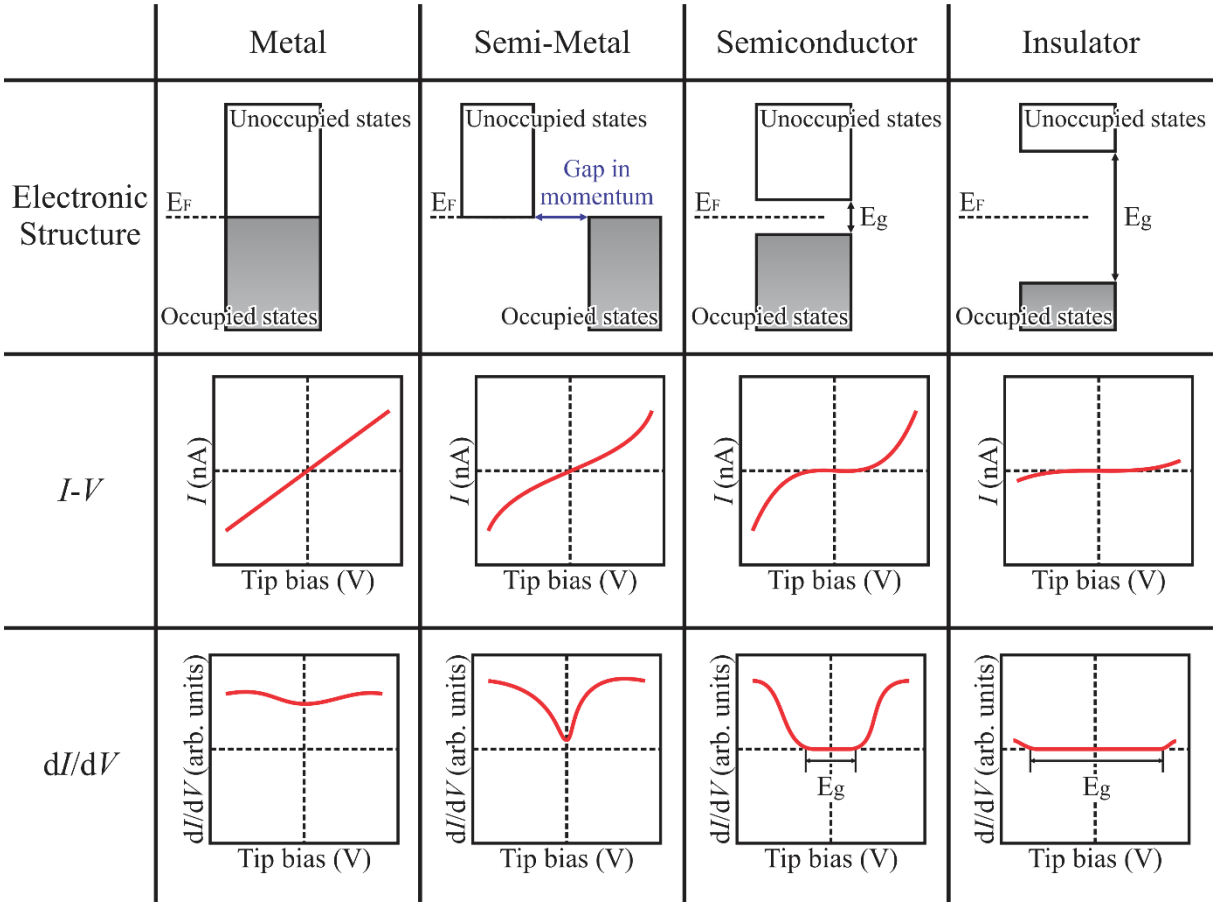

Figure 3.4.10 Schematic diagram of the electronic structure and the typical I-V and dI/dV curves of metals, semimetals, semiconductors and insulators. Figure adapted from reference [108].

Furthermore, Figure 3.4.10 shows the typical I-V and dI/dV curves for metals, semimetals, semiconductors, and insulators. By analyzing these curves, it is possible to study and classify the electronic structure of a desired material, estimate the band gap and, as we have seen in equations (3.36) and (3.37), obtain the local density of states of the sample.

In a semiconductor sample, applying a positive tip bias will populate the empty states of the tip with the electrons from the occupied states of the sample, consequently measuring the valence band of the sample. On the other hand, when a negative tip bias is applied, the electrons from the occupied states of the sample will populate the empty states of the semiconductor, resulting in the measurement of the conduction band of the semiconductor. Figure 3.4.11. shows a semiconductor-like tunneling spectrum, with the band gap and valence and conduction band depicted.

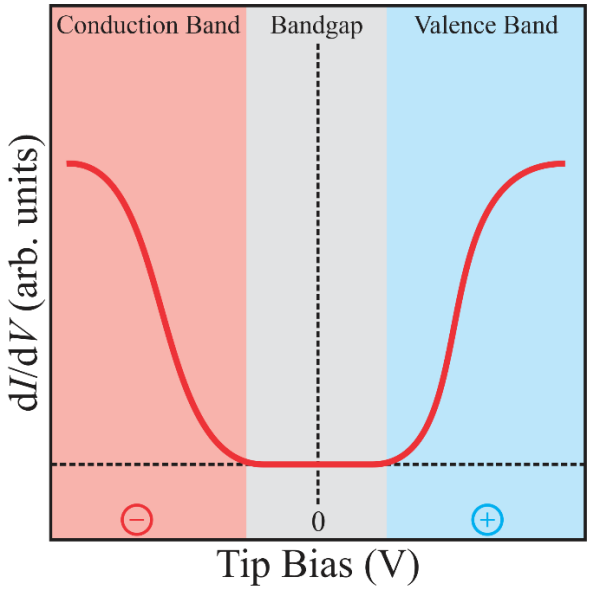

Figure 3.4.11. A typical semiconductor dI/dV spectrum. The local density of states in the conduction band depicted on a red background, and the valence band illustrated on a blue background. The band gap is represented by a grey background.

It is convenient, however, to depict scanning tunneling spectra in terms of energy (eV) rather than the bias voltage (V). To convert, we recall the relationship between energy and voltage, $E = qV$. Thus, considering q as the elementary charge of the electron,

$$E = -eV. \tag{3.38}$$

Practically, one just need to multiply the x-axis of a tunneling spectrum by $-e$. Consequently, the positions of the valence and conduction bands will be inverted in comparison with typical tip bias spectra, with positive energy representing the conduction band and negative energy representing the valence band. Figure 3.4.12 shows a typical semiconductor dI/dV spectrum as a function of energy in electronvolt.

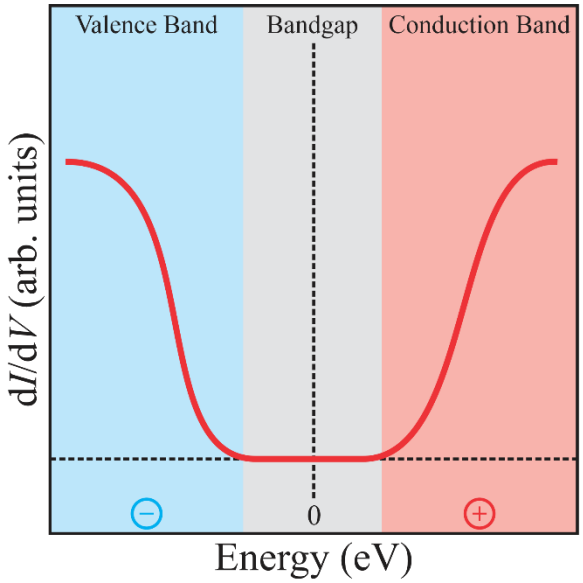

Figure 3.4.12. Semiconductor dI/dV spectrum as a function of the electrons energy.

Expressing the tunneling spectrum as a function of energy in electronvolt offers convenience as it allows for a more direct comparison with computational data of the calculated electronic density of state. Therefore, all tunneling spectra presented in this work will be plotted as a function of energy to facilitate a more straightforward analysis.

4. RESULTS AND DISCUSSION

In this chapter, we offer a comprehensive investigation and in-depth discussion regarding the crystal growth, atomic structure, and electronic properties of two multiphase indium selenide samples. Firstly, we discuss the crystal growth parameters used for the synthesis of both samples, while offering possible explanations for the variations observed in the phase and polymorph identification.

Our investigation of the atomic structure was conducted using a range of experimental techniques, including Scanning Electron Microscopy (SEM), Energy Dispersive X-ray Spectroscopy (EDS), Powder X-ray Diffraction (XRD), and Electron Backscatter Diffraction (EBSD). By this analysis, it is possible to understand how the growth parameters such as temperature and time affected the crystalline phases and polymorphs. Moreover, the electronic local density of states of such materials was probed by using Scanning Tunneling Microscopy (STM) and Spectroscopy (STS).

4.1 Crystal Growth and Structural Characterization

As we have seen, achieving a monocrystalline sample of indium selenide using the Bridgman method can present certain challenges, primarily due to the complex nature of the indium-selenium binary phase diagram (shown in Figure 2.1). Therefore, we decided to take advantage of this property and study the crystal growth of multiphase indium selenide by deliberately manipulating the temperature during the growth process to align with specific regions of the phase diagram. We have successfully obtained two crystals featuring multiple phases and polymorphs within a single growth process.

The first sample was grown using an evacuated and sealed quartz tube containing stoichiometric amounts of In and Se to crystallize the In_2Se_3 phase. The pressure inside the tube during the sealing process was maintained at 70 milliTorr. The sealed quartz tube was heated to 900°C for one day, a temperature higher than the boiling point of selenium. This approach aimed to increase the internal selenium pressure, thereby mitigating defects and minimizing the formation of pores within the crystal structure. Subsequently, the furnace temperature was

lowered to 650°C for one day and then further reduced to 250°C for an additional day. Finally, the sample was allowed to cool to room temperature naturally.

For the second sample, the quartz tube containing In and Se was evacuated until it reached a pressure of 80 milliTorr, after which it was sealed. We decided to initiate the growth process at the same starting temperature of 900°C. However, rather than altering the temperature to obtain specific polymorphs, the sample was held at 900°C for a period of three days. After that, the furnace was turned off, causing the temperature of the crystal to gradually decrease until it reached room temperature within three hours. During this abrupt cooling process, the crystal passed through all polymorph crystallization temperatures of the phase diagram above room temperature. Thus, this process was used to possibly investigate other phases. Figure 4.1.1 exhibits photographs of both samples of indium selenide synthesized for this work.

(a) **(b)**

Figure 4.1.1. Photographs of the synthesized materials; **(a)** First sample. **(b)** Second sample.

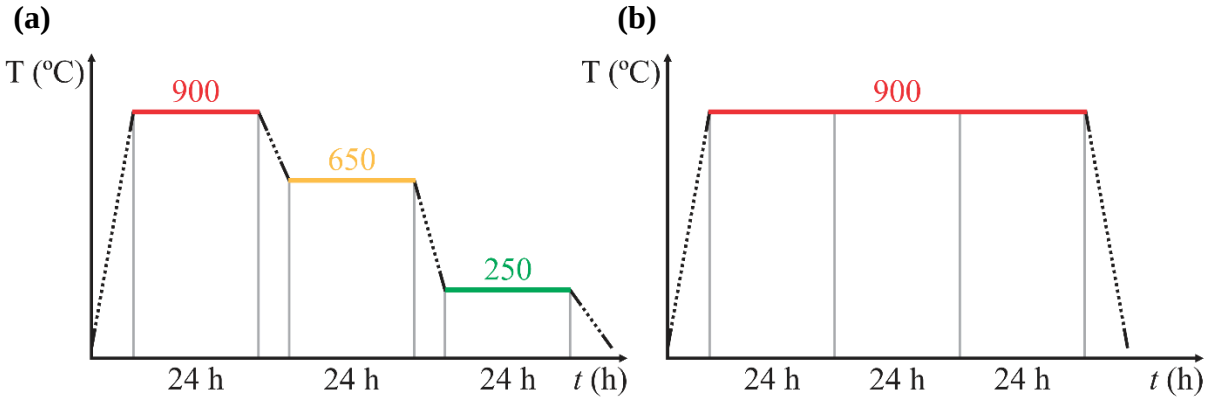

Figure 4.1.2. Temperature as a function of time **(a)** First sample. **(b)** Second sample. The dotted lines represent the heating and cooling processes.

We present the temperature of the furnace as a function of time in the figure above, with the dotted lines representing the heating and cooling processes. In Figure 4.1.2a, we observe a growth process characterized by temperature steps, from 900°C to 650°C and then from 650°C to 250°C. The initial temperature is higher than the δ-In_2Se_3 phase transition temperature, with the other temperatures aligned with the β and α, respectively. By giving the crystal sufficient time to stabilize at each temperature, we expected to minimize thermal fluctuations, thus promoting a more stable and homogeneous synthesis of the desired In_2Se_3 polymorphs.

On the other hand, Figure 4.1.2b illustrates the crystal growth process of the second sample, which underwent a fast-cooling process, going from 900°C to room temperature within a few hours. By employing structural characterization techniques, we expected to observe differences in the concentration of phases and polymorphs obtained in both samples, as well as other structural distinctions such as grain sizes.

(a) **(b)**

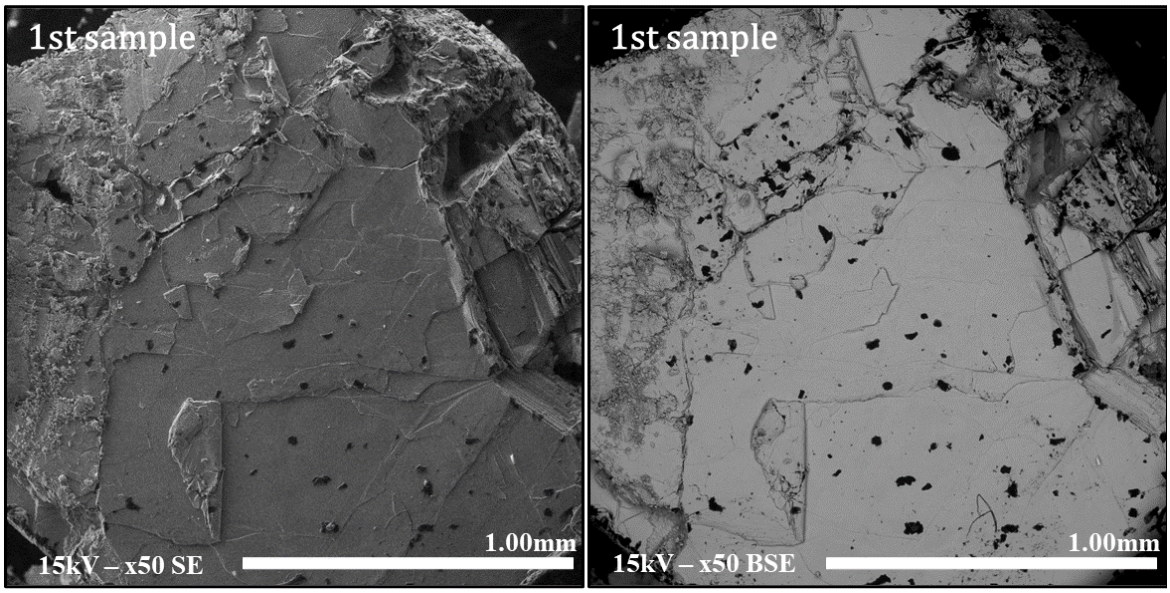

Figure 4.1.3. SEM images of first sample, taken at 15 kV with a magnification of 50x. **(a)** Captured using the SE detector and **(b)** BSE detector.

By analysing the first synthesized sample using scanning electron microscopy (SEM) with secondary and backscattered electrons (SE and BSE) detectors, it is evident that there are differences in the information obtained from the sample. In the SE image displayed in Figure 4.1.3a, it is possible to observe an apparent lamellar structure with more details and information compared to the BSE image shown in Figure 4.1.3b. Zooming in one of these structures, we obtain a more detailed image of the layers that compose the crystal, which can be seen in Figure 4.1.4. This approach provides direct evidence that we have successfully synthesized layered phases of indium selenide.

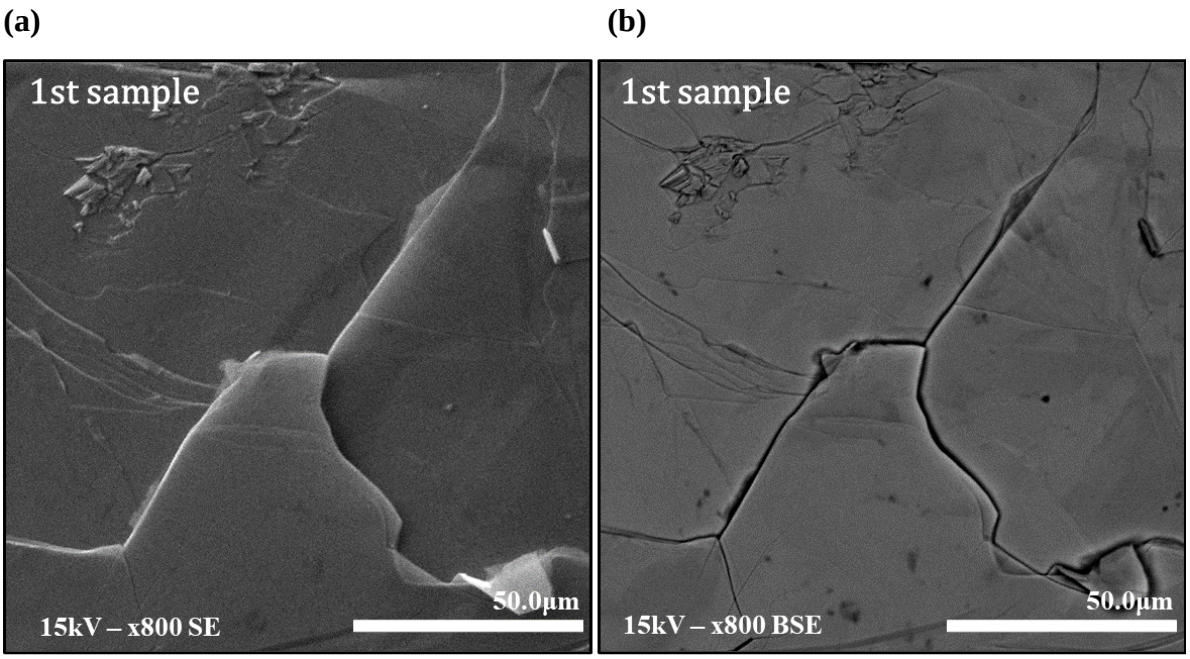

Figure 4.1.4. SEM images with magnification of 800x, displaying the lamellar structures using **(a)** SE and **(b)** BSE detectors.

Using the BSE detector, we collected several EDS spectra from the image above, as well as several other high-resolution magnified images. Upon calculating the averages of these spectra, we determined an atomic ratio of (39.0±1.5) % of indium and (61.0± 1.5) % of selenium. The average spectra are depicted in Figure 4.1.5.

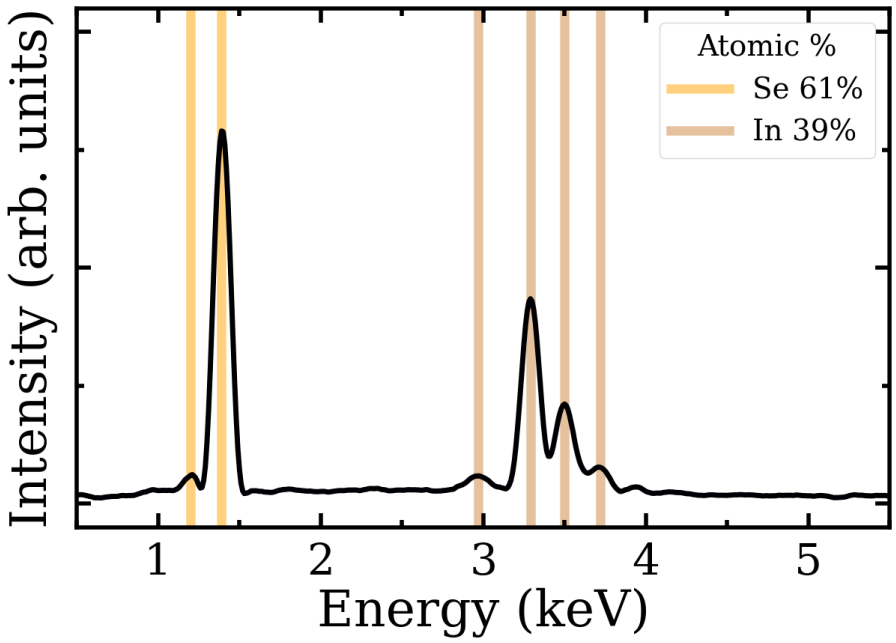

Figure 4.1.5. EDS spectrum of the first sample. The measured atomic proportion matches the intended value of the atomic ratio for the In_2Se_3 molecule.

Despite the mean atomic proportion values being in close agreement with the expected atomic ratio for the In_2Se_3 compound, this analysis alone is insufficient to confirm whether the sample is indeed In_2Se_3. For instance, a mixture of different phases might yield the same result. Moreover, since the EDS is a local measurement, it is possible that the acquired data is from a region of the sample predominantly composed of the In_2Se_3 phase.

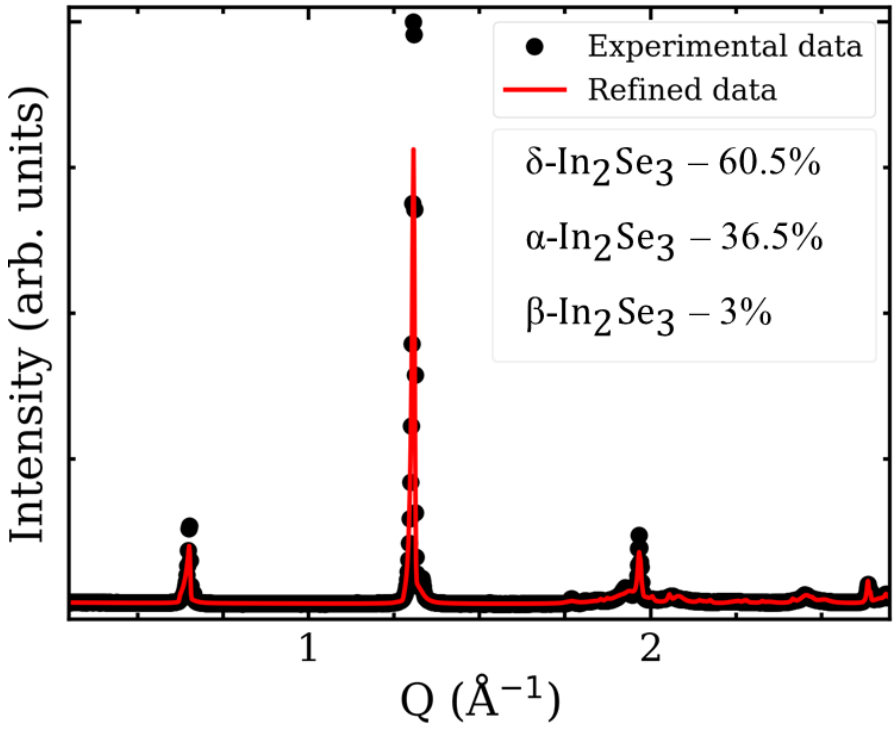

Figure 4.1.6. Powder X-ray diffraction pattern of the first sample. The dotted line represents the experimental data, while the red curve presents the data fit using Rietveld refinement.

To understand the phase and polymorph composition in the crystal, we employed a powder X-ray diffraction (XRD) analysis. The radiation used is Cu-Kα, with a wavelength of 1.54 Å. Figure 4.1.6 depicts the powder X-ray diffraction pattern of the first sample, as well as the Rietveld refined data curve shown in red. This refinement was obtained through collaborations that utilized the MAUD data analysis software. We determined the presence of α, β, and δ-In_2Se_3 polymorphs, with the corresponding weight percentages of 36.5%, 3%, and 60.5%, respectively. The disparity between these In_2Se_3 polymorphs is counterintuitive based on the phase diagram, as we subjected the crystal to different temperatures for an equal duration for each of the desired polymorphs. One possible explanation for this could be variations in the crystallization rates among these polymorphs, with the δ-In_2Se_3 having a faster crystallization.

We turn our attention now to the Electron Backscattered Diffraction (EBSD) analysis. By providing crystallographic information files (CIFs) of phases and polymorphs for In_2Se_3 and InSe, we were also able to determine the phase proportion within our sample. We obtained approximately 41% of the α and δ-In_2Se_3 and 15% of InSe polymorphs. Besides the In_2Se_3 polymorphs, we determined the presence of the γ and ε-InSe, as well as a new polymorph of InSe with a space group of C2/m. Figure 4.1.7 shows the phase map of this first sample measurement, with the normalized phase proportions.

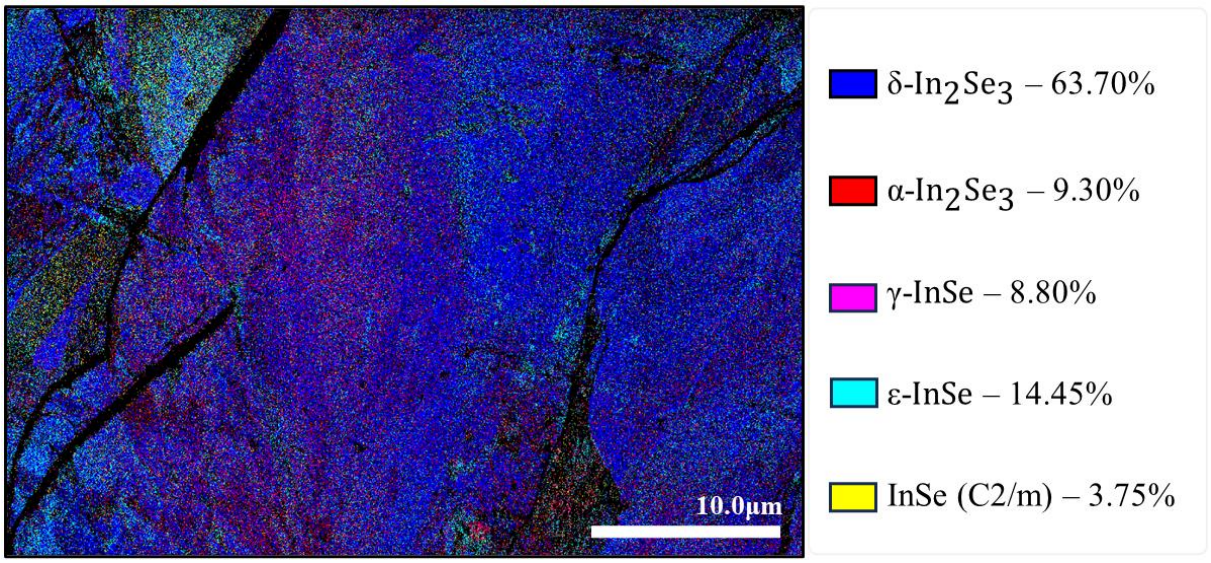

Figure 4.1.7. EBSD phase map of first sample. The phase proportions have been normalized.

Although new phases and polymorphs of indium selenide were found in the EBSD, it is important to note that the β-In_2Se_3 vanished in this analysis. Moreover, the black regions in the phase map indicate that it was not possible to correlate phases or polymorphs with the given CIFs. This could be attributed to the penetration of the electron beam, restricted to a few hundred nanometers in the crystal. Given the highly polycrystalline nature of the sample, variations in phases and polymorphs within the c-plane could undefine the Kikuchi lines, making it difficult to correlate the provided data with the diffraction lines.

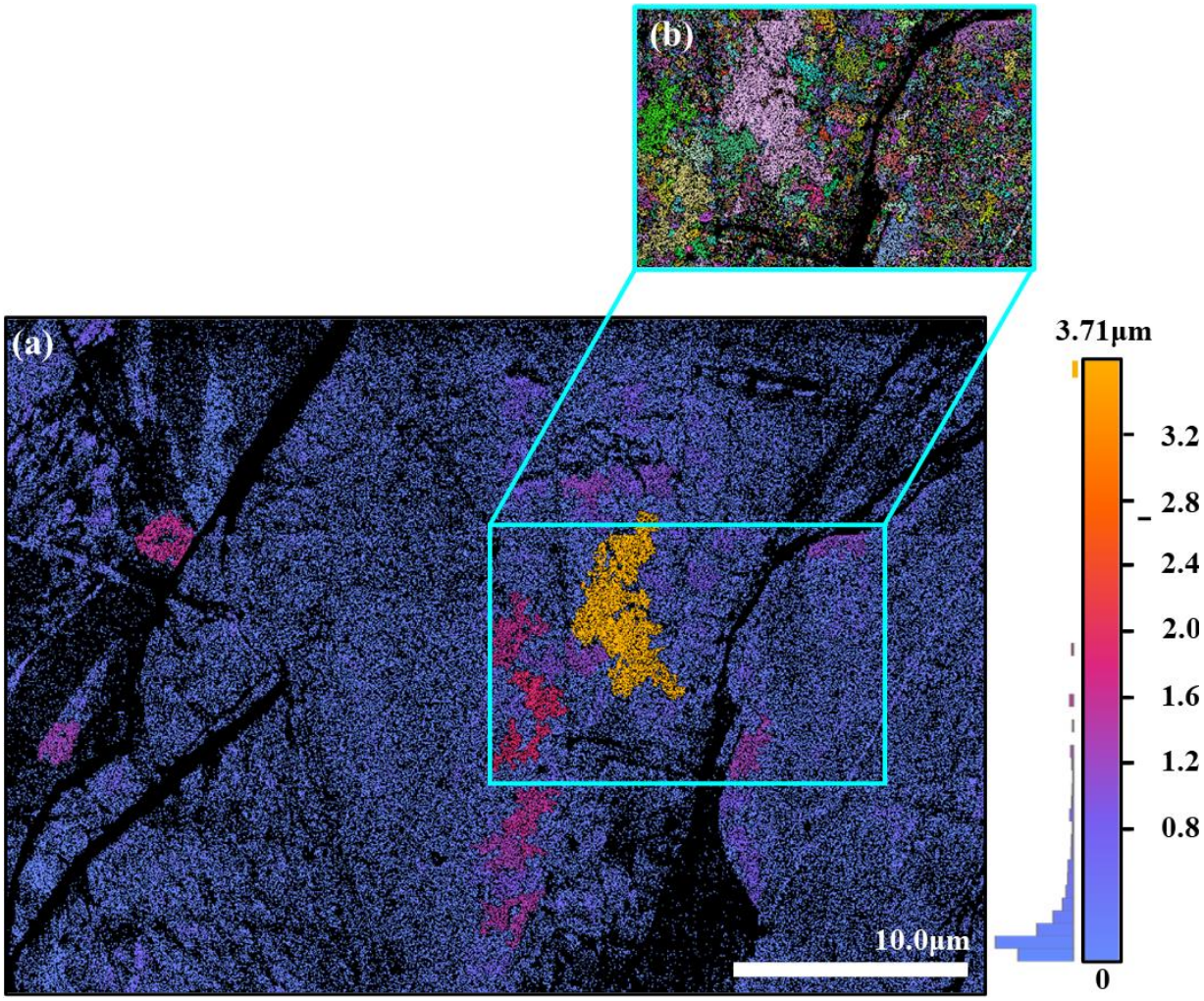

Figure 4.1.8. (a) Grain size map of the first indium selenide sample. The grain sizes are predominantly distributed between 0.05 and 0.4 microns. **(b)** Grain boundary map of the selected are in figure a.

In Figure 4.1.8a, we present the grain size map of the first indium selenide sample. The majority of the examined area is composed of grains ranging from 0.05 to 4 microns in size, while the biggest grain in this measure has approximately 3.7 microns. This structural property might be explained by the crystallization rate of the phases and polymorphs within the sample. For instance, if the growth rate of the predominant δ-In_2Se_3 is fast enough, the grains will not have time to significantly grow in size, resulting in smaller grains. On the other hand, as a significant number of other phases and polymorphs crystallize from across the entire sample, regions that are forming grains of different stoichiometries prevent the growth of grains of the predominant phase. Because of these reasons, only a few numbers of grains can grow larger than a fraction of microns.

For the second indium selenide sample, the SEM images further indicate the successful synthesis of layered phases, evidenced by the observed lamellar structures. Figure 4.1.9 shows the crystal with x30 and x1500 magnification using both SE and BSE detectors.

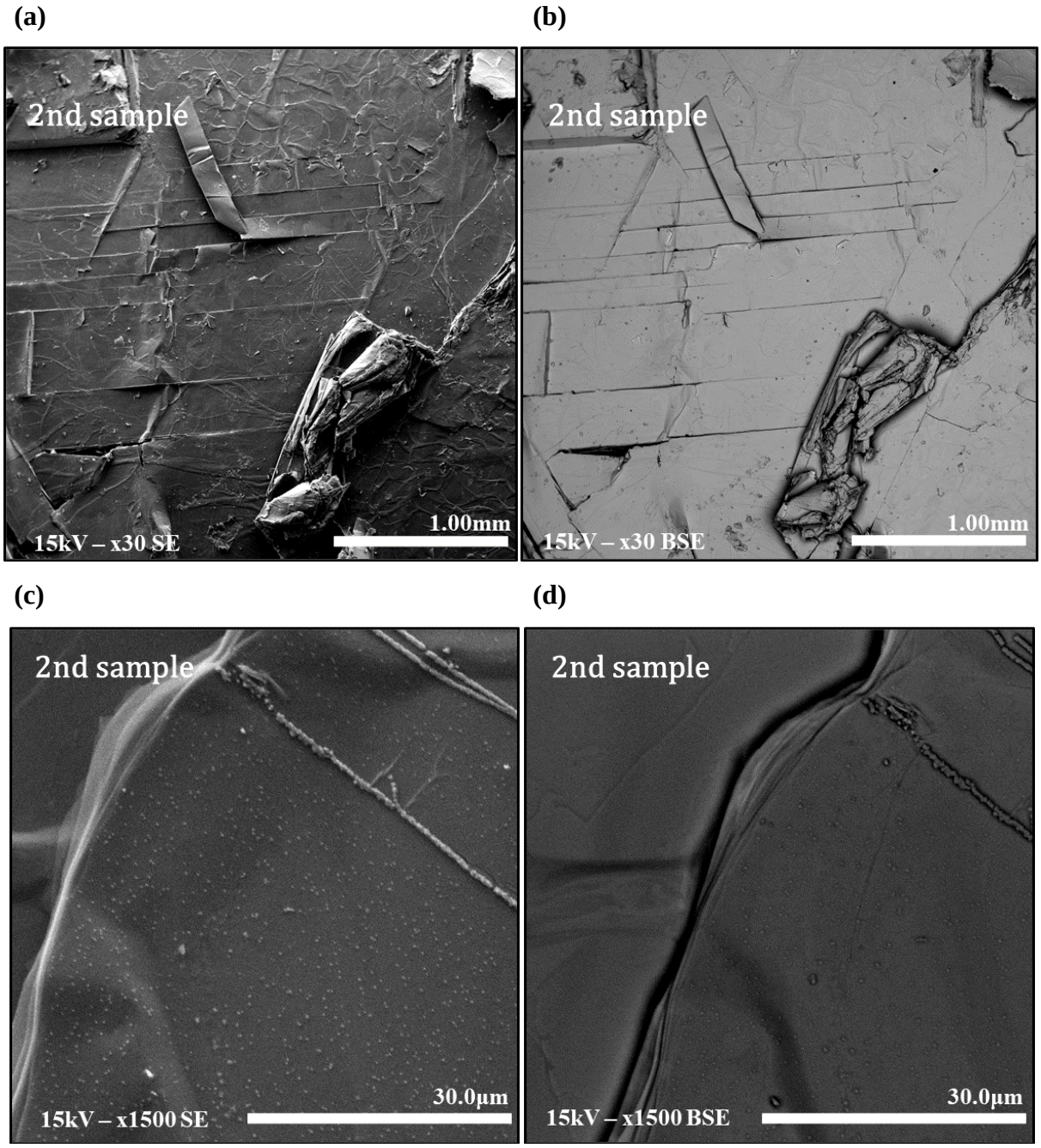

Figure 4.1.9. SEM image with **(a)** x30 using SE detector; **(b)** x30 using BSE detector. **(c)** x1500 using SE detector and **(d)** x1500 SEM image using BSE detector.

Using these high-resolution images, we conducted EDS measurements at various points within the sample. The average atomic proportion of these spectra is (38.0±1.0) % of indium

and (62.0±1.0) % of selenium, matching the expected value for the In_2Se_3 compound. However, as we could see, this analysis proved to be limited, especially considering the identification of the InSe phase within the first sample.

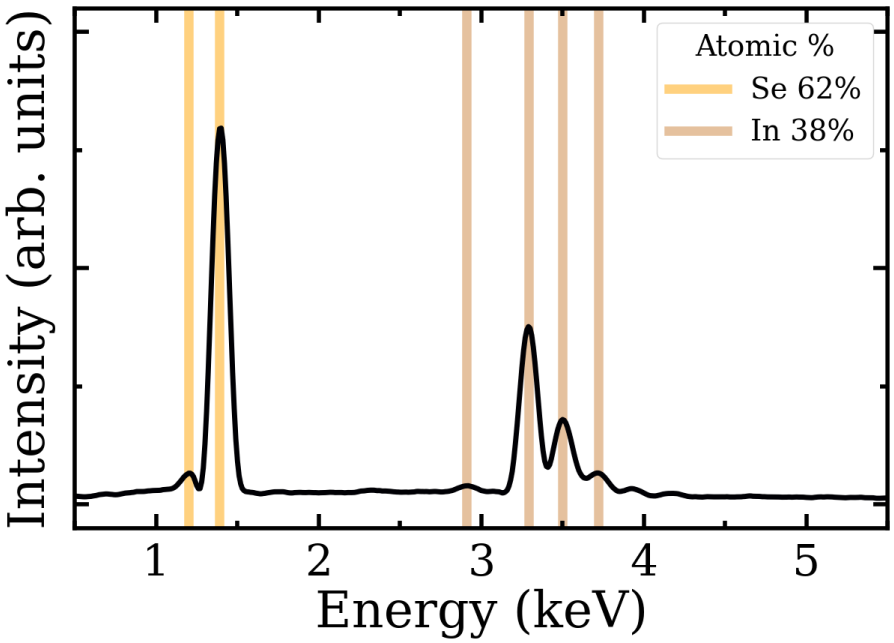

Figure 4.1.10. EDS spectrum of the second sample. The atomic proportion matches the expected value of the atomic ratio for the In_2Se_3 compound.

To examine the phases and polymorphs composition of the second crystal, we conducted powder X-ray diffraction. Figure 4.1.11 depicts the diffraction pattern of the second sample, presenting a higher number of peaks compared to the first one, especially at high values of Q.

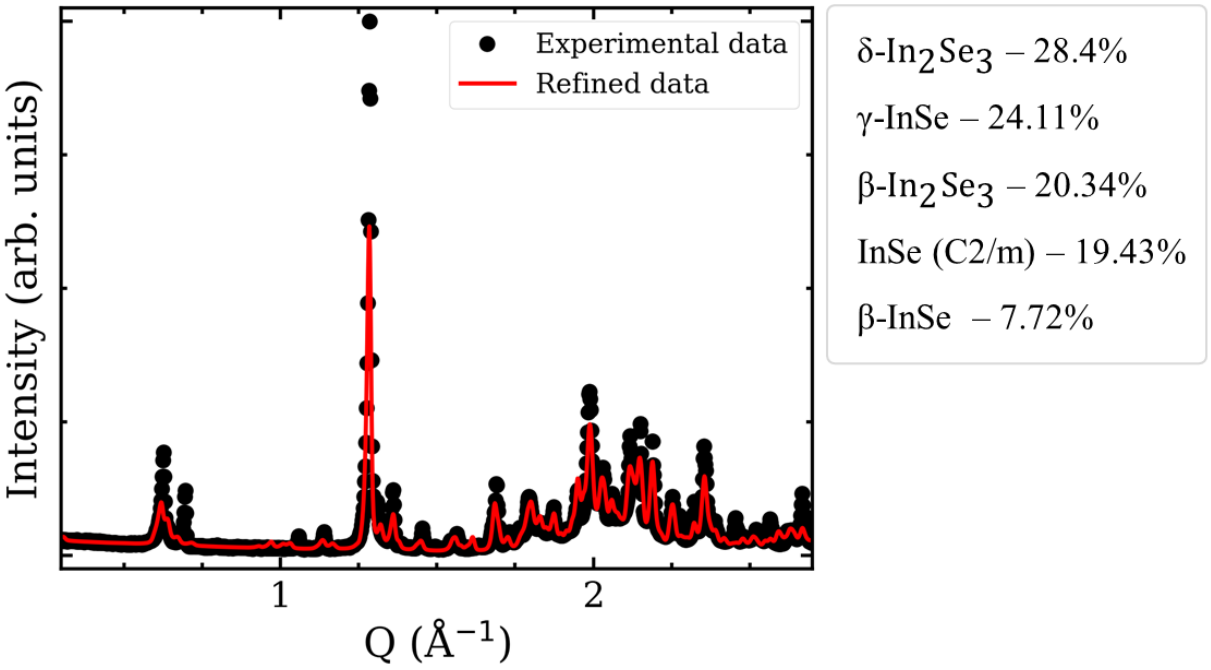

Figure 4.1.1.11. Powder X-ray diffraction of the second sample.

For the In_2Se_3 phase, the Rietveld refinement revealed the presence of two primary polymorphs: δ-In2Se3 and β-In_2Se_3. In the case of InSe, the analysis identified γ-InSe and InSe (C2/m), along with a polymorph not detected in the initial sample, β-InSe.

Comparing the two diffractograms shown in Figures 4.1.6 and 4.1.11, it becomes evident that the two growth approaches yielded entirely distinct diffraction patterns, despite the presence of some familiar peaks between them. While they do share common phases and polymorphs, the second sample still presents a significant number of peaks that were not observed in the first sample. Figure 4.1.12 depicts the comparison of both diffraction patterns while indexing the (00L) peaks family of δ-In_2Se_3. The δ polymorph is the predominant form of In_2Se_3 in both crystals, as indicated by both qualitative analyses of the peaks and quantitative data obtained by the Rietveld refinement.

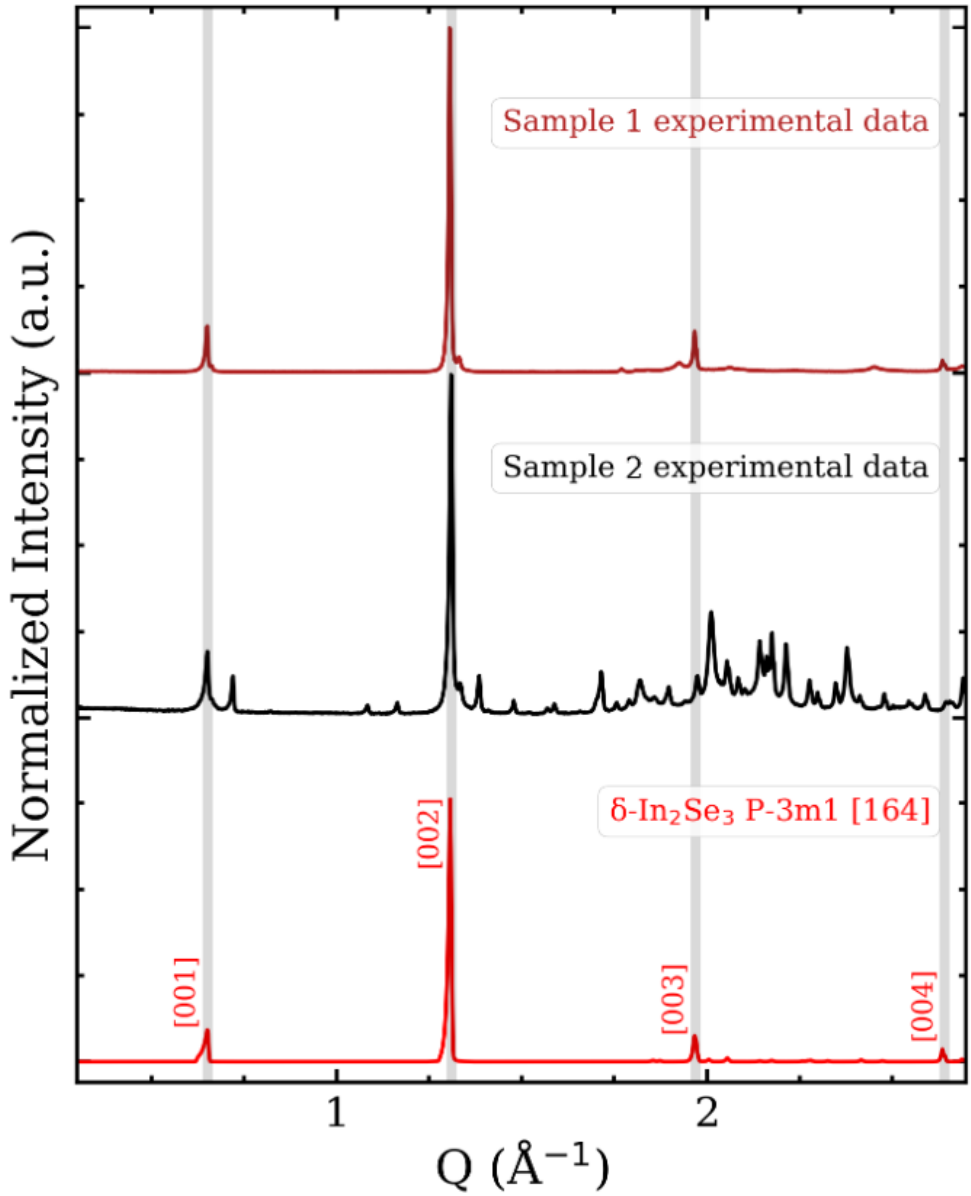

Figure 4.1.12. Comparison between the two diffraction patterns of both samples. The (00L) peaks of δ-In_2Se_3 are among the most intense peaks of both samples, indicating that this phase constitutes the major portion of these crystals.

Despite finding other phases using EBSD, we recall that the diffraction pattern of the first sample is simpler. We have only obtained the only three In_2Se_3 polymorphs, with two of these structures accounting for over 95% of the entire crystal. Despite the additional phases identified, causing a reasonable decrease in the δ-In_2Se_3 proportion, the difference between the δ polymorph and the second most predominant phase still exceeded 27%. This demonstrates that the additional structures obtained via EBSD represent a small fraction of the sample volume.

The uncontrolled cooling of the second sample has led to a more uniformly distributed phase proportion, with four of them around 20%. Consequently, with a more balanced distribution of these percentages, the intensity of diffraction peaks of a given phase increases. As such, we attribute the significant number of peaks to the predominance of at least four phases in the same crystal. As we shall observe, the EBSD measurement also revealed the existence of additional minor phases and polymorphs, contributing to further complexity in the diffraction pattern. The additional phases found were taken into consideration in the XRD analysis but were discarded during the refinement process.

The EBSD measurements of the second sample, however, diverge from the X-ray diffraction analysis. While the Rietveld refinement identified the δ-In_2Se_3 as one of the predominant phases, it appeared with a significantly diminished proportion in the EBSD results. Conversely, the β-In_2Se_3, which is one of the three major phases in terms of percentage abundance, emerged as the most prominent in the EBSD measurement. Figure 4.1.13 displays the EBSD phase map of the second sample.

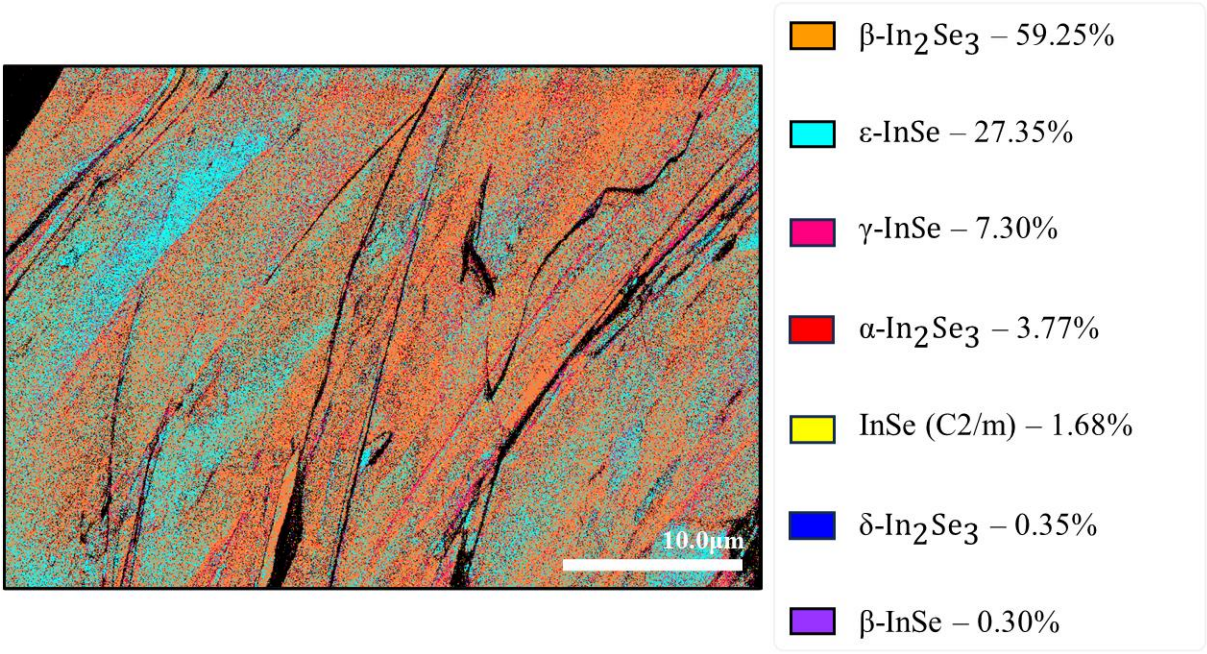

Figure 4.1.13. EBSD phase map of the second sample. Approximately 0.29% of the structure is attributed to 3D phases of In_2Se_3, thus desconsidered in the analysis.

The β-In_2Se_3 and the ε-InSe are the predominant structures in the investigated area, accounting for approximately 75%. In this sample, we managed to obtain a significantly lower

'zero solutions' value compared to the previous measurements, approximately 13%. Moreover, we acquired a value of 0.29% for two 3D phases of In_2Se_3, which will be disregarded in the analysis.

The disparity in results can be attributed to the difference between a local crystallographic measurement provided by EBSD with a bulk analysis of powder XRD. The EBSD measurement is conducted within a region of a few microns in size. Consequently, it is possible to obtain images in a specific area that may exhibit a dominance of one phase over another. One approach to mitigate this concern would involve performing a series of scans over a larger crystal area, thereby achieving a more robust statistical representation.

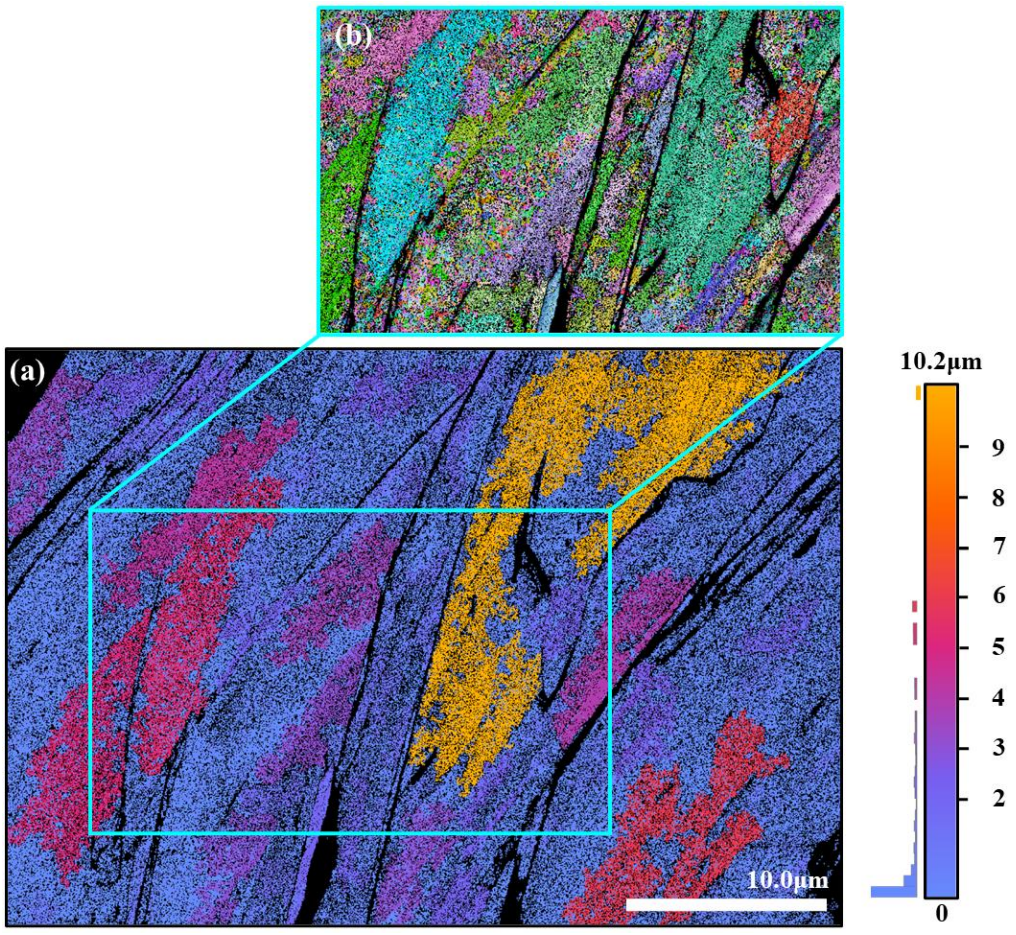

Figure 4.1.1.14. (a) Grain size map of the second sample. **(b)** Grain boundary map of the selected blue area.

From the grain size map of the second phase, a substantial difference compared to the first sample becomes evident. Here, we can observe that the structure comprises larger grains, reaching sizes of approximately 10 microns. While there is still a significant number of grains

in fractions of microns, a higher prevalence of grains with values exceeding 2 microns is noticeable, occupying a significant area of the image.

As the predominant phase in the two measurements differs, the hypothesis that δ-In_2Se_3 undergoes fast crystallization, lacking sufficient time for the formation of larger grains, becomes even more plausible. The β-In_2Se_3, which had the lowest proportion in the first sample, despite being subjected to the same crystallization temperature and duration as the other samples, yielded only a small percentage. This could suggest a slower growth rate, allowing the grains obtained in the above measurement to have had enough time to grow slightly larger, further confirmed by the EBSD grain size map of the second sample.

4.2 Measurements of Local Electronic Density of States

4.2.1 Scanning Tunneling Microscopy

The scanning tunneling microscopy technique yielded a number of nanometer-scale images for both samples, facilitating the observation of lamellar structures previously observed via scanning electron microscopy. Figures 4.2.1 and 4.2.2 present three STM images for each sample, providing a clear visualization of the layered structure of these materials.

The morphological features of these STM images of both samples are slightly different. While the first sample images exhibit more linear steps between individual layers, the second one has mound and more rounded structures. This result should be understood taking into account the different temperature regimes with which the samples were grown. The first sample was annealed at a different temperature, which may provide more favourable conditions for crystallization to occur uniformly across the crystal surface. Moreover, the growth temperature changes could influence the dominance of certain growth facets, leading to variations in step shapes. For the second sample the quenched from 900°C might disrupt the linear layer-by-layer growth, leading to the formation of the mound and rounded steps observed.

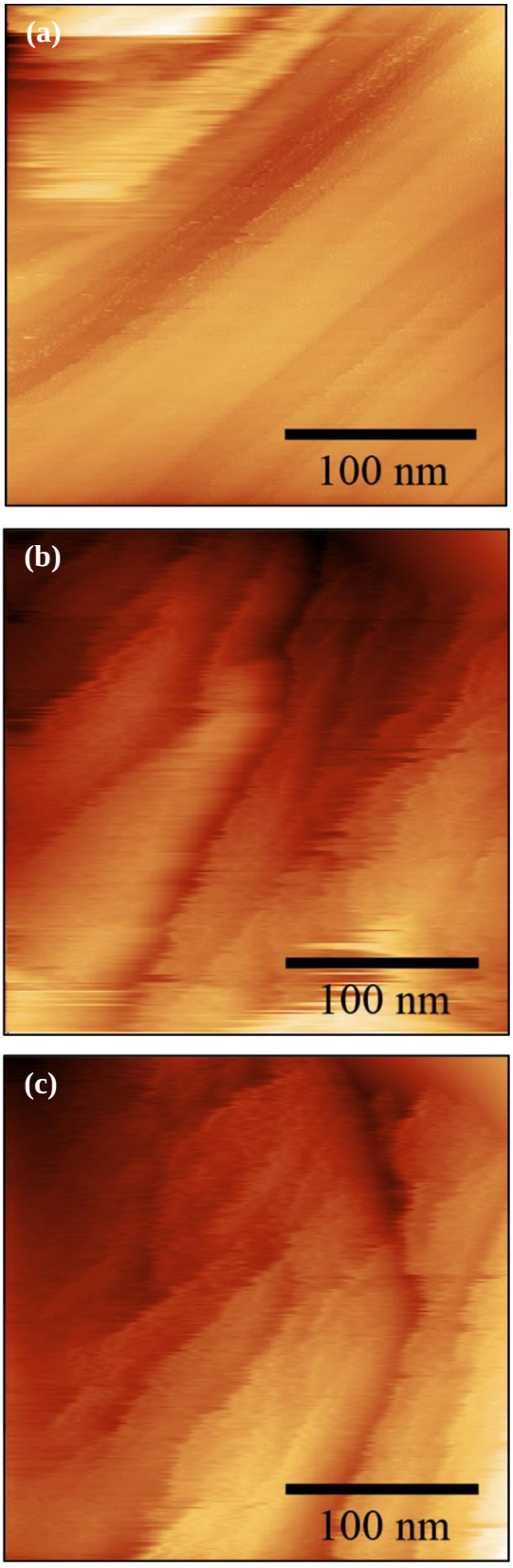

Figure 4.2.1. STM images of 250 nm taken in three different regions **(a)**, **(b)** and **(c)** of the first sample. Setpoint of 800 pA and tip voltage of 800 mV.

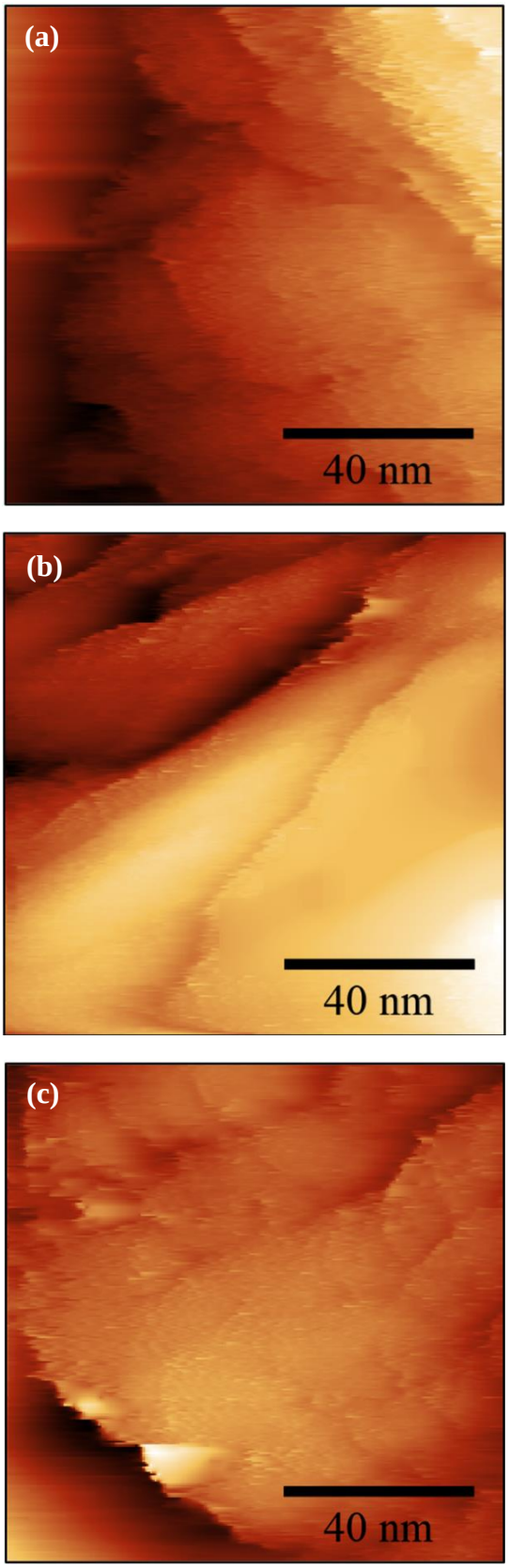

Figure 4.2.2. STM images of the second sample at a scale of 100nm. **(a)** Setpoint of 1 nA and a tip voltage of 1V. **(b)** Setpoint of 501 pA and a tip voltage of 900 mV. (c) Setpoint of 501 pA and a tip voltage of 900 mV.

4.2.2 Scanning Tunneling Spectroscopy

From STM images like those shown in the above figures, it is possible to obtain tunneling spectra (STS) from specific points, sets of points, or areas. In our work, due to the apparently prevalent grain sizes in the nanometer scale as observed via EBDS, it was prudent to prioritize point-spectroscopy measurements. This choice guarantees minimal acquisition area, consequently reducing the probability of obtaining a mean spectrum of different phases and polymorphs.

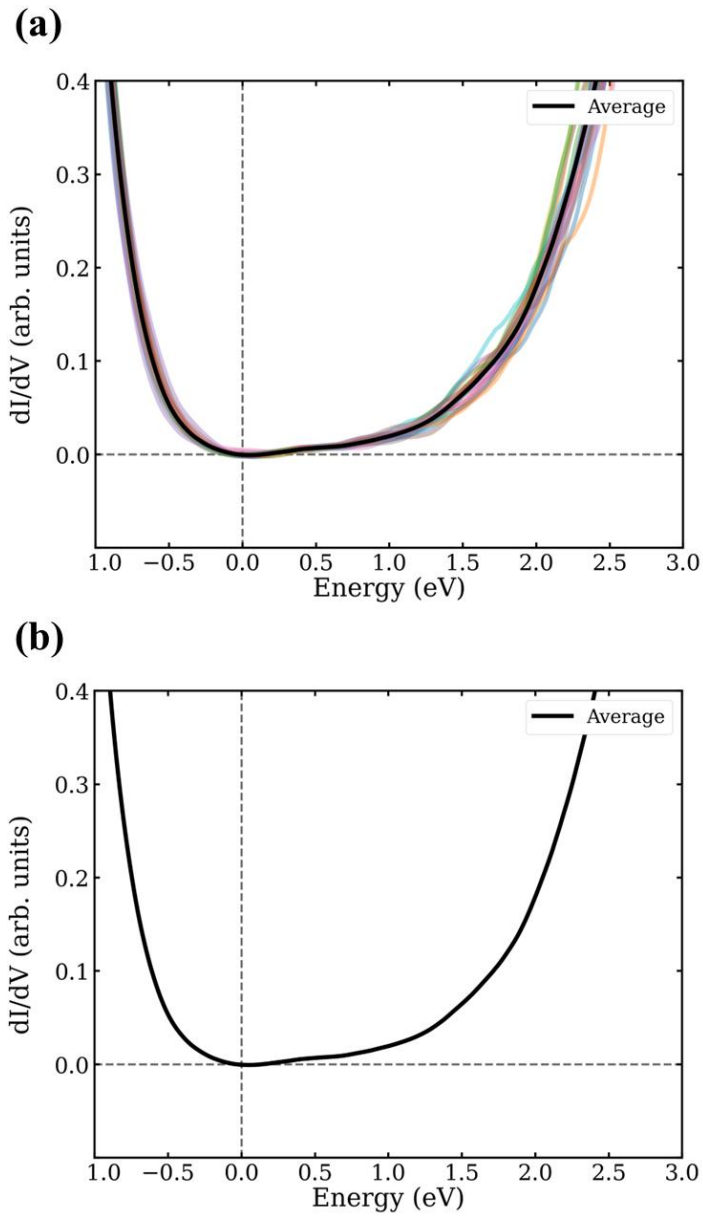

Figure 4.2.3. (a) Typical STS curves. The coloured opaque curves showcase the diverse spectra acquired from an image, with the black line denoting the average of these curves. **(b)** Plot of the mean of the curves obtained.

Additionally, we have employed a statistical approach to the STS measurements. This involved calculating the average of these curves when obtaining a set of similar spectra. Figure 4.2.3a presents STS curves acquired through point-spectroscopy along with the corresponding average curve illustrated as a black line. From this point onward, we will primarily display the average of the curves, as depicted in Figure 4.2.3b.

The average curves obtained in this work will be compared to density functional theory (DFT) calculations of the electronic density of states (DOS). Most of the calculations were performed by collaborations unless otherwise indicated in the text.

4.2.2.1 α-In_2Se_3

We have successfully determined a region of the sample with a tunneling spectrum profile similar to the computational profile of the α-In_2Se_3. Figure 4.2.4 illustrates the electronic band structure of α-In_2Se_3, displaying a gap of 1.27 eV.

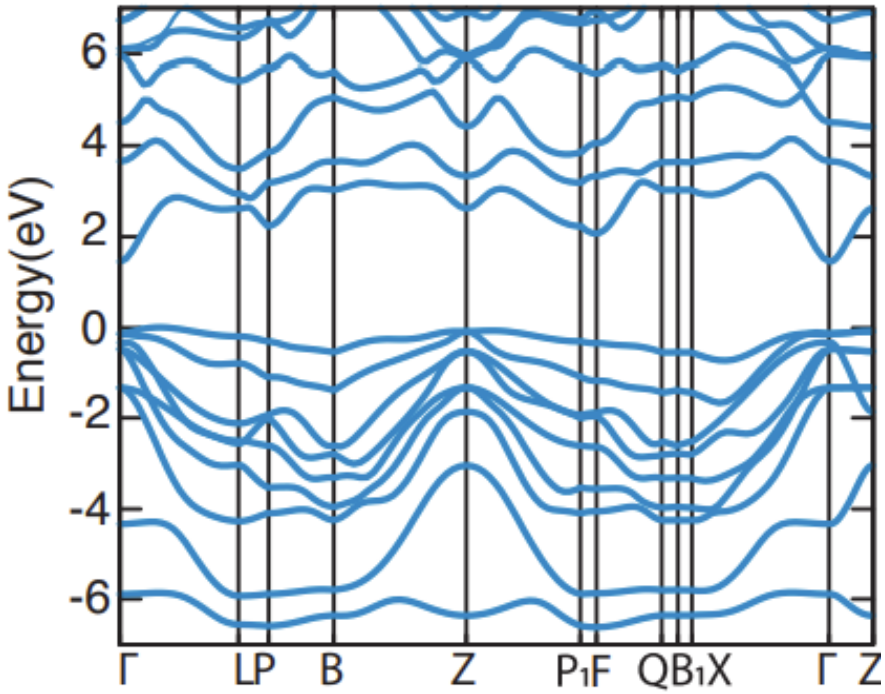

Figure 4.2.4. Electronic band structure calculations of the α-In_2Se_3. The fundamental band gap is approximately 1.27 eV. Figure taken from reference [22].

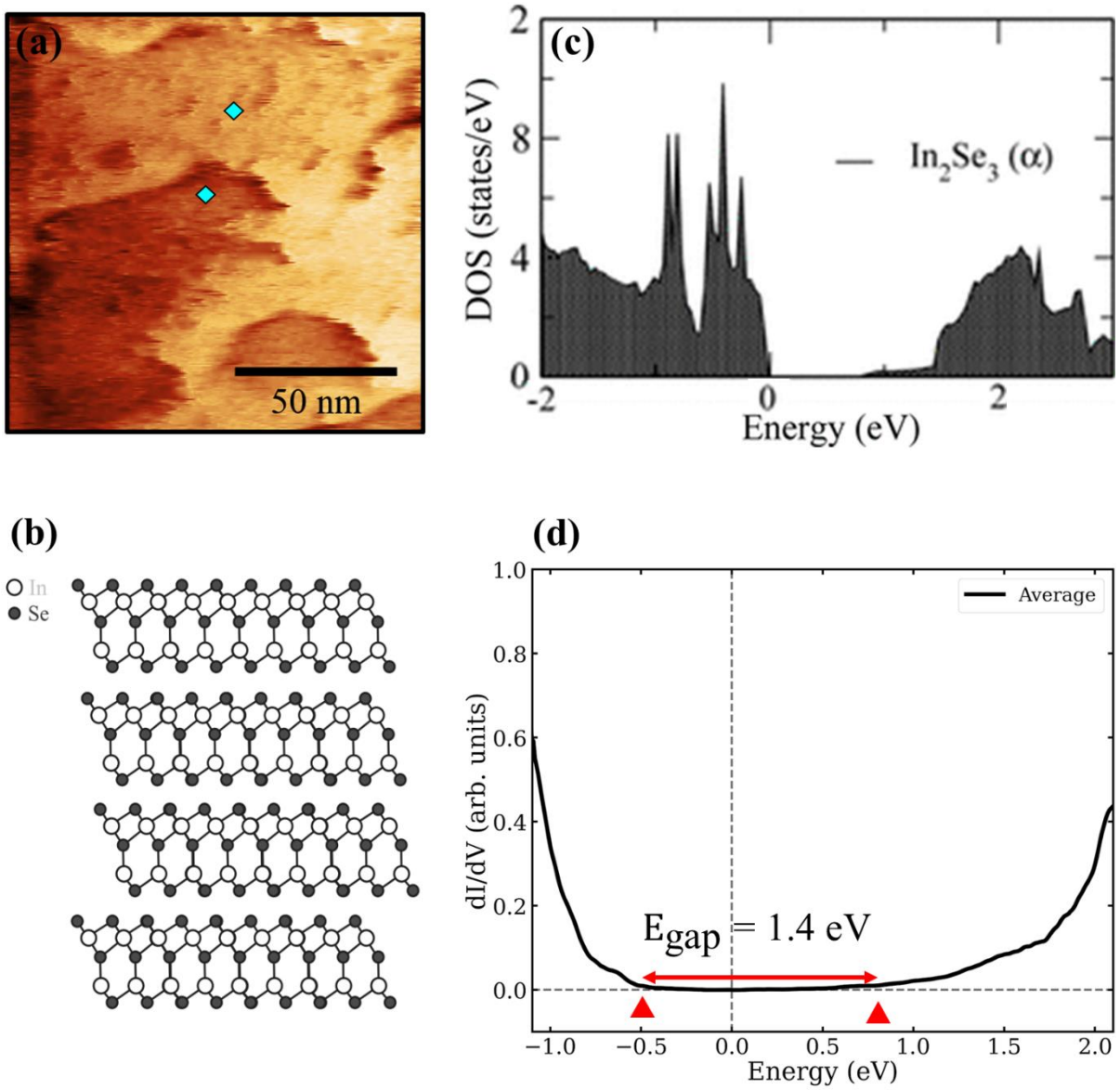

Figure 4.2.5. (a) STM image, with the points highlighted in blue indicating where the tunneling spectra were acquired. **(b)** Schematic view of the stacking of quintuple layers of the α-In_2Se_3 phase. **(c)** Total electronic density of states is calculated in reference [48]. **(d)** Average of at least ten STS curves obtained in figure a. The same result was observed in several different regions of the surface.

The tunneling spectra were obtained at the blue points visible in the STM image shown in Figure 4.2.5a. The atomic arrangement of the quintuple layers of the α-In_2Se_3 phase is displayed in Figure 4.3.5b.

Comparing the tunneling spectrum (see Figure 4.2.5d) with the computational calculation of the electronic density of states for the α-In2Se3 phase (see Figure 4.2.5c), it is

possible to observe a correlation between the profiles of both curves. Starting from negative energies, meaning the valence band, the derivative of the tunneling current exhibits a rapid decrease up to -0.5 eV. From -0.5 eV up to 0.9 eV, the dI/dV is nearly constant and equal to zero. This is a signature of a band gap typical of a semiconductor. For positive energies, a gradual increase in the dI/dV shows the onset of the appearance of the conduction band. Eventually, this growth intensifies, indicating that within the energy range of approximately 1.7 to 2 eV, a substantial number of available states exist for tunneling electrons. Finally, we estimated the energy gap value of the material using the tunneling spectrum. The value we obtained is approximately 1.4 eV and it is close to the results reported results published in the literature, typically ranging from 1.27 to 1.4 eV [22, 40-42]. Although qualitative, the dI/dV versus energy graphs shown here and onwards reproduce the calculated electronic densities of states.

4.2.2.2 β-In_2Se_3

The β-In_2Se_3 polymorph was also identified through scanning tunneling microscopy and spectroscopy. In the literature, the band gap reported ranges from 0.46 eV to 0.7 eV. Figure 4.2.6 depicts the electronic band structure calculations for this semiconductor material.

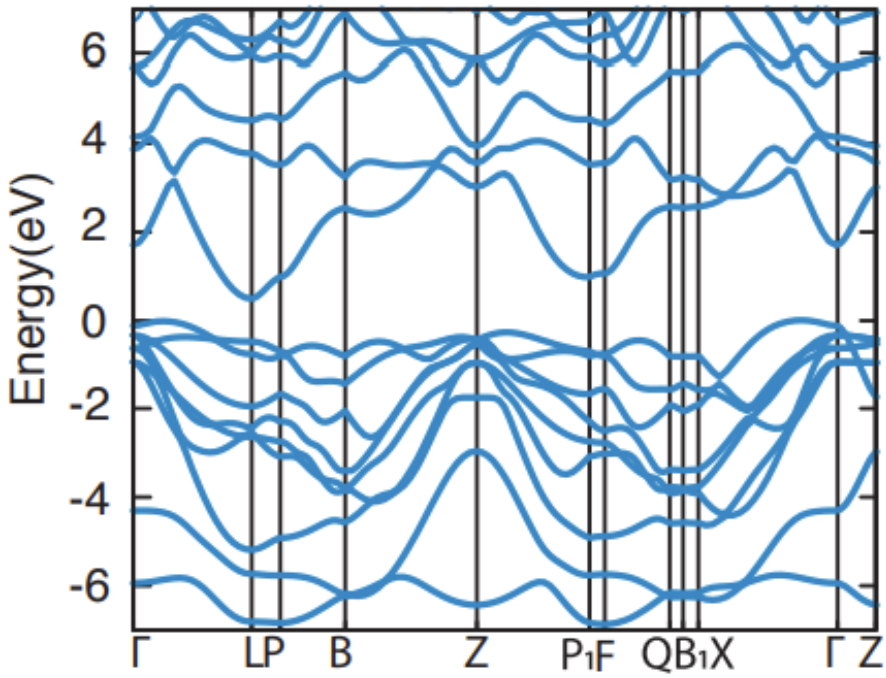

Figure 4.2.6. Electronic band structure of β-In_2Se_3. The figure was taken from reference [22], with a reported band gap value of 0.46 eV.

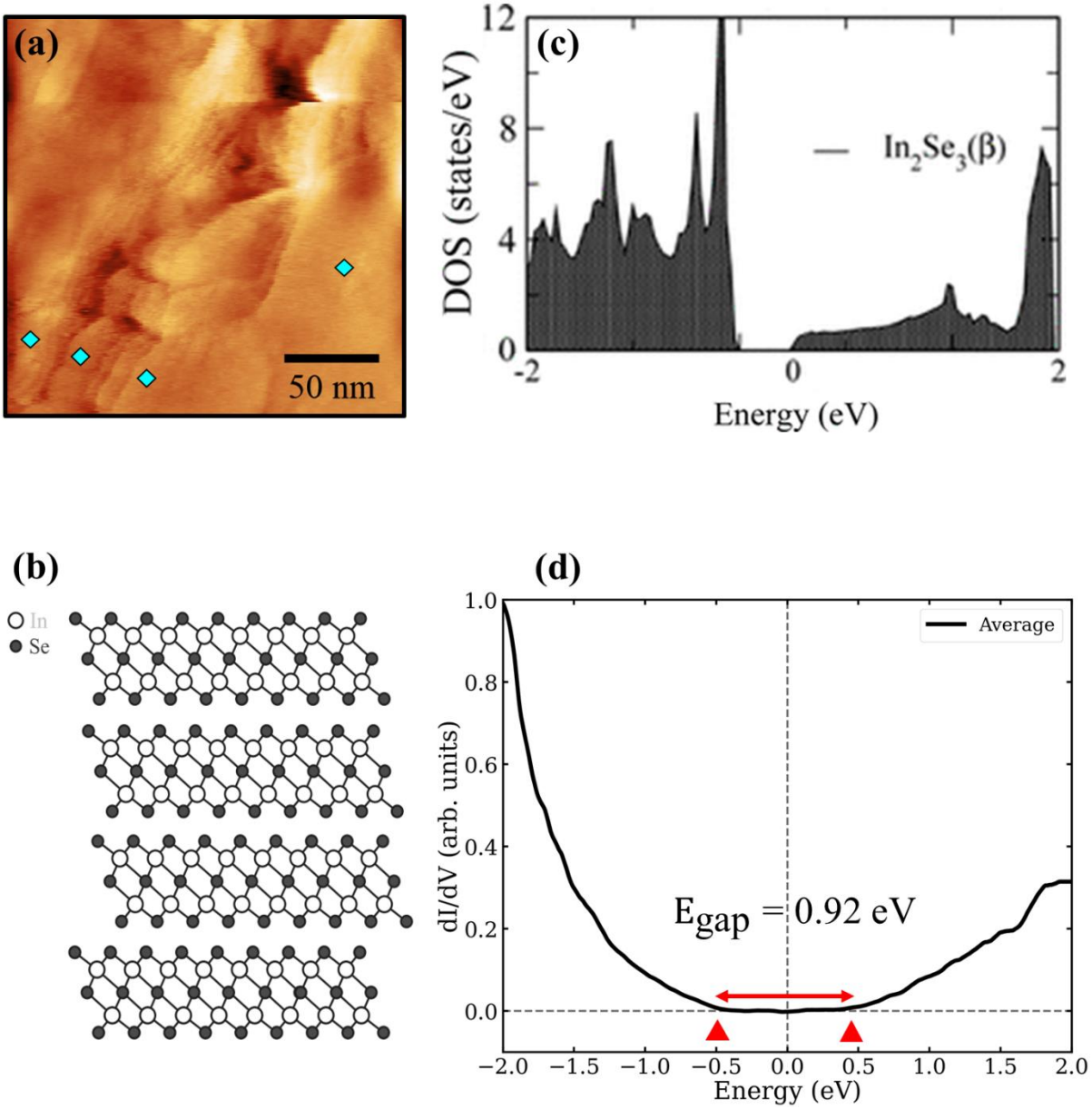

Figure 4.2.7. (a) STM image featuring four points where spectroscopy was conducted. **(b)** Arrangement of quintuple layers of the β-In_2Se_3 phase. **(c)** Total electronic density of states is calculated in reference [48]. **(d)** Average of the tunneling spectra measured in the region is depicted in figure a.

For negative energies, both curves exhibit a rapid decrease, reaching its lowest value at approximately -0.5 eV. The dI/dV value is equal to zero from -0.5 eV up to 0.45 eV. In contrast to the α polymorph, the experimental curve of dI/dV β-In_2Se_3 displays a more prominent bump at the beginning of the conduction band. As the positive energy increases, the density of states remains approximately constant. Analysing the band gap obtained from the tunneling spectrum, we obtain an approximate value of 0.92 eV. The profiles of both the tunneling spectrum and

the computational calculations are similar. As the DFT often underestimates the band gap, 0.9 eV is a reasonable value.

4.2.2.3 δ-In_2Se_3

We have also been able to identify the most predominant phase in both synthesized crystals, δ-In_2Se_3. Among all the studied In_2Se_3 polymorphs, this material possesses the smallest band gap of 0.32 eV. Figure 4.2.8 depicts the electronic band structure calculations for this semiconductor material.

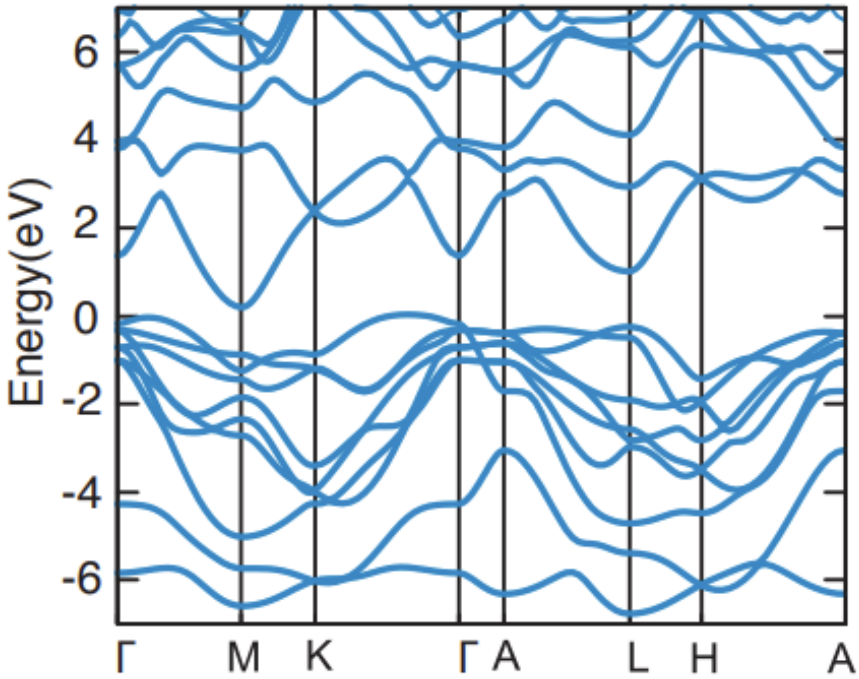

Figure 4.2.8. The electronic band structure of δ-In_2Se_3. This figure was taken from reference [22], with a reported band gap value of 0.32 eV.

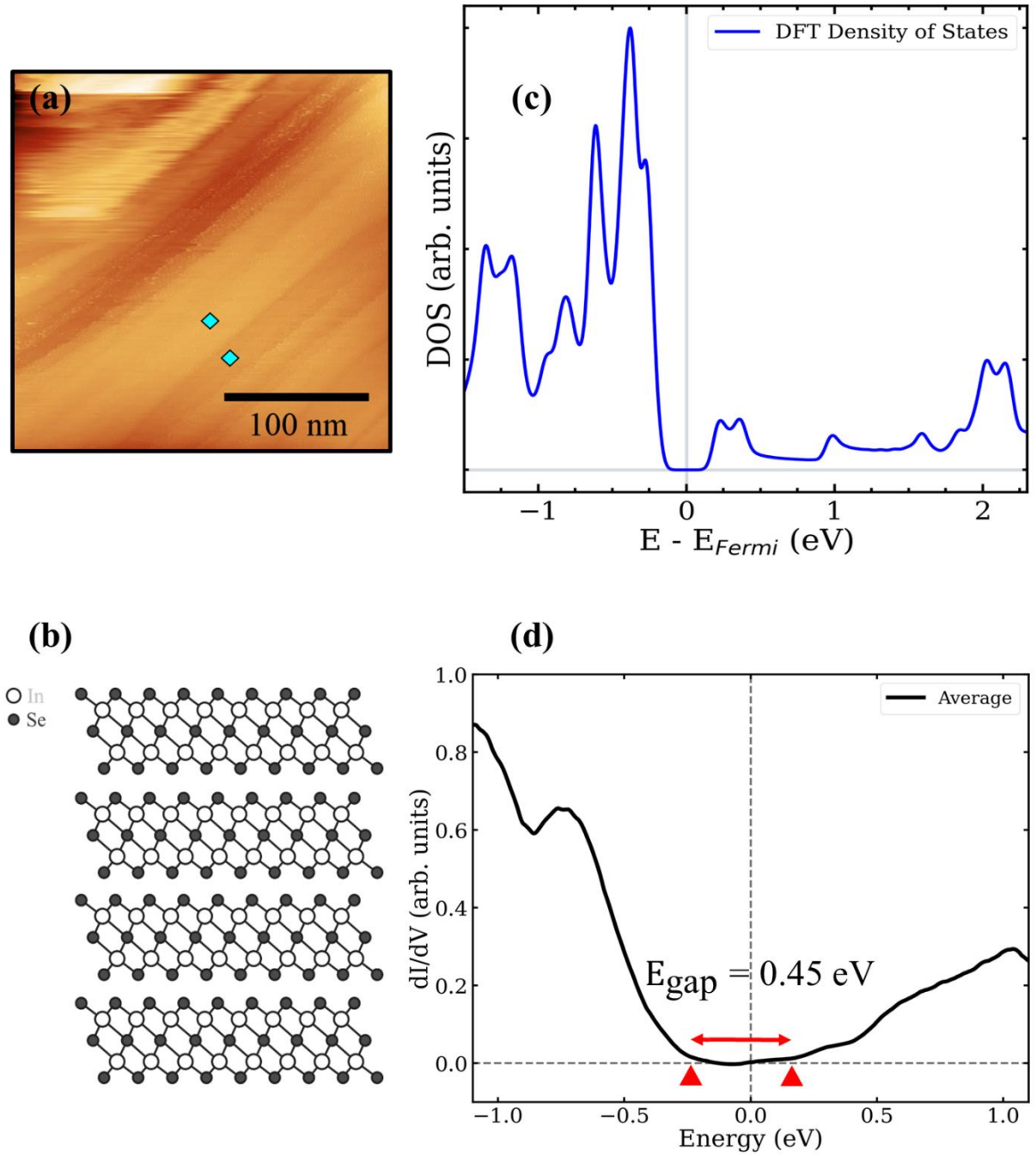

Figure 4.2.9. (a) STM image with the points where the STS spectra were obtained. **(b)** The stacking sequence of the quintuple layers of δ-In_2Se_3 **(c)** Electronic density of states calculations for the δ-In_2Se_3. **(d)** The obtained average of STS curves. The band gap obtained is approximately 0.45 eV.

The tunneling spectrum shown in Figure 4.2.9d exhibits a profile similar to the calculated electronic density of states shown in Figure 4.2.9c. In the negative energy regions, there is an accelerated curve decrease and a shoulder in the curve, which is observed both

theoretically and experimentally. The conduction band represents a region with fewer available electronic states, and both curves are also characterized by a bump. The estimated band gap value obtained from the tunneling spectrum is 0.45 eV, similar to the theoretical value.

4.2.2.4. InSe (C2/m)

We have also been able to identify two InSe phase polymorphs, namely the C2/m and ε-InSe ones. The C2/m polymorph is characterized by a tetra-layers arrangement (rather than a quintuple one), with two indium layers encapsulated by two selenium layers all connected by covalent bonds. These tetra-layers are also connected by van der Waals interaction, much alike the quintuple layer arrangements of the In_2Se_3 polymorphs. It possesses a large electronic gap, of nearly 2 eV. Figure 4.2.12 exhibit the complete electronic structure of the C2/m polymorph, where there is an indirect gap from the Y_2 to the A point in the reciprocal space, both close to the Γ point.

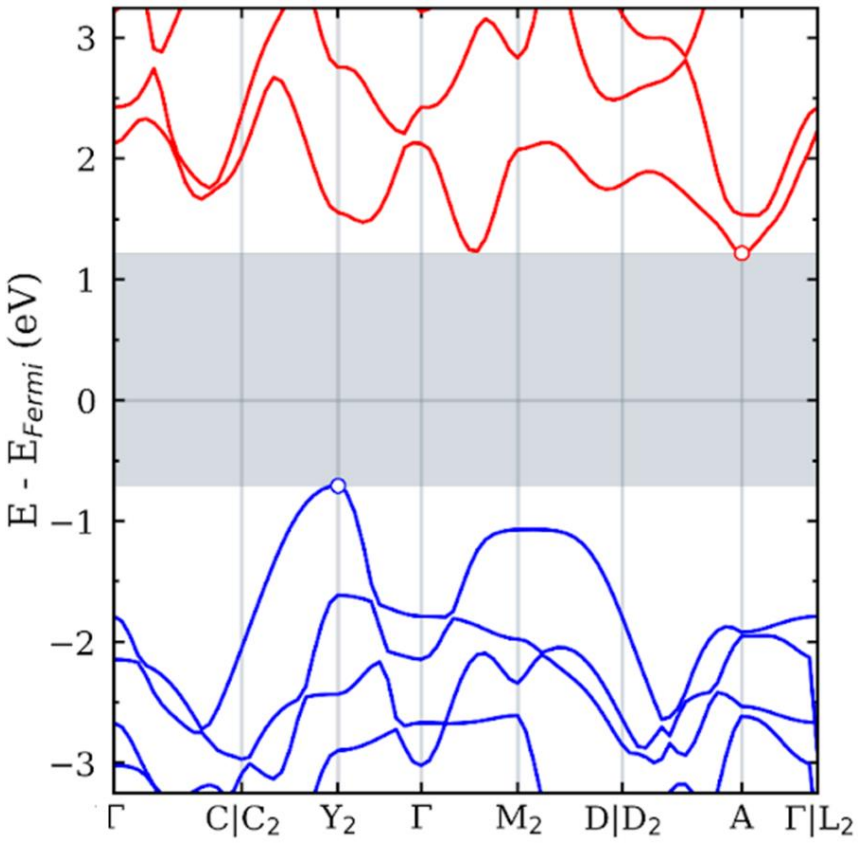

Figure 4.2.10. The electronic band structure of InSe (C2/m). The band gap value is 1.92 eV.

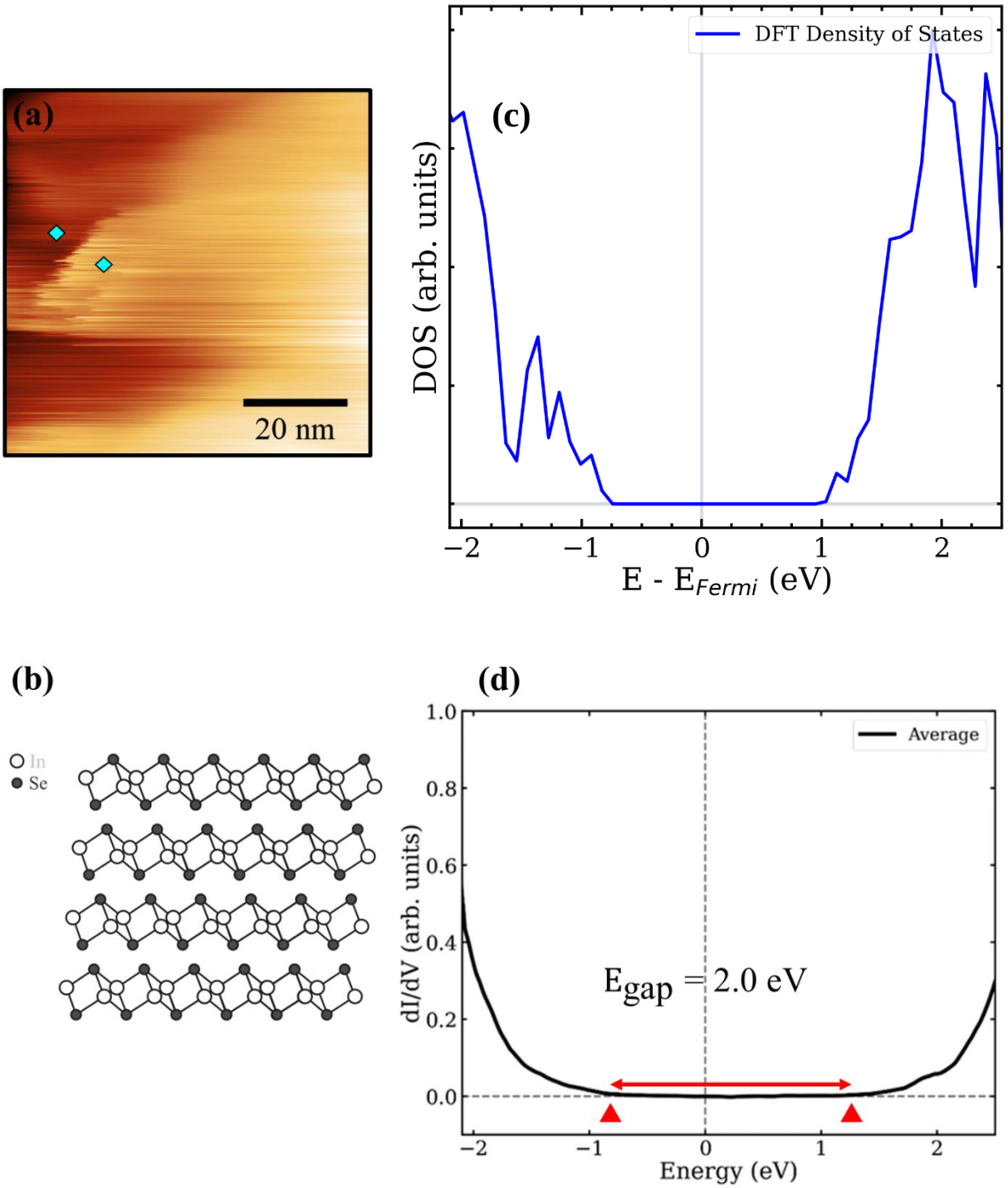

Figure 4.2.11. (a) STM image with the blue points representing the positions where the tunneling spectra were obtained. **(b)** Stacking sequence of the tetra layers of the InSe (C2/m) phase. **(c)** Electronic density of states calculations, with a band gap of 1.92 eV. **(d)** Average of the tunneling spectra. The band gap is 2.0 eV.

The tunneling spectrum shown in Figure 4.2.11d exhibits a band gap of approximately 2.0 eV. In contrast, the calculated band gap value is 1.92 eV, which is slightly smaller than the experimental result. The calculations of this InSe polymorph were conducted by our theoretical collaborators and, as it is well known, the DFT calculations may result in underestimated values of band gaps. Thus, the experimental band gap obtained is close to the expected value.

By analysing the tunneling spectrum profile, it is possible to observe that both experimental and computational curves are similar. Coming from the negative energy values, the dI/dV curve rapidly decreases, reaching a zero dI/dV value at approximately -0.8 eV. This null value of dI/dV is maintained until reaching the positive energy value at approximately 1.2 eV. Also, it is possible to observe a broad peak in the tunneling spectrum, around 1.8 eV. From 2.0 eV onwards, there is an increase in the electronic density of states of the conduction band, also observed in the calculated DOS.

4.2.2.5 ε-InSe

Finally, we turn our attention to the ε-InSe structure. Figure 4.2.10 presents the electronic band structure of this phase, highlighting a fundamental band gap of 1.41 eV in the Γ point.

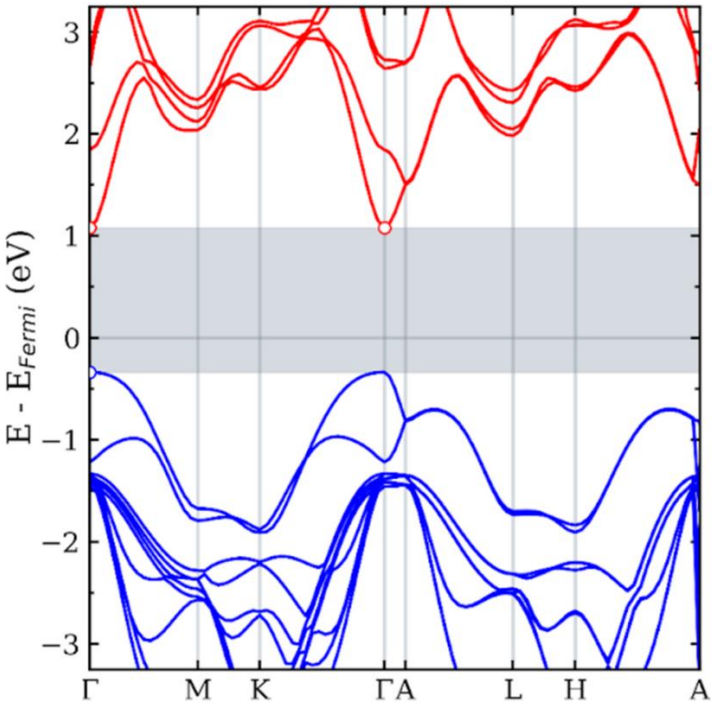

Figure 4.2.12. The electronic band structure of ε-InSe. The band gap value is 1.41 eV.

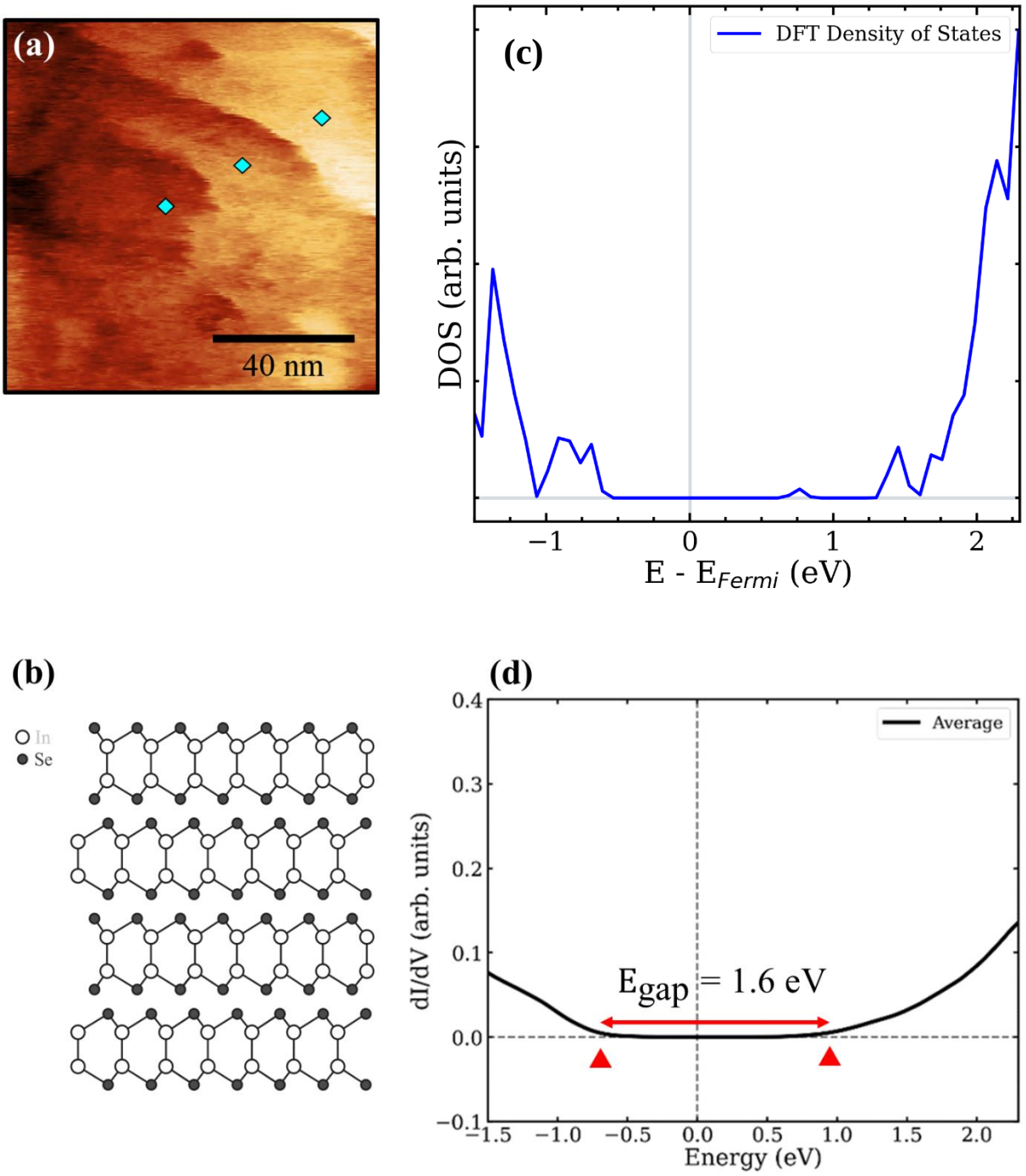

Figure 4.2.13. (a) STM image of the ε-InSe region. **(b)** Stacking sequence of the tetra-layers of ε-InSe. **(c)** Electronic density of states calculations, with a band gap of 1.41 eV. **(d)** Average of the tunneling spectra obtained from the three blue points in the STM image. The band gap estimated by the tunneling spectrum is 1.6 eV.

Using scanning tunneling microscopy and spectroscopy, we were able to obtain an image of a possible region of the ε-InSe. All the tunneling spectra were acquired in the three blue points seen in Figure 4.2.11a. By comparing both the tunneling spectrum and the electronic density of states calculations, a correlation between the profiles of the experimental and theoretical curves is more subtle. Despite not being evident as the previous ones, the value of the band gap corroborates that the tunneling spectrum is indeed from the ε-InSe phase. The band gap starts at approximately -0.7 eV and ends up in 0.9 eV. The valence band in the range of the STS measurement consists of an apparent bump, which we can observe in the computational calculation. However, for positive energies, there are discrepancies between these two curves, as the experimental one exhibits a moderate increase in the electronic states, while the computational curve presents a sharp peak right before a rapid increase.

The use of a room-temperature tunneling microscope leads to several broadening of the tunneling profiles. An estimate of this broadening for room-temperature (T = 300 K), considering a value of $2K_BT$ for both tip and the sample, one obtains a final value of $4K_BT$ = 100 meV. This value should be compared to 10 meV, obtaining if the temperature is 25 K, the typical temperature of a low-temperature STM microscope.

5. CONCLUSIONS AND PERSPECTIVES

In this work, we have successfully synthesized two multiphase indium selenide samples using the Bridgman method. By combining multiple experimental techniques, we managed to characterize a substantial volume of the crystals, composed of several layered polymorphs of InSe and In_2Se_3. The two different approaches in the growth yielded crystals with different proportions of phases and polymorphs.

Scanning electron microscopy measurements demonstrated our success in achieving lamellar phases in both crystals. The X-ray diffraction and electron backscattered diffraction analysis revealed that both syntheses resulted in highly multiphase indium selenide crystals, while also providing an estimate of phase proportions. For the first sample, we characterized the atomic structure of the α-, β-, and δ-In2Se3 phases, along with the γ- and ε-InSe ones. A new polymorph of InSe with a space group of C2/m was also obtained. In the second sample, we identified only one additional phase compared to the first one, namely the β-InSe. Also, we observed a disparity in grain sizes between both samples, with the fast-cooling crystal exhibiting larger grains.

Through the analysis of tunneling spectra, we were able to observe the electronic local density of states of α, β, and δ-In2Se3, as well as the ε-InSe and InSe (C2/m) polymorphs. We have obtained a semiconductor spectrum for these structures, with the estimated band gaps of the α, β, and δ-In2Se3 polymorphs as 1.4 eV, 0.95 eV, and 0.45 eV, respectively. We have also obtained the band gaps of the ε-InSe and InSe (C2/m) polymorphs as 1.6 eV and 2.0 eV, respectively. These values match the literature, as well as the computational calculations presented in this work.

Obtaining tunneling spectra for other phases presented challenges, primarily due to the limited current range of the scanning tunneling microscope pre-amplifier (±20 nA). Most of the phases saturated the tunneling current during I-V acquisition, making it difficult to distinguish curve profiles. As a perspective, these measurements could be conducted utilizing the ultra-high vacuum scanning tunneling microscope available in our Nanoscopia-UHV laboratory, as the tunneling current limit in this microscope is around 330 nA.

REFERENCES

[1] NOVOSELOV, Kostya S. et al. Electric field effect in atomically thin carbon films. **Science**, v. 306, n. 5696, p. 666-669, 2004.

[2] NETO, AH Castro et al. The electronic properties of graphene. **Reviews of Modern Physics**, v. 81, n. 1, p. 109, 2009.

[3] AVOURIS, Phaedon. Graphene: electronic and photonic properties and devices. **Nano Letters**, v. 10, n. 11, p. 4285-4294, 2010.

[4] SARMA, S. Das et al. Electronic transport in two-dimensional graphene. **Reviews of Modern Physics**, v. 83, n. 2, p. 407, 2011.

[5] BALANDIN, Alexander A. et al. Superior thermal conductivity of single-layer graphene. **Nano Letters**, v. 8, n. 3, p. 902-907, 2008.

[6] BALANDIN, Alexander A. Thermal properties of graphene and nanostructured carbon materials. **Nature Materials**, v. 10, n. 8, p. 569-581, 2011.

[7] FALKOVSKY, Leonid A. Optical properties of graphene. In: **Journal of Physics: Conference Series**. IOP Publishing, 2008. P. 012004.

[8] GEIM, Andre Konstantin. Graphene: status and prospects. **Science**, v. 324, n. 5934, p. 1530-1534, 2009.

[9] KARAA, Abdelkader et al. A review on silicene—New candidate for electronics. **Surface Science Reports**, v. 67, p. 1-18, 2012.

[10] ACUN, Adil et al. Germanene: the germanium analogue of graphene. **Journal of physics: Condensed Matter**, v. 27, n. 44, p. 443002, 2015.

[11] CARVALHO, Alexandra et al. Phosphorene: from theory to applications. **Nature Reviews Materials**, v. 1, n. 11, p. 1-16, 2016.

[12] LIU, Lei; FENG, Y. P.; SHEN, Z. X. Structural and electronic properties of h-BN. **Physical Review B**, v. 68, n. 10, p. 104102, 2003.

[13] MANZELI, Sajedeh et al. 2D transition metal dichalcogenides. **Nature Reviews Materials**, v. 2, n. 8, p. 1-15, 2017.

[14] YANG, Zhibin; HAO, Jianhua. Recent progress in 2D layered III–VI semiconductors and their heterostructures for optoelectronic device applications. **Advanced Materials Technologies**, v. 4, n. 8, p. 1900108, 2019.

[15] MAO, Ning et al. Ferroelectric higher-order topological insulator in two dimensions. **Physical Review B**, v. 107, n. 4, p. 045125, 2023.

[16] DING, Wenjun et al. Prediction of intrinsic two-dimensional ferroelectrics in In_2Se_3 and other III2-VI3 van der Waals materials. **Nature Communications**, v. 8, n. 1, p. 14956, 2017.

[17] HAN, Guang et al. Indium selenides: structural characteristics, synthesis and their thermoelectric performances. **Small**, v. 10, n. 14, p. 2747-2765, 2014.

[18] GRIMALDI, I. et al. Structural investigation of InSe layered semiconductors. **Solid State Communications**, v. 311, p. 113855, 2020.

[19] VAN LANDUYT, J.; VAN TENDELOO, G.; AMELINCKX, S. Phase transitions in In_2Se_3 as studied by electron microscopy and electron diffraction. **Phys. Status Solidi (a); (German Democratic Republic),** v. 30, 1975.

[20] POPOVIĆ, S. et al. Revised and new crystal data for indium selenides. **Journal of Applied Crystallography**, v. 12, n. 4, p. 416-420, 1979.

[21] MANOLIKAS, C. New results on the phase transformations of In_2Se_3. **Journal of Solid State Chemistry**, v. 74, n. 2, p. 319-328, 1988.

[22] LI, Wei et al. Large disparity between optical and fundamental band gaps in layered In_2Se_3. **Physical Review B**, v. 98, n. 16, p. 165134, 2018.

[23] KÜPERS, Michael et al. Controlled crystal growth of indium selenide, In_2Se_3, and the crystal structures of α-In_2Se_3. **Inorganic Chemistry**, v. 57, n. 18, p. 11775-11781, 2018.

[24] SEGURA, Alfredo. Layered indium selenide under high pressure: a review. Crystals, v. 8, n. 5, p. 206, 2018.

[25] ZHOU, Yu et al. Out-of-plane piezoelectricity and ferroelectricity in layered α-In_2Se_3 nanoflakes. **Nano Letters**, v. 17, n. 9, p. 5508-5513, 2017.

[26] WAN, Siyuan et al. Nonvolatile ferroelectric memory effect in ultrathin α-In_2Se_3. **Advanced Functional Materials**, v. 29, n. 20, p. 1808606, 2019.

[27] WANG, Lin et al. Exploring ferroelectric switching in α-In_2Se_3 for neuromorphic computing. Advanced Functional Materials, v. 30, n. 45, p. 2004609, 2020.

[28] HE, Qinming et al. Epitaxial Growth of Large Area Two-Dimensional Ferroelectric α-In_2Se_3. **Nano Letters**, v. 23, n. 7, p. 3098-3105, 2023.

[29] XUE, Fei et al. Multidirection piezoelectricity in mono-and multilayered hexagonal α-In_2Se_3. **ACS Nano**, v. 12, n. 5, p. 4976-4983, 2018.

[30] GUO, Feng et al. Piezoelectric biaxial strain effects on the optical and photoluminescence spectra of 2D III–VI compound α-In_2Se_3 nanosheets. **Applied Physics Letters**, v. 116, n. 11, 2020.

[31] UEDA, Keisuke et al. Piezoelectric effect in 2H and 3R phases of α-In_2Se_3. **Japanese Journal of Applied Physics**, 2023.

[32] HAO, Qiaoyan et al. Phase identification and strong second harmonic generation in pure ε-InSe and its alloys. **Nano Letters**, v. 19, n. 4, p. 2634-2640, 2019.

[33] SUN, Maojun et al. ε-InSe single crystals grown by a horizontal gradient freeze method. **CrystEngComm**, v. 22, n. 45, p. 7864-7869, 2020.

[34] DA COSTA, P. Gomes et al. First-principles study of the electronic structure of γ-InSe and β-InSe. **Physical Review B**, v. 48, n. 19, p. 14135, 1993.

[35] LIN, Min et al. Controlled growth of atomically thin In2Se3 flakes by van der Waals epitaxy. **Journal of the American Chemical Society**, v. 135, n. 36, p. 13274-13277, 2013.

[36] TAO, Xin; GU, Yi. Crystalline-crystalline phase transformation in two-dimensional In_2Se_3 thin layers. **Nano Letters**, v. 13, n. 8, p. 3501-3505, 2013.

[37] SEO, Dong Hyun et al. Characteristics of Rhombohedral (3R) Structure of α-In_2Se_3 Nanosheets by Mechanical Exfoliation. **Electronic Materials Letters**, p. 1-7, 2023.

[38] LIU, Lixuan et al. Atomically resolving polymorphs and crystal structures of In_2Se_3. Chemistry of Materials, v. 31, n. 24, p. 10143-10149, 2019.

[39] LI, C. F. et al. Band structure, ferroelectric instability, and spin–orbital coupling effect of bilayer α-In2Se3. **Journal of Applied Physics**, v. 128, n. 23, 2020.

[40] NARITA, Nobuo et al. Band structure of layered semiconductor α-In_2Se_3. **Journal of the Physical Society of Japan**, v. 60, n. 4, p. 1279-1285, 1991.

[41] HO et al. Surface Oxide Effect on Optical Sensing and Photoelectric Conversion of α-In2Se3 Hexagonal Microplates. **ACS Applied Materials & Interfaces**, v. 5, n. 6, p. 2269-2277, 2013.

[42] JACOBS-GEDRIM, Robin B. et al. Extraordinary photoresponse in two-dimensional In2Se3 nanosheets. **ACS Nano**, v. 8, n. 1, p. 514-521, 2014.

[43] LYU, Fengjiao et al. Thickness-dependent band gap of α-In_2Se_3: from electron energy loss spectroscopy to density functional theory calculations. **Nanotechnology**, v. 31, n. 31, p. 315711, 2020.

[44] WANG, Jianming et al. Solution-processable 2D α-In_2Se_3 as an efficient hole transport layer for high-performance and stable polymer solar cells. **Solar RRL**, v. 4, n. 3, p. 1900428, 2020.

[45] ZHANG, Wei et al. α-In_2Se_3 Nanostructure-Based Photodetectors for Tunable and Broadband Response. **ACS Applied Nano Materials**, 2023.

[46] OSAMURA, Kozo; MURAKAMI, Yotaro; TOMIIE, Yujiro. Crystal Structures of α-and β-indium selenide, In_2Se_3. **Journal of the Physical Society of Japan**, v. 21, n. 9, p. 1848-1848, 1966.

[47] ZHANG, Fan et al. Atomic-scale observation of reversible thermally driven phase transformation in 2D In_2Se_3. **ACS Nano**, v. 13, n. 7, p. 8004-8011, 2019.

[48] DEBBICHI, Lamjed; ERIKSSON, Olle; LEBÈGUE, Sébastien. Two-dimensional indium selenides compounds: an ab initio study. **The Journal of Physical Chemistry Letters**, v. 6, n. 15, p. 3098-3103, 2015.

[49] BOLARINWA, Sherifdeen O.; SATTAR, Shahid; ALSHAIKHI, Abdullah A. Superior gas sensing properties of β-In_2Se_3: A first-principles investigation. **Computational Materials Science**, v. 201, p. 110880, 2022.

[50] CLARO, Marcel S. et al. Wafer-scale fabrication of 2D β-In_2Se_3 photodetectors. **Advanced Optical Materials**, v. 9, n. 1, p. 2001034, 2021.

[51] ZHENG, Zhaoqiang et al. Self-assembly high-performance UV–vis–NIR broadband β-In_2Se_3/Si photodetector array for weak signal detection. **ACS Applied Materials & Interfaces**, v. 9, n. 50, p. 43830-43837, 2017.

[52] LUTZ, H. D. et al. Zur polymorphie des In_2Se_3. **Journal of the Less Common Metals**, v. 143, n. 1-2, p. 83-92, 1988.

[53] ČELUSTKA, B.; POPOVIĆ, S. The synthesis of In5Se6 and In2Se from InSe by zone-melting process. **Journal of Physics and Chemistry of Solids**, v. 35, n. 2, p. 287-289, 1974.

[54] GRIMALDI, I. et al. Structural investigation of InSe layered semiconductors. **Solid State Communications**, v. 311, p. 113855, 2020.

[55] KANG, L. et al. Surface photovoltaic effect and electronic structure of β-InSe. **Physical Review Materials**, v. 4, n. 12, p. 124604, 2020.

[56] GUO, Yuzheng; ROBERTSON, John. Band structure, band offsets, substitutional doping, and Schottky barriers of bulk and monolayer InSe. **Physical Review Materials**, v. 1, n. 4, p. 044004, 2017.

[57] GÜRBULAK, Bekir et al. Structural characterizations and optical properties of InSe and InSe: Ag semiconductors grown by Bridgman/Stockbarger technique. **Physica E: Low-dimensional Systems and Nanostructures**, v. 64, p. 106-111, 2014.

[58] SANG, David K. et al. Two dimensional β-InSe with layer-dependent properties: band alignment, work function and optical properties. **Nanomaterials**, v. 9, n. 1, p. 82, 2019.

[59] HU, Haowen et al. Room-temperature out-of-plane and in-plane ferroelectricity of two-dimensional β-InSe nanoflakes. **Applied Physics Letters**, v. 114, n. 25, 2019.

[60] LI, Jialin et al. Highly sensitive photodetector based on two-dimensional ferroelectric semiconducting β-InSe/graphene heterostructure. **Applied Physics Express**, v. 16, n. 2, p. 021002, 2023.

[61] LIKFORMAN, A. et al. Structure cristalline du monosélénure d'indium InSe. **Acta Crystallographica Section B: Structural Crystallography and Crystal Chemistry**, v. 31, n. 5, p. 1252-1254, 1975.

[62] RIGOULT, J.; RIMSKY, A.; KUHN, A. Refinement of the 3R γ-indium monoselenide structure type. **Acta Crystallographica Section B: Structural Crystallography and Crystal Chemistry**, v. 36, n. 4, p. 916-918, 1980.

[63] DA COSTA, P. Gomes et al. First-principles study of the electronic structure of γ-InSe and β-InSe. **Physical Review B**, v. 48, n. 19, p. 14135, 1993.

[64] XU, Huanfeng et al. Temperature-induced band shift in bulk γ-InSe by angle-resolved photoemission spectroscopy. **AIP Advances**, v. 8, n. 5, 2018.

[65] HAMER, Matthew J. et al. Indirect to direct gap crossover in two-dimensional InSe revealed by angle-resolved photoemission spectroscopy. **ACS nano**, v. 13, n. 2, p. 2136-2142, 2019.

[66] BRUDNYI, Valentin N.; SARKISOV, S. Yu; KOSOBUTSKY, Alexey V. Electronic properties of GaSe, InSe, GaS and GaTe layered semiconductors: charge neutrality level and interface barrier heights. **Semiconductor Science and Technology**, v. 30, n. 11, p. 115019, 2015.

[67] SONG, Chaoyu et al. Largely tunable band structures of few-layer InSe by uniaxial strain. **ACS Applied Materials & Interfaces**, v. 10, n. 4, p. 3994-4000, 2018.

[68] SUI, Fengrui et al. Sliding ferroelectricity in van der Waals layered γ-InSe semiconductor. **Nature Communications**, v. 14, n. 1, p. 36, 2023.

[69] DAI, Mingjin et al. Robust piezo-phototronic effect in multilayer γ-InSe for high-performance self-powered flexible photodetectors. **ACS Nano**, v. 13, n. 6, p. 7291-7299, 2019.

[70] YANG, Baoxiang et al. Visible and infrared photodiode based on γ-InSe/Ge van der Waals heterojunction for polarized detection and imaging. **Nanoscale**, v. 15, n. 7, p. 3520-3531, 2023.

[71] BRIDGMAN, Percy W. Certain physical properties of single crystals of tungsten, antimony, bismuth, tellurium, cadmium, zinc, and tin. In: **Papers 32-58**. Harvard University Press, 1964. P. 1851-1932.

[72] ATUCHIN, V. V. et al. Formation of inert Bi2Se3 (0001) cleaved surface. **Crystal Growth & Design**, v. 11, n. 12, p. 5507-5514, 2011.

[73] HRUBAN, A. et al. Reduction of bulk carrier concentration in Bridgman-grown Bi2Se3 topological insulator by crystallization with Se excess and Ca doping. **Journal of Crystal Growth**, v. 407, p. 63-67, 2014.

[74] CHEN, X. et al. Thermal expansion coefficients of Bi2Se3 and Sb2Te3 crystals from 10 K to 270 K. **Applied Physics Letters**, v. 99, n. 26, 2011.

[75] RAJPUT, Indu et al. Crystal growth and x-ray diffraction characterization of Sb2Te3 single crystal. In: **AIP Conference Proceedings**. AIP Publishing, 2019.

[76] AUSTIN, L.; STARKE, H. Ueber die Reflexion der Kathodenstrahlen und eine damit verbundene neue Erscheinung secundärer Emission. **Annalen der Physik**, v. 314, n. 10, p. 271-292, 1902.

[77] INKSON, Beverley J. Scanning electron microscopy (SEM) and transmission electron microscopy (TEM) for materials characterization. In: **Materials characterization using nondestructive evaluation (NDE) methods**. Woodhead publishing, 2016. P. 17-43.

[78] EDS MEASUREMENT of Copper (Cu) and its Artifacts. Disponível em: https://www.globalsino.com/EM/page4479.html. Acesso em: 28 jul. 2023.

[79] NISHIKAWA, SHOJI; KIKUCHI, SEISHI. Diffraction of cathode rays by calcite. **Nature**, v. 122, n. 3080, p. 726-726, 1928.

[80] NISHIKAWA, S.; KIKUCHI, S. Diffraction of cathode rays by mica. **Nature**, v. 121, n. 3061, p. 1019-1020, 1928.

[81] SCHWARTZ, Adam J. et al. (Ed.). **Electron backscatter diffraction in materials science**. New York: Springer, 2009.

[82] THE CHARACTERIZATION Advantage of Electron Backscatter Diffraction (EBSD) Microscopy – RJ Lee Group, Inc. (RJLG). Disponível em: https://www.rjlg.com/materials-insights/the-characterization-advantage-of-electron-backscatter-diffraction-ebsd-microscopy/. Acesso em: 28 jul. 2023.

[83] UL-HAMID, Anwar. **A beginners' guide to scanning electron microscopy**. Cham, Switzerland: Springer International Publishing, 2018.

[84] WATSON, James D.; CRICK, Francis HC. Molecular structure of nucleic acids: a structure for deoxyribose nucleic acid. **Nature**, v. 171, n. 4356, p. 737-738, 1953.

[85] ALS-NIELSEN, Jens; MCMORROW, Des. **Elements of modern X-ray physics**. John Wiley & Sons, 2011.

[86] ROBINSON, Ian K. Crystal truncation rods and surface roughness. **Physical Review B**, v. 33, n. 6, p. 3830, 1986.

[87] BINNIG, Gerd et al. Tunneling through a controllable vacuum gap. **Applied Physics Letters**, v. 40, n. 2, p. 178-180, 1982.

[88] BINNIG, Gerd et al. Surface studies by scanning tunneling microscopy**. Physical Review Letters**, v. 49, n. 1, p. 57, 1982.

[89] LI, Guohong; LUICAN, Adina; ANDREI, Eva Y. Scanning tunneling spectroscopy of graphene on graphite. **Physical Review Letters**, v. 102, n. 17, p. 176804, 2009.

[90] ZHAO, Kun et al. Scanning tunneling microscopy studies of topological insulators. **Journal of Physics: Condensed Matter**, v. 26, n. 39, p. 394003, 2014.

[91] CHEN, Mu et al. Molecular beam epitaxy of bilayer Bi (111) films on topological insulator Bi2Te3: A scanning tunneling microscopy study. **Applied Physics Letters**, v. 101, n. 8, 2012.

[92] CHAGAS, Thais et al. Bi2: Bi2Te3 stacking influence on the surface electronic response of the topological insulator Bi4Te3. **Electronic Structure**, v. 2, n. 1, p. 015002, 2020.

[93] KUBBY, Joel A.; BOLAND, John J. Scanning tunneling microscopy of semiconductor surfaces. **Surface Science Reports**, v. 26, n. 3-6, p. 61-204, 1996.

[94] FEENSTRA, Randall M. A prospective: Quantitative scanning tunneling spectroscopy of semiconductor surfaces. **Surface Science**, v. 603, n. 18, p. 2841-2844, 2009.

[95] HILL, Heather M. et al. Band alignment in MoS2/WS2 transition metal dichalcogenide heterostructures probed by scanning tunneling microscopy and spectroscopy. **Nano Letters**, v. 16, n. 8, p. 4831-4837, 2016.

[96] RIGOSI, Albert F. et al. Electronic band gaps and exciton binding energies in monolayer $Mo_xW_{1-x}S_2$ transition metal dichalcogenide alloys probed by scanning tunneling and optical spectroscopy. **Physical Review B**, v. 94, n. 7, p. 075440, 2016.

[97] HANSMA, Paul K. et al. Scanning tunneling microscopy and atomic force microscopy: application to biology and technology. **Science**, v. 242, n. 4876, p. 209-216, 1988.

[98] GUCKENBERGER, Reinhard et al. Scanning tunneling microscopy of insulators and biological specimens based on lateral conductivity of ultrathin water films. **Science**, v. 266, n. 5190, p. 1538-1540, 1994.

[99] MCINTYRE, David H. **Quantum Mechanics: A Paradigms Approach**. Cambridge University Press, 2022.

[100] EASYSCAN, Nanosurf. **Nanosurf Easyscan 2 STM Operating Instructions**, 3.1.

[101] BARDEEN, John. Tunnelling from a many-particle point of view. **Physical Review Letters**, v. 6, n. 2, p. 57, 1961.

[102] GIAEVER, Ivar; MEGERLE, Karl. Study of superconductors by electron tunneling. **Physical Review**, v. 122, n. 4, p. 1101, 1961.

[103] TERSOFF, Jerry; HAMANN, Donald R. Theory and application for the scanning tunneling microscope. **Physical Review Letters**, v. 50, n. 25, p. 1998, 1983.

[104] LOUNIS, Samir. Theory of scanning tunneling microscopy. **arXiv preprint arXiv:1404.0961**, 2014.

[105] SILVA, Thaís Chagas Peixoto et al. Tunneling spectroscopy of 2D materials: unraveling their density of states and the relationship with local atomic environment. 2020.

[106] CHEN, C. Julian. **Introduction to Scanning Tunneling Microscopy Third Edition**. Oxford University Press, USA, 2021.

[107] CONTRIBUTORS TO WIKIMEDIA PROJECTS. Electronic band structure - Wikipedia. 5 jun. 2004. Disponível em: https://en.wikipedia.org/wiki/Electronic_band_structure. Acesso em: 30 jul. 2023.

[108] UW DEPARTMENTS Web Server. Disponível em: https://depts.washington.edu/nanolab/NUE_UNIQUE/Background/AFM.pdf. Acesso em: 30 jul. 2023.